UNIVERSITÀ
DEGLI STUDI
DI PADOVA

Head Office: Università degli Studi di Padova
Department of Industrial Engineering
Electrical Energy Engineering Curriculum
XXXIV Cycle

Advanced Modeling of Anisotropic Synchronous Machine Drives for Sensorless Control

Ph.D. course coordinator: Prof. Giulio Rosati
Curriculum referent: Prof. Luigi Alberti
Supervisor: Prof. Luigi Alberti

Ph.D. student: Matteo Berto

December 2021

"Do not act as if you were going to live ten thousand years. Death hangs over you. While you live, while it is in your power, be good."
Marcus Aurelius

Acknowledgments

I wish to express my gratitude to my supervisor Prof. Luigi Alberti for his guidance during such an important period of my life. He supported me during positive and negative periods, helping me to achieve great results and understand many things about electrical engineering and not only.

A special thank goes to Prof. Marko Hinkkanen for being so welcoming and qualified during my short but special visit to Finland.

I wish to thank my family for always believing in me. This thanks is also addressed to those who will be watching me from far away and unfortunately we can not celebrate together.

A special thank goes to my better half, Sofia. Since I have known her, she always supported me and helped me to believe in my dreams. Some of those dreams are going to come true.

Finally, I would like to thank also all the people I met during my PhD, my friends, my colleagues. All of them contributed to make my PhD journey so special and unforgettable.

Padova, December 2021 Matteo Berto

Contents

Introduction

Synchronous machines are extensively used for home appliances and industrial applications thanks to their fast dynamic response, good overload capability and high energy density. A precise knowledge of the rotor position is required to control efficiently this kind of motors [1]. In most of the applications resolvers or absolute encoders are installed on the rotor shaft. The employment of position sensors leads to significant drawbacks such as the increased size and cost of the system and a lower reliability of the drive, caused by additional hardware and cabling.

In sensorless drives motor position is estimated and employed in the machine control. Thus, no position sensor is required by the drive and all the drawbacks entailed by the sensor are eliminated. Moreover, the position estimation could be useful for redundancy in case of system failures. Therefore, position estimation techniques are object of great interest in the electric drives field.

Position estimation techniques can be divided into two main categories: methods that are suitable for medium or high speed and techniques suitable for low speed or standstill operations. In the former group the motor position is estimated through a reconstruction of the permanent magnet flux or back electromotive force (back-EMF). In case of synchronous reluctance machines it is possible to reconstruct the extended active flux or back-EMF [2–6]. Stator voltages and currents measurements are needed for these reconstruction methods. Since these signals amplitude is proportional to the rotor speed, position estimation can be successfully performed only for medium and high speed machine operations.

In the low speed range, sensorless schemes exploit the rotor magnetic anisotropy. Thus, position can be estimated only for anisotropic motors, i.e. synchronous reluctance motors (SynRM), permanent magnet assisted synchronous reluctance motors (PMA-SynRM) and interior permanent magnet synchronous motors (IPMSM). The rotor anisotropy is recognized thanks to an high frequency voltage injection in the stator windings. Several injection techniques have been proposed, differing from the signal typology. In particular, high frequency sinusoidal [1, 7–9] or square-wave [10] carriers are often applied. The position information is usually extracted from the current response through a heterodyning demodulation that entails the use of low pass filters in the position estimator, limiting its dynamic.

The aim of the research was proposing a new algorithm to estimate the rotor position from the HF current response, getting rid of the demodulation and its weaknesses. Thus, the ellipse fitting technique has been proposed. Robustness against signal processing delay effects and a reduced number of required filters are the main advantages of this novel approach. The inverse problem related to the ellipse fitting is solved implementing a recursive least squares algorithm. The proposed ellipse fitting technique is not affected by signal processing delay effects,

and it requires the tuning of only one parameter, called forgetting factor, making the studied method suitable for industrial application thanks to its minimal setup effort.

Besides the ellipse fitting technique for rotor position estimation, two other topics have been studied:

- Computation of self-sensing capabilities of synchronous machines.
- Online incremental inductances identification for SynRM.

Signal-injection sensorless control methods rely on the current response of a synchronous motor to high frequency voltage injection. Since the considered motors can differ one from the other, it follows that the performance achievable in sensorless control can change significantly depending on the considered machine. Moreover, even the same motor changes its high-frequency response depending on the load. Thus, a systematic and comprehensive method to compute and predict the self-sensing capabilities (saliency, estimation error, convergence region) of a synchronous motor starting from its flux linkages maps is proposed and validated.

SynRM have several advantages: they are cheap, they have high efficiency, and they do not have permanent magnets. One the main disadvantages is that they are characterized by highly non-linear inductances (which make the control not trivial). Thus, an online inductance identification method (based on rotating high frequency voltage injection) for SynRM has been proposed and validated.

Outline

This work is divided into six chapters.

Chapter 1 presents three conventional signal injection methods for low speed sensorless control (pulsating, square-wave and rotating injection) and an innovative approach based on a real time ellipse fitting. The similarities and peculiarities of the presented methods are highlighted through the control schemes and the analytical equations.

Chapter 2 describes a computational approach to compute the self-sensing capabilities of a synchronous motor in order to predict its performance during a sensorless control. The comprehensive model includes flux linkages, apparent and incremental inductances, and the MTPA.

Chapter 3 deals with the experimental procedure to measure the convergence region of a synchronous motor installed on a real test bench. During the first test, the sensored trajectory t_1 is measured. In the second test the sensorless trajectory t_2 is measured.

Chapter 4 presents the innovative ellipse fitting approach to estimate the rotor position of an anisotropic synchronous motor from the high frequency currents due to a rotating injection in $\alpha\beta$. Simulation and experimental results validate the proposed method.

Chapter 5 focuses again on the ellipse fitting approach, but this time a more efficient algorithm (based on recursive QR factorization) is adopted. Experimental results including a comparison with the convention demodulation approach are carried out in order to validate the effectiveness of the presented method.

Chapter 6 proposes an online algorithm to estimate the incremental inductances of a SynRM operating in sensored opeation. The presented method is tested both during current and speed transients in order the examine its estimation accuracy.

Original contribution

The first main contribution of the research carried out during these three years was the ellipse fitting technique for the rotating injection in $\alpha\beta$. The proposed method appears to be less sensitive, if compared with the conventional demodulation scheme, to the signal processing delay effects.

A second contribution was the computation of the self-sensing capabilities of a synchronous motor. With a simple and open source Python code[1] it is possible to obtain a clear prediction of the sensorless performances of a motor (as well as the computation of the apparent/incremental inductances and the MTPA).

Another key contribution was recognizing that the rotating high frequency voltage injection scheme can be used for two purposes:

- Rotor position estimation if the injection is in the stationary ($\alpha\beta$) or estimated ($d^x q^x$) reference frame.
- Online incremental inductance estimation if the injection is in the measured rotor frame (dq); a position sensor is required.

[1] https://gitlab.com/LuigiAlberti/dolomites-python (free code)

Glossary

PMSM	Permanent magnet synchronous motor
SPMSM	Surface permanent magnet synchronous motor
IPMSM	Interior permanent magnet synchronous motor
SynRM	Synchronous reluctance motor
PMA-SynRM	Permanent magnet assisted synchronous reluctance motor
HPF	High-pass filter
LPF	Low-pass filter
hf	High frequency
$\alpha\beta$	Stator reference frame
dq	Rotor reference frame
$d^x q^x$	Estimated rotor reference frame
θ_{me}	Rotor electrical position (rad)
ω_{me}	Rotor electrical speed (rad/s)
$\widetilde{\theta}_{me}$	Estimated rotor electrical position (rad)
$\widetilde{\omega}_{me}$	Estimated rotor electrical speed (rad/s)
u_d, u_q	Stator voltages (V)
i_d, i_q	Stator currents (A)
λ_d, λ_q	Stator flux linkages (Vs)
R	Stator resistance (Ω)
L_d, L_q	Apparent inductances (H)
$l_{dd}, l_{dq}, l_{qd}, l_{qq}$	Incremental inductances (H)
l_Σ	Mean incremental inductance (H)
l_Δ	Semi-difference incremental inductance (H)
$\gamma_{dd}, \gamma_{dq}, \gamma_{qd}, \gamma_{qq}$	Inverse incremental inductances (1/H)
m	Torque (Nm)
ξ	Saliency ratio
ε	Estimation error in open loop (rad)
U_h	Amplitude of the voltage injection (V)
f_h	Frequency of the voltage injection (Hz)
I	Current amplitude (A)
α_{ie}	Current angle (rad)
I_{hq}	Input of the position observer (A)
MTPA	Maximum torque per ampere
REF	Reference for the current control loop
t_1	Sensored (fictitious) current trajectory
t_2	Sensorless current trajectory

Chapter 1

Signal-Injection Sensorless Control

Abstract - Additional signal injection or unconventional pulse-width modulation (PWM) patterns are required in order to estimate the rotor position in the zero-low speed region. This chapter reports an analysis of three different injection schemes for low speed sensorless control (sinusoidal and square-wave pulsating injection in $d^x q^x$, sinusoidal rotating injection in $\alpha\beta$). Also the innovative ellipse fitting method is introduced for the position estimation in the case of rotating injection.

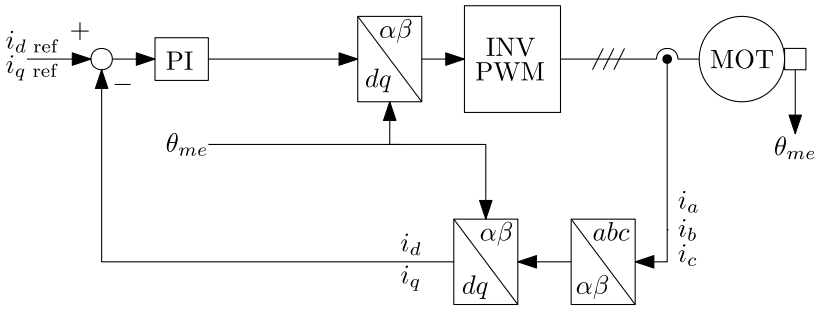

Figure 1.1: Control scheme for synchronous machines drives: conventional PI current control loop.

1.1 Introduction

Conventional control methods of permanent magnet synchronous motors (PMSM) rely on the measure of the rotor position. This type of solution, hereafter called "sensored", requires the use either of an incremental encoder or an absolute resolver (Figure 1.1). The position sensor increases the cost and the size of the electric drive and, moreover, it may be subject to failure. For these reasons it is worth investing the possibility to control a PMSM without the use of a position sensor. These kind of techniques are known as "sensorless". The focus of this work is on the sensorless control methods for standstill and low speed operation, i.e. any operation in which the motor speed is not greater than 10% of the rated speed. Although many high frequency (hf) injection techniques exist (pulsating, square-wave, triangular, pseudo-random, PWM excitation), this work focuses on the rotating voltage injection in the stationary reference frame α-β. Pulsating and square-wave injection in the estimated reference frame $d^x q^x$ are briefly considered in 1.3 and 1.4 just to show that the signal I_{hq} (responsible for the convergence region of the sensorless drive) depends more on the considered machine than on the adopted injection method.

Hf injection range is between 500 Hz and 2000 Hz, reaching half of the switching frequency in the case of square-wave injection. It is worth highlighting that the considered methods consist in extracting the position information contained in the current response due to the hf voltage injection. An anisotropic PMSM, i.e. a PMSM characterized by rotor magnetic saliency, is required for this kind of techniques. Thus, synchronous reluctance motor (SynRM), permanent magnet assisted synchronous reluctance motor (PMA-SynRM) and interior permanent magnet synchronous motor (IPMSM) are suitable for low speed sensorless control. On the contrary, the surface permanent magnet synchronous Motor (SPMSM) has no rotor saliency so the position can not be estimated through hf injection methods. A modified version of SPMSM, the ringed-pole, in which a copper turn has been wound around each rotor pole, is preferable for this kind of applications [11, 12].

1.2 High-frequency model

Signal-injection methods rely on hf voltage injection at low speed. The stator voltage model of a PMSM is:

$$\begin{aligned} u_d(t) &= R\, i_d(t) + l_{dd}\, \frac{di_d(t)}{dt} + l_{dq}\, \frac{di_q(t)}{dt} - \omega_{me}\, \lambda_q \\ u_q(t) &= R\, i_q(t) + l_{dq}\, \frac{di_d(t)}{dt} + l_{qq}\, \frac{di_q(t)}{dt} + \omega_{me}\, \lambda_d \end{aligned} \tag{1.1}$$

where R is the stator resistance, ω_{me} the rotor electrical speed and l_{dd}, l_{dq}, l_{qq} the incremental inductances (2.4). Voltages, currents and incremental inductances are expressed in the rotating reference frame dq.

The permanent magnet does not provide high frequency flux contribution so it can be neglected, as well as the stator resistance. Thus, the hf model of a PMSM is given by incremental inductances only. The hf voltage balance, where $u_{hd}(t)$ and $u_{hq}(t)$ are the injected voltages and $i_{hd}(t)$ and $i_{hq}(t)$ represent the currents response, can be written as:

$$\begin{bmatrix} u_{hd}(t) \\ u_{hq}(t) \end{bmatrix} = \begin{bmatrix} l_{dd} & l_{dq} \\ l_{dq} & l_q \end{bmatrix} \frac{d}{dt} \begin{bmatrix} i_{hd}(t) \\ i_{hq}(t) \end{bmatrix} \tag{1.2}$$

From l_{dd} and l_{qq} it is possible to define:

$$l_\Sigma = \frac{l_{qq} + l_{dd}}{2} \qquad l_\Delta = \frac{l_{qq} - l_{dd}}{2} \tag{1.3}$$

which are the mean incremental inductance and the semi-difference incremental inductance (2.7). It is even possible to obtain the hf voltage balance in the stator reference frame by applying the Park transformation to (1.2):

$$\begin{bmatrix} u_{h\alpha}(t) \\ u_{h\beta}(t) \end{bmatrix} = \begin{bmatrix} l_\alpha & l_{\alpha\beta} \\ l_{\alpha\beta} & l_\beta \end{bmatrix} \frac{d}{dt} \begin{bmatrix} i_{h\alpha}(t) \\ i_{h\beta}(t) \end{bmatrix} \tag{1.4}$$

where:

$$\begin{aligned} l_\alpha &= l_\Sigma - l_\Delta \cos(2\theta_{me}) - l_{dq} \sin(2\theta_{me}) \\ l_\beta &= l_\Sigma + l_\Delta \cos(2\theta_{me}) + l_{dq} \sin(2\theta_{me}) \\ l_{\alpha\beta} &= -l_\Delta \sin(2\theta_{me}) + l_{dq} \cos(2\theta_{me}) \end{aligned} \tag{1.5}$$

It is worth noting that the differential inductances l_α, l_β and $l_{\alpha\beta}$ depend on the rotor electrical position θ_{me}.

In a conventional (sensored) control scheme for PMSM, the rotor position θ_{me} is measured, and the control operates in the actual dq reference frame. In signal-injection (sensorless) schemes the rotor position $\widetilde{\theta}_{me}$ is estimated, and the the control operates in the estimated reference frame $d^x q^x$. Since the estimation methods are afflicted by an estimation error (due to both observer dynamics and cross-saturation effects), the estimated rotor reference frame $d^x q^x$ is usually different from the actual dq (Figure 1.2). The angle between dq and $d^x q^x$ is expressed by $\Delta\theta$. As will be explained in Chapter 2, the steady-state open-loop error due to the cross-saturation effects is $\varepsilon = \text{atan2}(-l_{dq}, l_\Delta)$ or $\varepsilon = \text{atan2}(l_{dq}, -l_\Delta)$ (depending on the adopted motor convention).

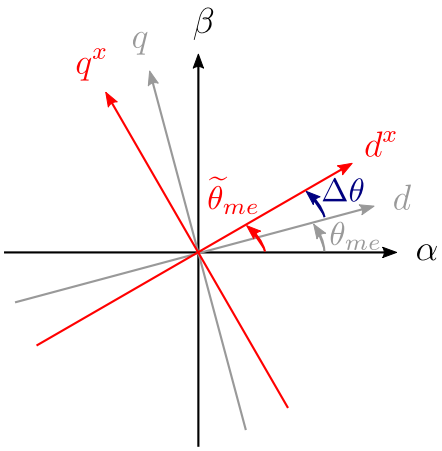

Figure 1.2: Actual and estimated rotor reference frame.

1.3 Sinusoidal injection in $d^x q^x$ (pulsating)

Among the signal-injection schemes present in the literature, one of the simplest is characterized by sinusoidal pulsating injection in $d^x q^x$. The control scheme, shown in Figure 1.3, is described in [8, 13, 14]. A pulsating hf injection is superimposed to the $d^x q^x$ voltage references:

$$u^x_{hd} = U_h \cos(\omega_h t) \tag{1.6}$$
$$u^x_{hq} = 0 \tag{1.7}$$

The sinusoidal pulsating injection in d^x leads to the high frequency currents:

$$i^x_{hd} = \frac{U_h}{\omega_h \left(l_{dd}\, l_{qq} - l^2_{dq}\right)} \left[l_\Sigma + l_\Delta \cos(2\Delta\theta) - l_{dq} \sin(2\Delta\theta)\right] \sin(\omega_h t) \tag{1.8}$$
$$i^x_{hq} = -\frac{U_h}{\omega_h \left(l_{dd}\, l_{qq} - l^2_{dq}\right)} \left[l_\Delta \sin(2\Delta\theta) + l_{dq} \cos(2\Delta\theta)\right] \sin(\omega_h t) \tag{1.9}$$

or, equivalently:

$$i^x_{hd} = \frac{U_h}{\omega_h \left(l_{dd}\, l_{qq} - l^2_{dq}\right)} \left[l_\Sigma + \sqrt{l^2_\Delta + l^2_{dq}} \cos(2\Delta\theta - 2\varepsilon)\right] \sin(\omega_h t) \tag{1.10}$$
$$i^x_{hq} = -\frac{U_h}{\omega_h \left(l_{dd}\, l_{qq} - l^2_{dq}\right)} \left[\sqrt{l^2_\Delta + l^2_{dq}} \sin(2\Delta\theta - 2\varepsilon)\right] \sin(\omega_h t) \tag{1.11}$$

The hf currents i^x_{hd}, i^x_{hq} are obtained measuring the $d^x q^x$ currents and applying a high-pass filter (HPF). The rotor position information is extracted by a demodulation-observer scheme applied to the current i^x_{hq}, as shown in Figure 1.4. The current i^x_{hq} is multiplied for $\sin(\omega_h t)$ and the result is filtered with a low-pass filter (LPF). The result of the demodulation is the signal:

$$I_{hq} = -\frac{U_h}{2\,\omega_h \left(l_{dd}\, l_{qq} - l^2_{dq}\right)} \left[-l_\Delta \sin(2\Delta\theta) - l_{dq} \cos(2\Delta\theta)\right] \tag{1.12}$$

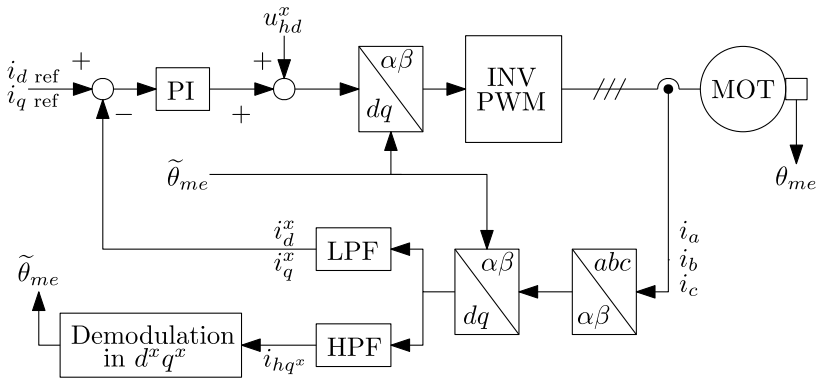

Figure 1.3: Control scheme for anisotropic synchronous machines drives: pulsating injection in $d^x q^x$ and demodulation.

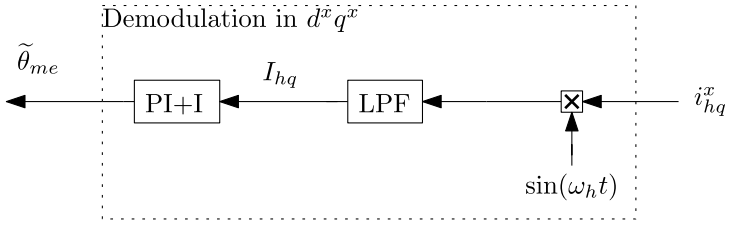

Figure 1.4: Demodulation scheme in $d^x q^x$.

or, equivalently:

$$I_{hq} = -\frac{U_h}{2\,\omega_h\,(l_{dd}\,l_{qq} - l_{dq}^2)}\sqrt{l_\Delta^2 + l_{dq}^2}\,\sin(2\Delta\theta - 2\varepsilon) \tag{1.13}$$

The signal I_{hq} is related to the convergence region of the sensorless drive since it is the signal that the position observer (a PI+I) tries to nullify in order to find the stable convergence points [15]. In fact, I_{hq} is the input of the position observer. The output of the position observer, i.e. the estimated position $\widetilde{\theta}_{me}$, is used to feed the current control loop Park transformations.

1.4 Square-wave injection in $d^x q^x$ (pulsating)

The square-wave injection has been proposed as an alternative of the sinusoidal injection for the sensorless control of anisotropic synchronous motors [16]. A square-wave pulsating injection in d^x:

$$u^x_{hd} = U_h\,\mathrm{clk}[n] \tag{1.14}$$

$$u^x_{hq} = 0 \tag{1.15}$$

leads to square-wave currents:

$$\Delta i_{hd}^{x} = \frac{U_h\, T_s}{l_{dd}\, l_{qq} - l_{dq}^2} \left[l_\Sigma + \sqrt{l_\Delta^2 + l_{dq}^2} \cos(2\Delta\theta - 2\varepsilon) \right] \text{clk}[n-2] \tag{1.16}$$

$$\Delta i_{hq}^{x} = -\frac{U_h\, T_s}{l_{dd}\, l_{qq} - l_{dq}^2} \left[\sqrt{l_\Delta^2 + l_{dq}^2} \sin(2\Delta\theta - 2\varepsilon) \right] \text{clk}[n-2] \tag{1.17}$$

where Ts is the control period. The current Δi_{hq}^{x} can be written as:

$$\Delta i_{hq}^{x} = I_{hq}\, \text{clk}[n-2] \tag{1.18}$$

where:

$$I_{hq} = -\frac{U_h\, T_s}{2(l_{dd}\, l_{qq} - l_{dq}^2)} \sqrt{l_\Delta^2 + l_{dq}^2} \sin(2\Delta\theta - 2\varepsilon) \tag{1.19}$$

I_{hq} is the input signal for the position tracking. Comparing (1.19) and (1.13) it is possible to notice that, theoretically, two different injection schemes lead to almost the same signal I_{hq} (signal related to the convergence region, a concept that will be deepened in chapter). Thus, it is possible to state that the convergence region mainly depends on the considered motor (characterized by the inductances l_{dd}, l_{dq}, l_{qq}, l_Δ), and not so much on the injection/demodulation method. This will be confirmed also in the next section dealing with rotating injection in $\alpha\beta$.

1.5 Sinusoidal injection in $\alpha\beta$ (rotating)

Sensorless control schemes for rotor position estimation at standstill or low speed can operate with a pulsating injection on d^x but also with of a rotating injection in α-β [9]. The scheme is shown in Figure 1.5. A sinusoidal rotating injection in α-β:

$$u_{h\alpha} = U_h \cos(\omega_h t) \tag{1.20a}$$

$$u_{h\beta} = U_h \sin(\omega_h t) \tag{1.20b}$$

leads to high frequency currents:

$$i_{h\alpha} = \frac{U_h}{\omega_h\, (l_{dd}\, l_{qq} - l_{dq}^2)} \left[l_\Sigma\, \sin(\omega_h t) + \sqrt{l_\Delta^2 + l_{dq}^2}\, \sin(\omega_h t - 2\widetilde{\theta}_{me}) \right] \tag{1.21a}$$

$$i_{h\beta} = \frac{U_h}{\omega_h\, (l_{dd}\, l_{qq} - l_{dq}^2)} \left[-l_\Sigma\, \cos(\omega_h t) + \sqrt{l_\Delta^2 + l_{dq}^2}\, \cos(\omega_h t - 2\widetilde{\theta}_{me}) \right] \tag{1.21b}$$

The hf currents $i_{h\alpha}$ and $i_{h\beta}$ contain information on the rotor position $\widetilde{\theta}_{me}$. Heterodyning demodulation, shown in Figure 1.6, is the conventional approach to retrieve the rotor position estimation [17,18]: $i_{h\alpha}$ is multiplied for $-\cos(\omega_h t - 2\widetilde{\theta}_{me})$, $i_{h\beta}$ for $\sin(\omega_h t - 2\widetilde{\theta}_{me})$. The results of the products are summed and filtered with a LPF. The result of the demodulation (input of the position observer) is the signal:

$$I_{hq} = -\frac{U_h}{\omega_h\, (l_{dd}\, l_{qq} - l_{dq}^2)} \sqrt{l_\Delta^2 + l_{dq}^2} \sin(2\Delta\theta - 2\varepsilon) \tag{1.22}$$

The signal I_{hq} in the case of rotating injection in $\alpha\beta$ (1.22) is equal to the one in the case of pulsating injection, (1.13) and (1.19), apart from a factor 2 in the denominator. Thus, the convergence region will be almost the same in all the three considered cases.

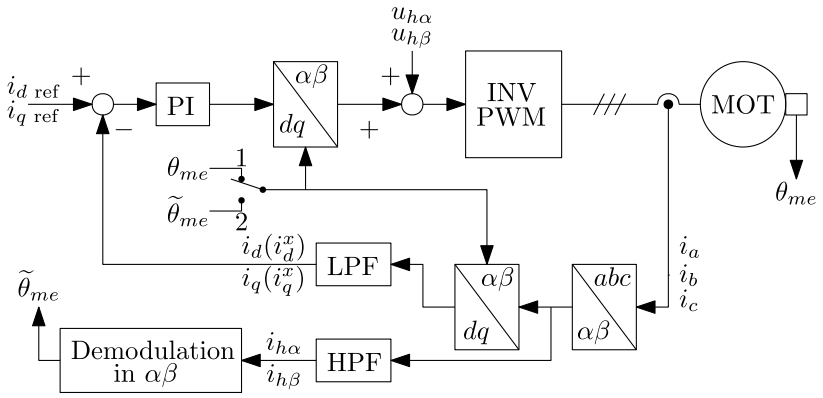

Figure 1.5: Control scheme for anisotropic synchronous machines drives: rotating injection in $\alpha\beta$ and demodulation. When the switch is on position 1, the control operates on the measured dq reference frame (sensored operation). When the switch is on position 2, the control operates on the estimated $\mathrm{d}^x\mathrm{q}^x$ reference frame (sensorless operation).

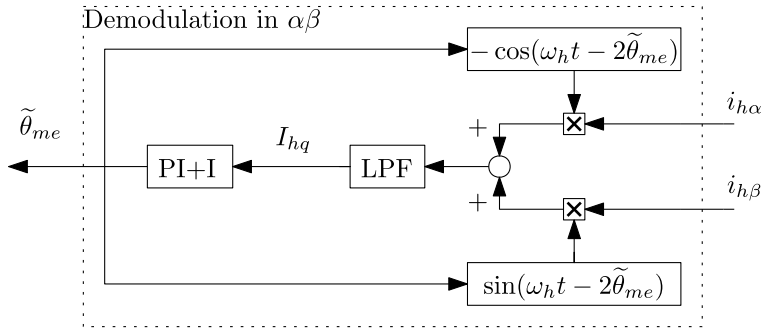

Figure 1.6: Demodulation scheme in $\alpha\beta$.

1.6 Ellipse fitting

"Ellipse fitting" [19, 20] represents an alternative to the demodulation scheme in α-β. The current samples are filtered with a HPF, as in the demodulation scheme, and processed with an ellipse fitting algorithm. In fact, since the injection is a rotating vector and the considered motors (SynRM, PMA-SynRM, IPMSM) have salient rotor, it follows that the hf currents vector traces an ellipse in the α-β plane. The hf vector requires one period of the injected voltage to complete the ellipse drawing. This hf ellipse is ideally centered in the origin of the α-β plane thanks to the effect of the HPF. Anyway, during transients, some deviations can appear. A key aspect of the hf current response in α-β is that the hf ellipse rotates accordingly with the rotor position. In particular, the ellipse major semi-axis is oriented with the rotor axis characterized by lower inductance (axis d for IPMSM and PMA-SynRM, axis q for SynRM). The main idea behind the ellipse fitting method is recognizing in real-time the ellipse major semi-axis tilt in order to estimate the rotor position. In mathematical terms, an inverse problem has to be solved. The

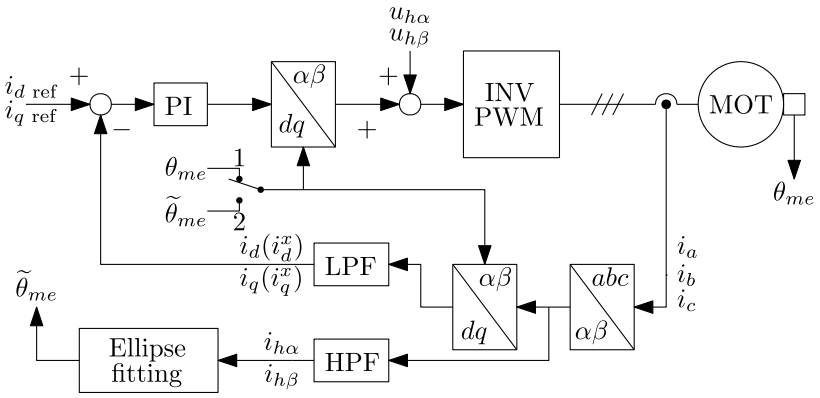

Figure 1.7: Control scheme for anisotropic synchronous machines drives: rotating injection in $\alpha\beta$ and ellipse fitting. When the switch is on position 1, the control operates on the measured dq reference frame (sensored operation). When the switch is on position 2, the control operates on the estimated $\mathrm{d}^x\mathrm{q}^x$ reference frame (sensorless operation).

linear system is composed by the hf current samples as data points, 3 unknown parameters (ellipse coefficients a, b, c) and known terms fixed with the amplitude and frequency of the voltage injection (ellipse coefficient f). In [19,20] the problem is solved through recursive least square estimator (RLSE). In particular, in [19], the solution is computed recursively taking into consideration the incremental variation of a, b, c with respect to the previous time step. In [20] a computationally efficient algorithm is proposed: the inverse problem is recursively solved using an updating QR factorization.

The hf currents induced by the rotating injection $u_{h\alpha}, u_{h\beta}$ can be written in the following form:

$$\begin{aligned}\mathbf{i}_{\alpha\beta} = \begin{bmatrix} i_{h\alpha} \\ i_{h\beta} \end{bmatrix} = \frac{U_h}{\omega_h (l_{dd}\ l_{qq} - l_{dq}^2)} \Bigg(l_\Sigma \begin{bmatrix} \sin\omega_h t \\ -\cos\omega_h t \end{bmatrix} + l_\Delta \begin{bmatrix} \sin(\omega_h t - 2\theta_{me}) \\ \cos(\omega_h t - 2\theta_{me}) \end{bmatrix} + \\ + l_{dq} \begin{bmatrix} \cos(\omega_h t - 2\theta_{me}) \\ -\sin(\omega_h t - 2\theta_{me}) \end{bmatrix} \Bigg) = \mathbf{i}_\Sigma + \mathbf{i}_\Delta + \mathbf{i}_{dq}\end{aligned} \tag{1.23}$$

The three equation terms represent three circular trajectories in the α-β reference frame. Figure 1.8 shows the trajectories of the three current vectors rotating at high frequency. The sum of the three circles leads to an ellipse that rotates exactly at the electrical speed $\widetilde{\omega}_{me}$. At standstill the hf ellipse is stationary. The major semi-axis tilt corresponds to the estimated rotor position $\widetilde{\theta}_{me}$. It is worth noting that the adopted HPF eliminates the fundamental component due to the operating working point. This ensures that the hf ellipse is centered in the origin of the α-β reference frame.

The hf ellipse brings information about rotor mechanical-electrical position and speed, as shown in Figure 1.9. Major axis tilt $\widetilde{\theta}_{me}$ and rotation speed $\widetilde{\omega}_{me}$ are indirect measurements of the actual rotor position θ_{me} and speed ω_{me}.

In the following analysis, the implicit equation of an ellipse centered in the origin is adopted:

$$a\,x^2 + b\,xy + c\,y^2 + f = 0 \tag{1.24}$$

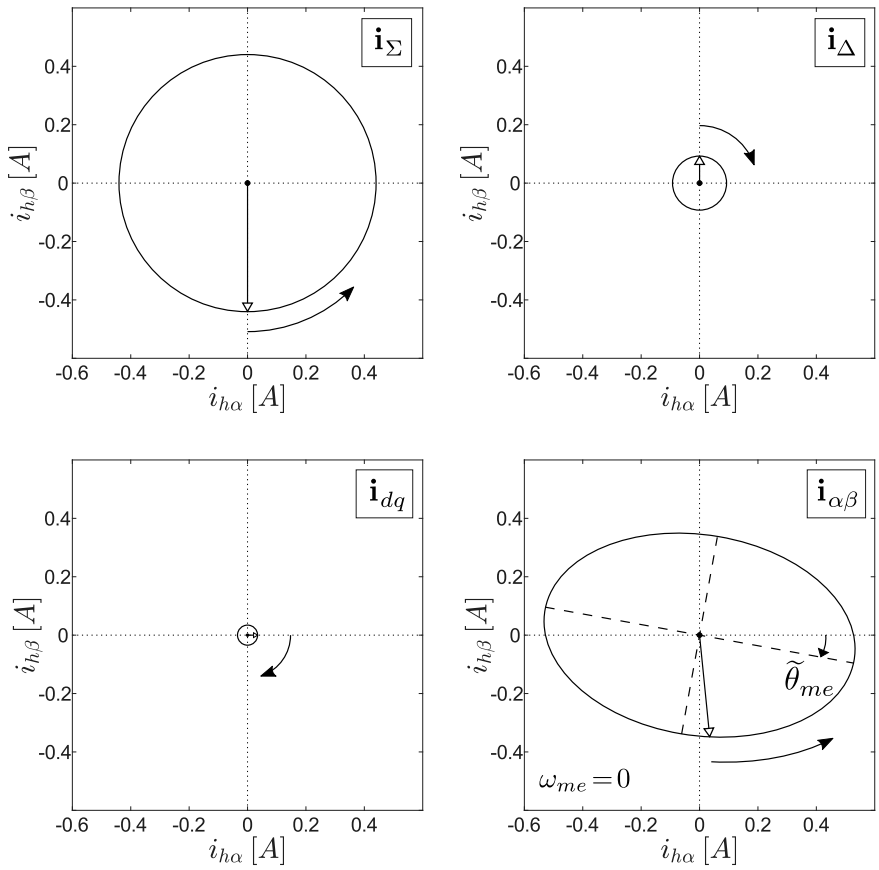

Figure 1.8: hf rotating vectors at standstill with $\theta_{me} = 0$. Resulting ellipse is not horizontal because of $l_{dq} \neq 0$.

where $x = i_{h\alpha}$ and $y = i_{h\beta}$. The mathematical relationships between ellipse equation coefficients and motor inductive parameters are summarized in the following:

$$\begin{aligned} a &= l_\Sigma^2 + l_\Delta^2 + l_{dq}^2 - 2\, l_\Sigma \sqrt{l_\Delta^2 + l_{dq}^2}\cos(2\widetilde{\theta}_{me}) \\ b &= -4\, l_\Sigma \sqrt{l_\Delta^2 + l_{dq}^2}\sin(2\widetilde{\theta}_{me}) \\ c &= l_\Sigma^2 + l_\Delta^2 + l_{dq}^2 + 2\, l_\Sigma \sqrt{l_\Delta^2 + l_{dq}^2}\cos(2\widetilde{\theta}_{me}) \\ f &= -\frac{U_h^2}{\omega_h^2} \end{aligned} \tag{1.25}$$

It is important to highlight that the ellipse coefficients a, b and c vary with the rotor position, as shown in Figure 1.10, allowing (1.24) to describe a rotating ellipse. Differently the coefficient f depends only on the injected signal and not on the rotor position.

The major semi-axis tilt $\widetilde{\theta}_{me}$ can be written in terms of the ellipse coefficients

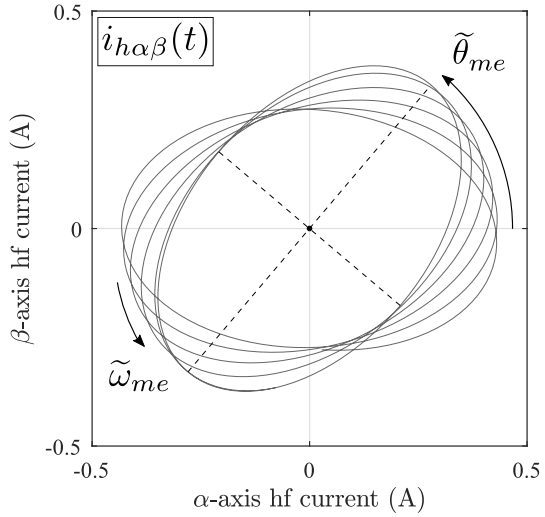

Figure 1.9: hf currents response to rotating injection.

(in the case of PMA-SynRM) as:

$$\widetilde{\theta}_{me} = \frac{1}{2}\,\mathrm{atan2}(-b, c-a) \tag{1.26}$$

Cosine and sine of the estimated position $\widetilde{\theta}_{me}$ can be computed as:

$$\cos(2\widetilde{\theta}_{me}) = \frac{c-a}{\sqrt{b^2+(c-a)^2}} \tag{1.27}$$

$$\sin(2\widetilde{\theta}_{me}) = \frac{-b}{\sqrt{b^2+(c-a)^2}} \tag{1.28}$$

$$\cos(\widetilde{\theta}_{me}) = \pm\sqrt{\frac{\cos(2\widetilde{\theta}_{me})+1}{2}} \tag{1.29}$$

$$\sin(\widetilde{\theta}_{me}) = \pm\sqrt{1-\cos^2(\widetilde{\theta}_{me})} \tag{1.30}$$

Applying the formula for the derivative of the inverse tangent to (1.26), the estimated rotor angular speed results:

$$\widetilde{\omega}_{me} = \frac{1}{2}\,\frac{(c-a)^2}{b^2+(c-a)^2}\,\frac{d}{dt}\left(\frac{-b}{c-a}\right). \tag{1.31}$$

The previous equations can be used to estimate the rotor position and speed from the the hf currents $i_{h\alpha}, i_{h\beta}$ processed with the online ellipse fitting. Together with the rotor position and speed, the real-time ellipse fitting allows to compute also the rotor saliency. The ellipse axis detection is feasibile when the rotor saliency can be recognized, i.e. when the ratio between the major s_M and minor s_m ellipse

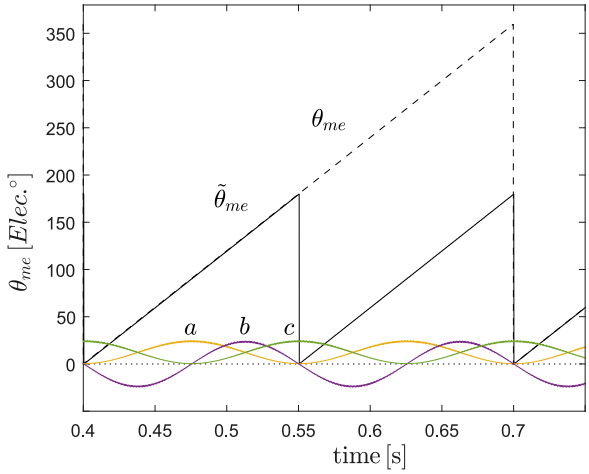

Figure 1.10: Rotor position, estimated position and estimated coefficients a, b, c during a steady state test at 100 rpm.

semi-axes lenghts is greater than one. Semi-axes lenghts can be extrapolated from the ellipse equation coefficients as:

$$s_M = \sqrt{\frac{-2f}{4ac - b^2}\left(a + c + \sqrt{b^2 + (a-c)^2}\right)} \tag{1.32}$$

$$s_m = \sqrt{\frac{-2f}{4ac - b^2}\left(a + c - \sqrt{b^2 + (a-c)^2}\right)} \tag{1.33}$$

It follows that the hf saliency ratio can be monitored online computing:

$$\xi = \frac{s_M}{s_m} = \frac{a + c + \sqrt{b^2 + (a-c)^2}}{a + c - \sqrt{b^2 + (a-c)^2}} \tag{1.34}$$

It is also possible to obtain individually the semi-axes lengths as functions of the differential inductances l_Σ, l_Δ, l_{dq}:

$$s_M = \frac{U_h}{\omega_h} \frac{l_\Sigma + \sqrt{l_\Delta^2 + l_{dq}^2}}{l_\Sigma^2 - l_\Delta^2 - l_{dq}^2} \tag{1.35}$$

$$s_m = \frac{U_h}{\omega_h} \frac{l_\Sigma - \sqrt{l_\Delta^2 + l_{dq}^2}}{l_\Sigma^2 - l_\Delta^2 - l_{dq}^2} \tag{1.36}$$

Moreover, the ellipse fitting approach allows to estimate online the following incremental inductances:

$$l_{\Sigma} = \frac{1}{2}\sqrt{a + c + \sqrt{4ac - b^2}} \tag{1.37}$$

$$\sqrt{l_{\Delta}^2 + l_{dq}^2} = \frac{1}{2}\sqrt{\frac{b^2 + (a-c)^2}{a + c + \sqrt{4ac - b^2}}} \tag{1.38}$$

$$l_{dd}\, l_{qq} - l_{dq}^2 = l_{\Sigma}^2 - l_{\Delta}^2 - l_{dq}^2 = \frac{1}{2}\sqrt{4ac - b^2} \tag{1.39}$$

1.7 Conclusions

In this chapter, three different injection schemes have been briefly considered. Analytical equations show that the considered injection and demodulation schemes share almost the same signal I_{hq} which is related to convergence region of the sensorless drive. As will be seen in detail in the next chapter, sensorless performance is inherently related with the considered motor and its operating point. Also the ellipse fitting scheme has been introduced. This method is innovative since it allows to the extract the rotor position information avoiding the conventional demodulation approach. Experimental results of the ellipse fitting procedure will be shown in the other chapters of the thesis.

Chapter 2

Synchronous Motor Model

Abstract - Performance achievable in sensorless control of electrical drives strictly depends on the adopted synchronous machine. The combination of cross-saturation and saliency, both dependent by the current load and the rotor position, makes always the position estimation afflicted by an estimation error. When the machine is highly saturated, the sensorless control can even diverge resulting in a useless drive. Thus, it is of primary importance to know in advance the convergence region of the sensorless drive, i.e. the operating points where the motor can be successfully controlled without a position sensor.

This chapter presents a computational approach[1] to calculate the inductances, the MTPA and the self-sensing capabilities of a synchronous motor starting from its flux linkages maps. The proposed PMSM model is valid and useful for both sensored and sensorless control [21].

[1] https://gitlab.com/LuigiAlberti/dolomites-python (free code)

2.1 Introduction

The motor itself serves as a sensor in a sensorless drive. The motor self-sensing capability allows to estimate the rotor position measuring and processing the stator currents. Signal injection sensorless control is known to be affected by the variation of the motor differential inductances with the operating point. The variation of the differential inductances makes the same motor change its response to the signal injection depending on the load current. The saliency ratio and the estimation error introduced by the cross-saturation change significantly on the same motor because of the intinsic non-linearities [22,23]. Moreover, depending on the differential inductances shape, some motors can be more suitable than others to be controlled without a position sensor. In particular it has been shown that stator and rotor geometry play a fundamental role on how the motor responds to the signal injection [24–26].

Research on signal injection sensorless control has recently progressed with the introduction of the "convergence region" concept [15, 16]. Previous works focused mainly on saliency ratio and estimation error [27–29]. A motor characterized on average by high saliency ratio and low estimation error is suitable for a sensorless drive, and viceversa. Since both saliency ratio and estimation error depend on the current load, there exist operating points where the motor can be effectively controlled without a position sensor and operating points where the sensorless operation is even unfeasible. Researchers reported the set of operating points in which the sensorless control is achievable with null or small estimation error as "feasible region" [27,30,31]. Exceeding the current limit imposed by the feasible region leads to the divergence of the position observer. It follows that the concepts of saliency ratio, estimation error and feasible region are consistent with the real behavior of a sensorless drive but not entirely explanatory. The convergence region theory, recently proposed, explains rigorously the performance of a sensorless drive including the divergence of the position observer in heavy saturation conditions. The ambitious task of extending the convergence region has been recently achieved [15, 16, 32, 33], but these kind of compensations are beyond the scope of this work.

The primary aim of this chapter is to provide a complete and systematic model to compute the self-sensing capabilities (saliency ratio, estimation error and convergence region) of a given motor starting from its flux linkages maps. Since such maps can be derived both experimentally and through simulations, the developed model is useful for both experimental sessions in lab (for example in the characterization of an existing motor) and during the design and development of new electric drives. It is also highlighted that the convergence region depends on both the reference trajectory for current control and the rotor position. Therefore, as a major contribution, this work proposes a clear and systematic approach for the computation of the convergence region of the sensorless drive.

The proposed model is supported by finite element analysis (FEA) and experimental validation on a SynRM and a PMA-SynRM.

2.2 Description of the considered motors

The motors considered in this work are a SynRM and a PMA-SynRM. The two prototypes have been designed for electric vehicle traction purpose, resulting in highly saturated motors [34]. Main data of the considered machines are shown in Table 2.1. The laminations of the two motors and the conventions used to define the

Table 2.1: Main data of the considered machines.

slots/poles	36/4	
rated power	2	kW
rated peak current	6	A
rated torque	16	Nm
rated speed	1400	rpm
stator resistance	4.6	Ω
d-axis apparent inductance	54	mH
q-axis apparent inductance	400	mH
stator outer diameter	200	mm
stator inner diameter	125	mm
air gap length	0.3	mm
stack length	40	mm
PM remanence (PMA-SynRM)	0.5	T

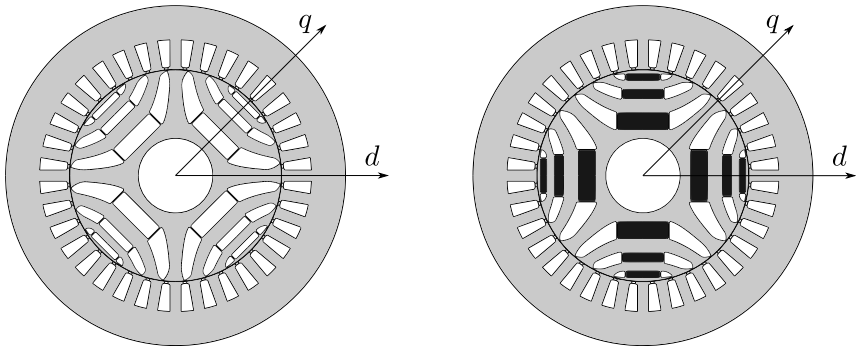

(a) SynRM (b) PMA-SynRM

Figure 2.1: Considered synchronous motors laminations and conventions.

d-*q* axes are shown in Figure 2.1. Signal-injection methods are designed to identify the position of an axis by exploiting the fact that its inductance is greater or less than the inductance of the other axis. Thus, the *d*-*q* axes convention must be taken carefully into account. Moreover, as will be shown in Sec. 2.3.5, the estimation error ε should be computed with two different equations depending on the adopted convention.

2.3 Modeling of synchronous machine

The structure of the current section represents a sistematic workflow to compute the self-sensing capabilities of a PMSM or SynRM starting from the flux linkages maps.

2.3.1 Flux linkages maps

Flux linkages maps are the first analysed in this work. Stator voltage equations of a PMSM or SynRM in the synchronous reference frame *d-q* can be expressed as:

$$\begin{aligned} u_d &= R\, i_d + \frac{d\lambda_d}{dt} - \omega_{me}\, \lambda_q \\ u_q &= R\, i_q + \frac{d\lambda_q}{dt} + \omega_{me}\, \lambda_d \end{aligned} \tag{2.1}$$

where R is the stator resistance, i_d and i_q the currents, λ_d and λ_q the flux linkages and ω_{me} the rotor electrical speed. Equations (2.1) are valid whatever convention is chosen (Figure 2.1).

The flux linkages λ_d and λ_q strictly depend on the operating point (i_d, i_q). The relationships $\lambda_d(i_d, i_q)$ and $\lambda_q(i_d, i_q)$ for a given motor can be found through FEA or experimental measurements. Several characterization techniques are reviewed in [35]. For both SynRM and PMA-SynRM, FEA and flux linkages measurements have been realized. The offline identification process required a prime mover motor to mantain a constant speed. The adopted method ensures that the flux linkages measuruments are not affected by the termal drift in stator resistance [36]. The flux linkages of SynRM are shown in Figure 2.2 and Figure 2.3. Regarding PMA-SynRM, the simulated and measured flux linkages are depicted in Figure 2.4 and Figure 2.6. Simulated and experimental maps have comparable shapes. Absolute error percentage between simulated and measured fluxes is about 10% along the iron axis and 20-30% along the flux barriers axis for both SynRM and PMA-SynRM.

As concerns the finite element simulations (Figure 2.2 and Figure 2.4), flux linkages have been evaluated for 30 rotor positions (i.e. one electrical periodicity) and, subsequently, the mean value has been computed and depicted. Regarding the experimental maps (Figure 2.3 and Figure 2.6), the flux linkages have been measured at constant speed, thus the average values on a rotor revolution are available.

Flux linkages maps, and consequently all the parameters obtainable from them, depend on both i_d and i_q but also on the rotor position θ_{me}. In fact, rotor rotation with respect to the stator introduces secondary effects such as spatial harmonics and local saturation due to the slotting. In the following, flux linkages maps are computed with FEA considering the average values on a rotor revolution (Figure 2.4). It is worth noting that the proposed computations can be extended for all rotor positions of interest.

2.3.2 Apparent inductances

Flux linkages, can be expressed as:

$$\begin{aligned} \lambda_d(i_d, i_q) &= L_d(i_d, i_q)\, i_d + \lambda_d(0, i_q) \\ \lambda_q(i_d, i_q) &= L_q(i_d, i_q)\, i_q + \lambda_q(i_d, 0) \end{aligned} \tag{2.2}$$

where L_d and L_q are the apparent inductances. It is worth noting that equation (2.2) has general validity. For both the conventions in Figure 2.1 the term $\lambda_q(i_d, 0)$ can be neglected since practically equal to 0. The same consideration is valid for the term $\lambda_d(0, i_q)$ in the case of SynRM.

Apparent inductances (or absolute inductances, [37]) represent the gradient of the flux linkages versus the currents respect to the origin. Rearranging (2.2) it is

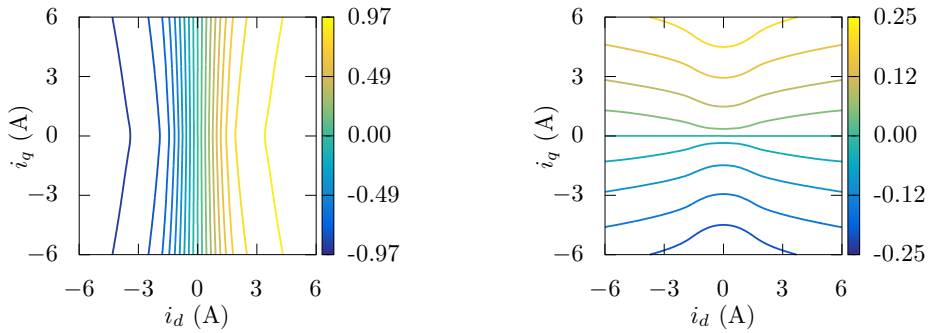

(a) $\lambda_d(i_d, i_q)$ (Vs) (b) $\lambda_q(i_d, i_q)$ (Vs)

Figure 2.2: Flux linkages λ_d, λ_q in the case of SynRM. Finite element analysis.

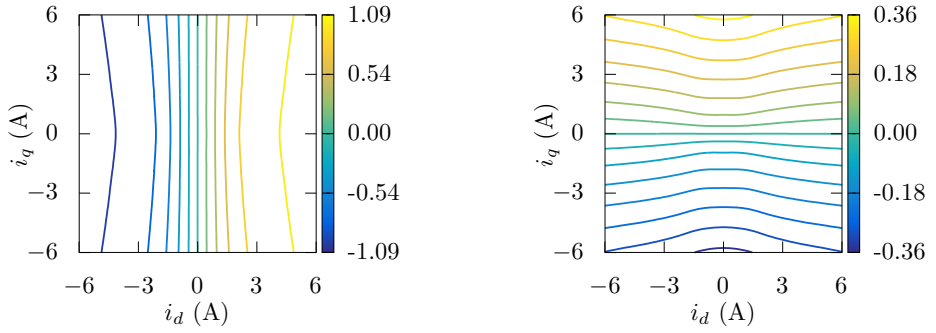

(a) $\lambda_d(i_d, i_q)$ (Vs) (b) $\lambda_q(i_d, i_q)$ (Vs)

Figure 2.3: Flux linkages λ_d, λ_q in the case of SynRM. Experimental measurements.

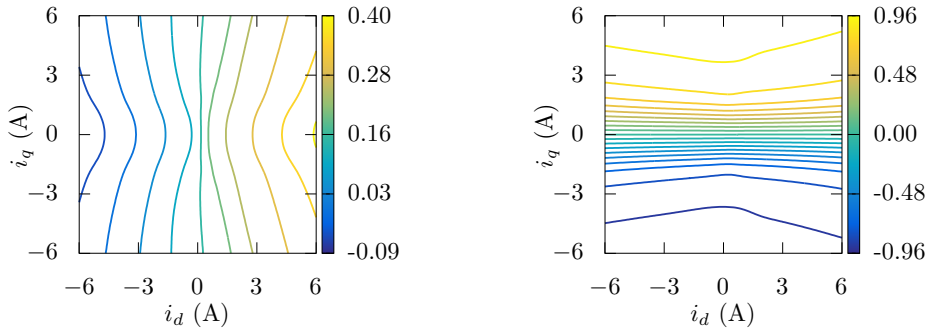

(a) $\lambda_d(i_d, i_q)$ (Vs) (b) $\lambda_q(i_d, i_q)$ (Vs)

Figure 2.4: Flux linkages λ_d, λ_q in the case of PMA-SynRM. Finite element analysis.

possible to obtain:

$$\begin{aligned} L_d(i_d, i_q) &= \frac{\lambda_d(i_d, i_q) - \lambda_d(0, i_q)}{i_d} \\ L_q(i_d, i_q) &= \frac{\lambda_q(i_d, i_q) - \lambda_q(i_d, 0)}{i_q} \end{aligned} \tag{2.3}$$

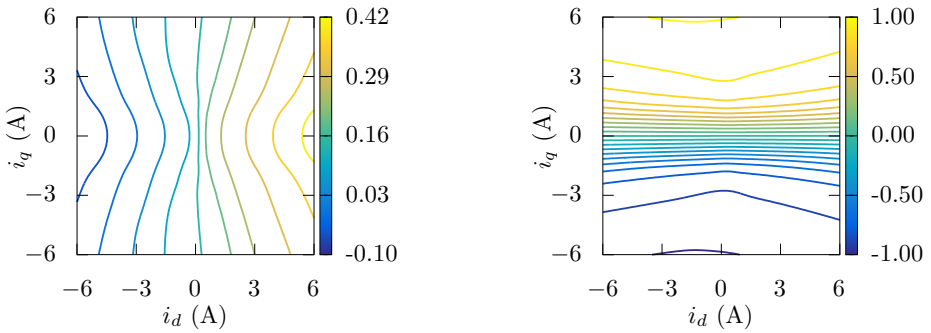

(a) $\lambda_d(i_d, i_q)$ (Vs) (b) $\lambda_q(i_d, i_q)$ (Vs)

Figure 2.5: Flux linkages λ_d, λ_q in the case of PMA-SynRM. Finite element analysis ($\theta_{me} = 0$).

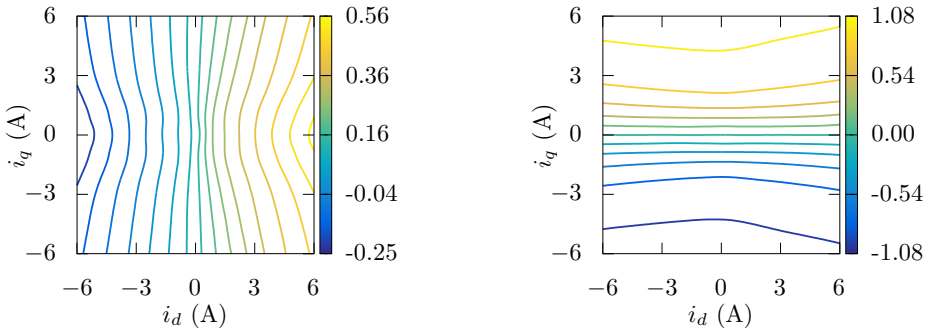

(a) $\lambda_d(i_d, i_q)$ (Vs) (b) $\lambda_q(i_d, i_q)$ (Vs)

Figure 2.6: Flux linkages λ_d, λ_q in the case of PMA-SynRM. Experimental measurements.

Differently to the incremental inductances (2.3.3) that can be calculated considering the variation of the fluxes between two adjacent working points, the apparent inductances are computed independently for each steady-state operating point. Figure 2.7 shows the apparent inductances of PMA-SynRM in the case of finite element analysis. Apparent inductances are useful for the computation of global quantities, such as the torque.

2.3.3 Incremental parameters

The incremental (or differential) inductances are the key parameters needed for the computation of the self-sensing capabilities of a considered synchronous machine (2.3.5). Two methods, both valid and with comparable results, for computing the incremental inductances using the finite element analysis can be found in literature, such as the small-signal model of the machine [38, 39] and the frozen permeability method [40].

In the following, incremental inductances are directly calculated as the local

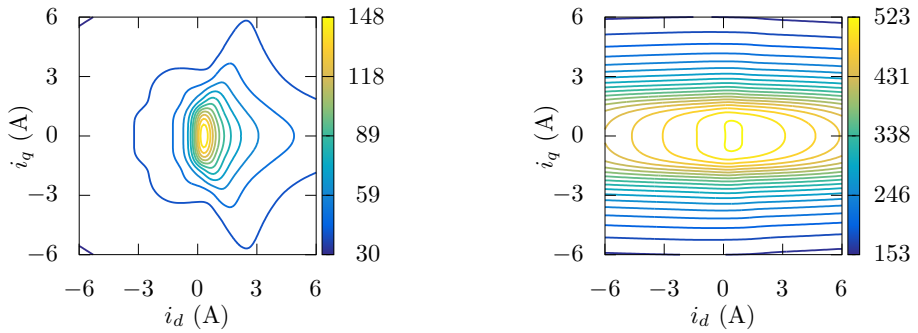

(a) $L_d(i_d, i_q)$ (mH) (b) $L_q(i_d, i_q)$ (mH)

Figure 2.7: PMA-SynRM apparent inductances maps (FEA).

derivatives of the flux linkages maps:

$$\begin{bmatrix} l_{dd}(i_d, i_q) & l_{dq}(i_d, i_q) \\ l_{qd}(i_d, i_q) & l_{qq}(i_d, i_q) \end{bmatrix} = \begin{bmatrix} \frac{\partial \lambda_d(i_d, i_q)}{\partial i_d} & \frac{\partial \lambda_d(i_d, i_q)}{\partial i_q} \\ \frac{\partial \lambda_q(i_d, i_q)}{\partial i_d} & \frac{\partial \lambda_q(i_d, i_q)}{\partial i_q} \end{bmatrix} \tag{2.4}$$

Figure 2.8 shows the incremental inductances computed for the PMA-SynRM. As expected, the cross-saturation inductance l_{dq} is equal to l_{qd}.

As regards the computation of the incremental inductances, the derivative of a matrix can be obtained in Python and MATLAB using either the function "diff" or the function "gradient". The function "diff" computes the derivative calculating the single-sided differences. The result is an array with smaller size than the array on which diff is computed. In particular, incremental inductances l_{dd} and l_{qd} (obtained applying diff along direction i_d) have one less row than the starting matrices λ_d and λ_q. On the other hand, incremental inductances l_{dq} and l_{qq} (obtained applying diff along direction i_q) have one less column than the starting matrices λ_d and λ_q. In order to guarantee the same number of rows and columns in all the matrices, one should duplicate the last row of l_{dd} and l_{qd} and the last column of l_{dq} and l_{qq}. Regarding "gradient", the function computes the derivative calculating central difference. The result of the differentiation with gradient is an array with the same size of the original fluxes. Moreover, the use of gradient has a smoothing effect in the resulting inductances.

A close correlation between L_d and l_{dd} can be noted (Figure 2.7a and Figure 2.8a), as well as between L_q and l_{qq} (Figure 2.7b and Figure 2.8d). The analytical relationship between the incremental and the apparent inductances can be

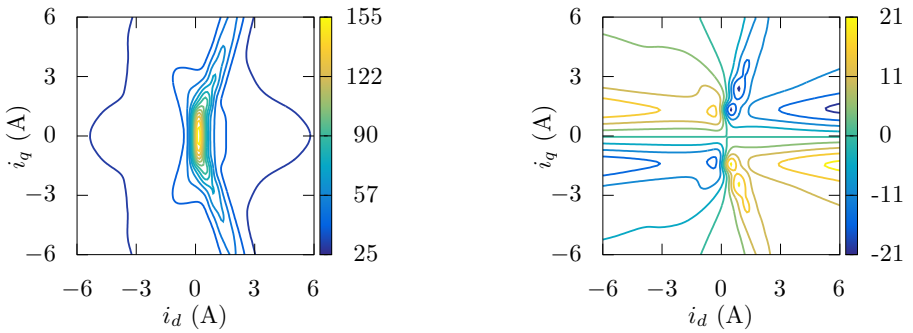

(a) $l_{dd}(i_d, i_q)$ (mH)

(b) $l_{dq}(i_d, i_q)$ (mH)

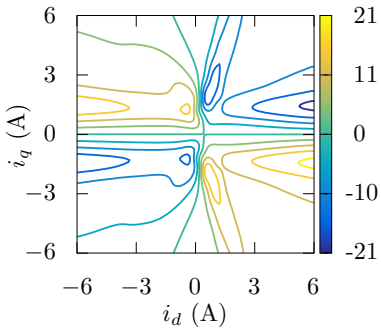

(c) $l_{qd}(i_d, i_q)$ (mH)

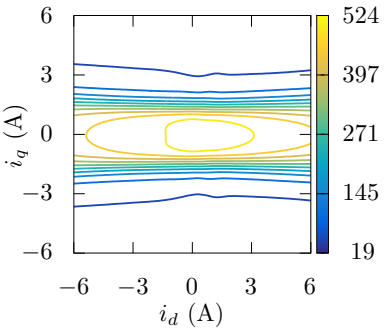

(d) $l_{qq}(i_d, i_q)$ (mH)

Figure 2.8: Incremental inductances $l_{dd}, l_{dq}, l_{qd}, l_{qq}$ in the case of PMA-SynRM (FEA).

obtained by applying the partial derivatives to (2.3):

$$\begin{aligned} l_{dd}(i_d, i_q) &= L_d(i_d, i_q) + \frac{\partial L_d(i_d, i_q)}{\partial i_d}\, i_d \\ l_{dq}(i_d, i_q) &= \frac{\partial \lambda_d(0, i_q)}{\partial i_q} + \frac{\partial L_d(i_d, i_q)}{\partial i_q}\, i_d \\ l_{qd}(i_d, i_q) &= \frac{\partial \lambda_q(i_d, 0)}{\partial i_d} + \frac{\partial L_q(i_d, i_q)}{\partial i_d}\, i_q \\ l_{qq}(i_d, i_q) &= L_q(i_d, i_q) + \frac{\partial L_q(i_d, i_q)}{\partial i_q}\, i_q \end{aligned} \tag{2.5}$$

It follows that:

$$\begin{aligned} L_d(i_d, i_q) &= \frac{\int l_{dq}(i_d, i_q)\, di_q \; - \; \lambda_d(0, i_q)}{i_d} \\ L_q(i_d, i_q) &= \frac{\int l_{qd}(i_d, i_q)\, di_d}{i_q} \end{aligned} \tag{2.6}$$

As stated in 2.3.2, the term $\lambda_q(i_d, 0)$ is equal to zero for a PMA-SynRM. In the case of SynRM, the terms $\lambda_d(0, i_q)$ and $\lambda_q(i_d, 0)$ are both zero. In the case of an ideal

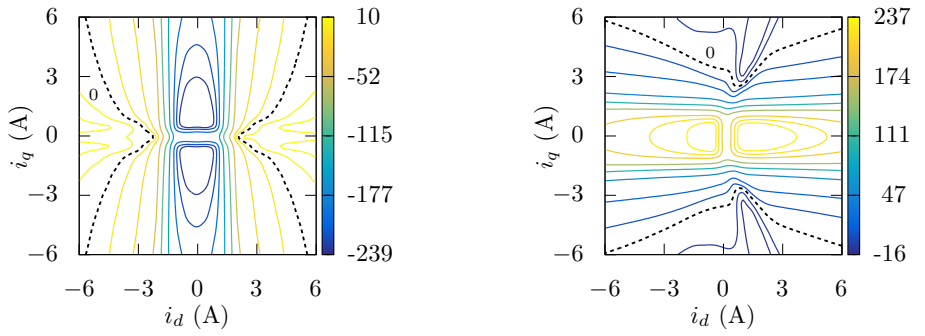

(a) $l_\Delta(i_d, i_q)$ (mH) SynRM

(b) $l_\Delta(i_d, i_q)$ (mH) PMA-SynRM

Figure 2.9: Semi-difference incremental inductance l_Δ computed with (2.7).

motor (linear flux linkages), it is clearly $l_{dd} = L_d = \text{const}$, $l_{qq} = L_q = \text{const}$ and $l_{dq} = l_{qd} = 0$.

The inductances l_Σ and l_Δ should be defined for the computation of the sensorless capabilities (2.3.5):

$$\begin{aligned} l_\Sigma(i_d, i_q) &= \frac{l_{qq}(i_d, i_q) + l_{dd}(i_d, i_q)}{2} \\ l_\Delta(i_d, i_q) &= \frac{l_{qq}(i_d, i_q) - l_{dd}(i_d, i_q)}{2} \end{aligned} \tag{2.7}$$

The incremental inductance l_Σ is the mean value between l_{dd} and l_{qq} in each operating point (i_d, i_q), while l_Δ is the semi-difference. Incremental inductance l_Δ in the case of SyRM and PMA-SynRM is depicted in Figure 2.9. The term l_Δ is related to the negative sequence of the current response to the high frequency injection [41,42]. Such negative sequence of the current response, which amplitude is proportional to $\sqrt{l_\Delta^2 + l_{dq}^2}$, contains the position information which is exploited for the rotor position estimation.

The area of $|l_\Delta \neq 0|$ has been reported as "feasible region" in literature because the sensorless control can operate safely and with acceptable estimation error within this region [26,27,30,31]. Many researchers consider the trajectory $l_\Delta = 0$ critical for sensorless control and crucial for the self-sensing capabilities assessment. Exceeding the current limit of the feasable region leads to a warning zone (characterized by high estimation error) and to a not feasable zone (with high risk of control divergence) [22]. Generally the definition of the feasible region is approximate and not rigorous. Moreover it has been found that sensorless operation is possible beyond the $l_\Delta = 0$ region adopting appropriate control strategies [31], thus the concept of feasible region should be revisited. Sec. 2.3.5 will focus on a novel concept, the convergence region computation, that fully explains the operation of a sensorless drive, i.e. the control of a motor when the estimated position is used in closed loop.

The incremental inductances matrix has been defined in (2.4). Computing the inverse of (2.4), it is possible to obtain:

$$\begin{bmatrix} \gamma_{dd}(i_d, i_q) & \gamma_{dq}(i_d, i_q) \\ \gamma_{qd}(i_d, i_q) & \gamma_{qq}(i_d, i_q) \end{bmatrix} = \begin{bmatrix} l_{dd}(i_d, i_q) & l_{dq}(i_d, i_q) \\ l_{qd}(i_d, i_q) & l_{qq}(i_d, i_q) \end{bmatrix}^{-1} \tag{2.8}$$

The incremental parameters γ_{xx} in the case of PMA-SynRM are depicted in Figure 2.10. The incremental parameters γ_{xx} can be directly computed from the incremental inductances l_{xx} expanding equation (2.8) into the following:

$$\begin{aligned}
\gamma_{dd}(i_d, i_q) &= \frac{l_{qq}(i_d, i_q)}{\Delta} \\
\gamma_{dq}(i_d, i_q) &= \frac{-l_{dq}(i_d, i_q)}{\Delta} \\
\gamma_{qd}(i_d, i_q) &= \frac{-l_{qd}(i_d, i_q)}{\Delta} \\
\gamma_{qq}(i_d, i_q) &= \frac{l_{dd}(i_d, i_q)}{\Delta}
\end{aligned} \tag{2.9}$$

where:

$$\Delta = l_{dd}(i_d, i_q)\, l_{qq}(i_d, i_q) - l_{dq}(i_d, i_q)\, l_{qd}(i_d, i_q) \tag{2.10}$$

The incremental parameters γ_{xx} are not necessary for the computation of the self-sensing capabilities. Actually, equations in 2.3.5 could be rewritten as function of the incremental parameters γ, but it would not be useful. The incremental parameters γ_{xx} defined in (2.8) can be used for creating the non-linear Simulink model with the current as state variable (appendix A).

2.3.4 Maximum Torque Per Ampere trajectory

The maximum torque per ampere (MTPA) trajectory for a considered motor can be obtained with offline and online methods [43, 44]. In this work, MTPA is calculated through derivation of the torque with respect to the current angle α_{ie}.

It is possible to consider the torque available with the finite element analysis (from Maxwell's stress tensor) or the dq torque obtainable with the following equation:

$$m(i_d, i_q) = \frac{3}{2}\, p\, [\lambda_d(i_d, i_q)\, i_q - \lambda_q(i_d, i_q)\, i_d] \tag{2.11}$$

where p is the number of pole pairs.

Figure 2.11a shows the PMA-SynRM torque obtained with finite element analysis. Once the torque is computed, the tangential derivative can be calculated as:

$$\frac{\partial m(i_d, i_q)}{\partial \alpha_{ie}} = -\frac{\partial m(i_d, i_q)}{\partial i_d}\, i_q + \frac{\partial m(i_d, i_q)}{\partial i_q}\, i_d \tag{2.12}$$

The torque derivative with respect to the current angle, in the case of PMA-SynRM, is depicted in Figure 2.11b. The dashed lines represent the locus where the torque derivative is zero. For a PMA-SynRM the MTPA is located in the second quadrant. The MTPA trajectory can be extracted from the map in Figure 2.11b and expressed in cartesian coordinates as in Figure 2.12a. For the computation of the convergence region (2.3.5), it is useful to express the MTPA trajectory in polar coordinates as shown in Figure 2.12b. For a SynRM the MTPA trajectory is equivalently in the first and third quadrant of the d-q plane.

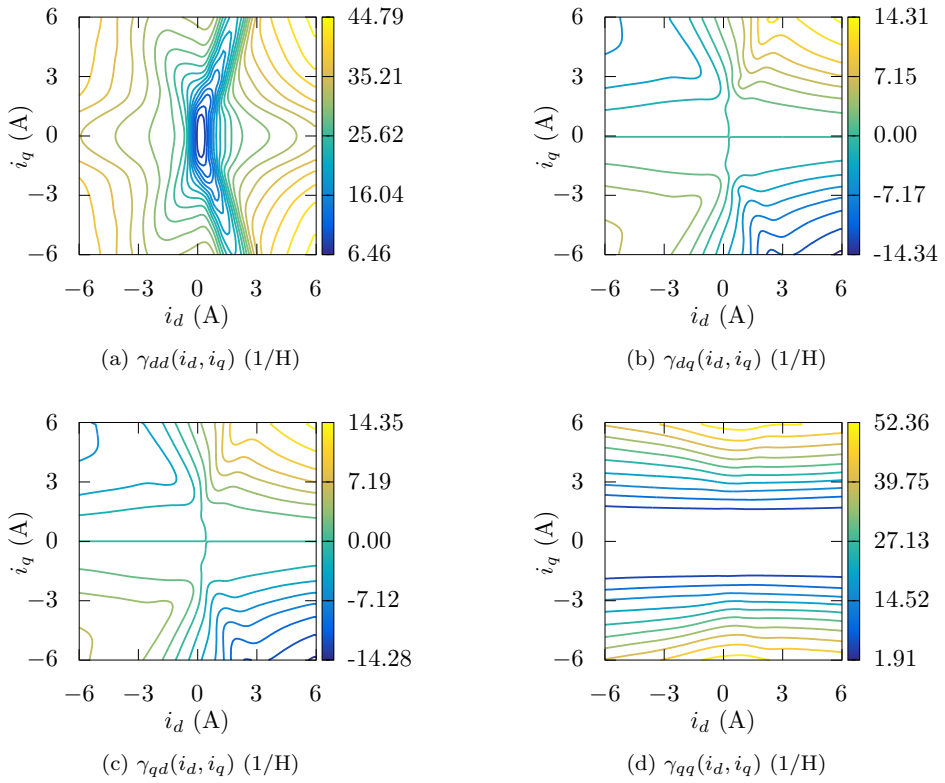

(a) $\gamma_{dd}(i_d, i_q)$ (1/H) (b) $\gamma_{dq}(i_d, i_q)$ (1/H)

(c) $\gamma_{qd}(i_d, i_q)$ (1/H) (d) $\gamma_{qq}(i_d, i_q)$ (1/H)

Figure 2.10: PMA-SynRM inverse incremental inductances maps (finite element analysis). (a) $\gamma_{dd}(i_d, i_q)$ (b) $\gamma_{dq}(i_d, i_q)$ (c) $\gamma_{qd}(i_d, i_q)$ (d) $\gamma_{qq}(i_d, i_q)$

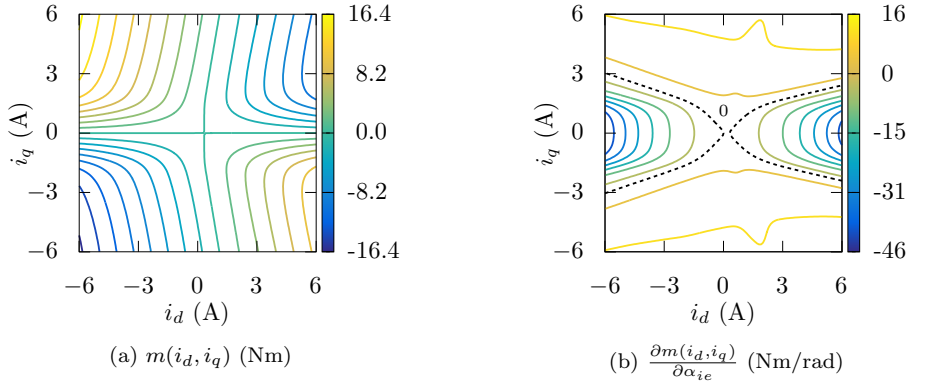

(a) $m(i_d, i_q)$ (Nm) (b) $\frac{\partial m(i_d, i_q)}{\partial \alpha_{ie}}$ (Nm/rad)

Figure 2.11: Torque m (on the left) and torque derivative $\frac{\partial m}{\partial \alpha_{ie}}$ (on the right) in the case of PMA-SynRM.

The MTPA can also be computed analytically [45] considering the torque equa-

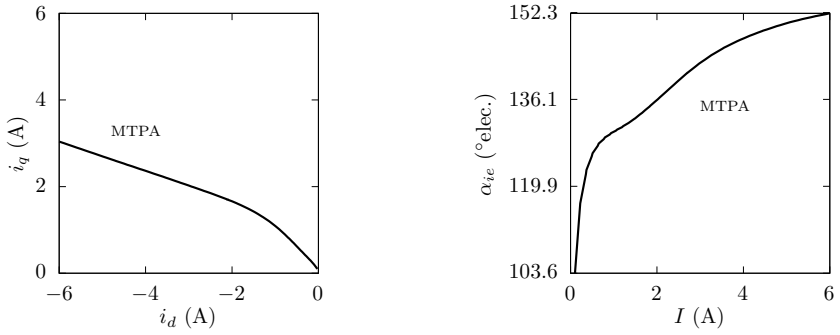

(a) MTPA in the d-q plane.

(b) MTPA in polar coordinates

Figure 2.12: MTPA in the case of PMA-SynRM.

tion (2.11) obtaining:

$$\frac{\partial m(i_d, i_q)}{\partial \alpha_{ie}} = 2\, l_{dq}(i_d, i_q)\, i_d\, i_q - (l_{dd}(i_d, i_q)\, i_q^2 + l_{qq}(i_d, i_q)\, i_d^2) + \lambda_d(i_d, i_q)\, i_d + \lambda_q(i_d, i_q)\, i_q \quad (2.13)$$

or, equivalently:

$$\frac{\partial m(i_d, i_q)}{\partial \alpha_{ie}} = 2\, l_{dq}(i_d, i_q)\, i_d\, i_q - \left[l_{dd}(i_d, i_q)\, i_q^2 + l_{qq}(i_d, i_q)\, i_d^2\right] + L_d(i_d, i_q)\, i_d^2 + L_q(i_d, i_q)\, i_q^2 + \lambda_d(0, i_q)\, i_d + \lambda_q(i_d, 0)\, i_q \quad (2.14)$$

2.3.5 Self-sensing capabilities

In this section, the computation of saliency ratio, estimation error (in open loop) and convergence region are explained. Saliency ratio and estimation error are commonly referred to as self-sensing capabilities [27–29, 46, 47]. The concept of "convergence region" [15, 16] replaces the concept of "feasible region" [27, 30, 31] as it is more rigorous and explanatory.

The saliency ξ is the ratio between the major and minor semi-axes lengths, s_M (1.32) and s_m (1.33), of the current response to the high frequency rotating voltage injection [22, 47] and it can be defined as:

$$\xi(i_d, i_q) = \frac{l_\Sigma(i_d, i_q) + \sqrt{l_\Delta^2(i_d, i_q) + l_{dq}^2(i_d, i_q)}}{l_\Sigma(i_d, i_q) - \sqrt{l_\Delta^2(i_d, i_q) + l_{dq}^2(i_d, i_q)}} \quad (2.15)$$

The saliency ratio can be computed as $\xi = \frac{l_{qq}}{l_{dd}}$ when the cross-saturation inductance l_{dq} is neglected [27]. The saliency ratio in the case of SynRM and PMA-SynRM is depicted in Figure 2.13. Theoretically, a saliency ratio $\xi > 1$ makes the position estimation possible. In practice, the area in which the saliency is little greater than one can be considered critical for the position estimation using saliency tracking methods.

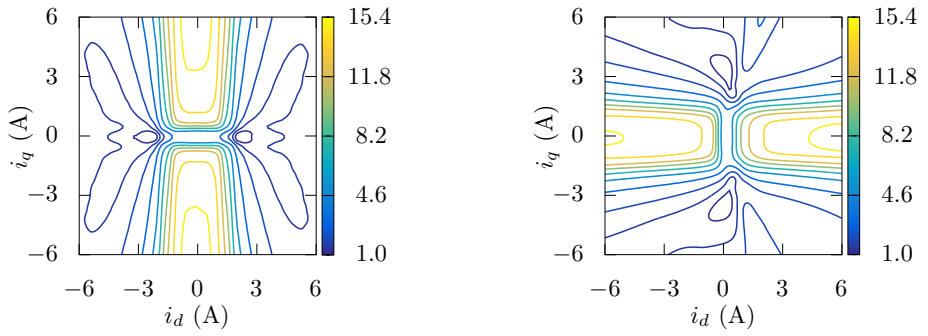

(a) $\xi(i_d, i_q)$ SynRM (b) $\xi(i_d, i_q)$ PMA-SynRM

Figure 2.13: Saliency ratio ξ computed with (2.15).

The estimation error ε is the second parameter related to the self-sensing capabilities which can be predicted from the incremental inductances. Without applying any compensation, the position observer of any signal injection method will never be able to estimate θ_{me}, because of the altered response of the machine due to the cross-saturation. What can be estimated is $\widetilde{\theta}_{me}$, where:

$$\widetilde{\theta}_{me}(i_d, i_q) = \theta_{me} + \varepsilon(i_d, i_q) \tag{2.16}$$

$\widetilde{\theta}_{me}$ is the rotor position θ_{me} altered by the presence of the estimation error ε [15, 16, 23]. It appears that the estimated position corresponds exactly to $\widetilde{\theta}_{me}$ at steady state, that is the reason why ε is called estimation error. Inevitably during transients the estimated position can assume other values. Estimation error ε can be computed as:

$$\varepsilon = \begin{cases} \frac{1}{2}\ \text{atan2}(-l_{dq}, l_\Delta) = \arctan\left(\frac{-l_{\mathrm{dq}}}{l_\Delta + \sqrt{l_\Delta^2 + l_{\mathrm{dq}}^2}}\right), & \text{for PMA-SynRM} \\ \frac{1}{2}\ \text{atan2}(l_{dq}, -l_\Delta) = \arctan\left(\frac{l_{\mathrm{dq}}}{-l_\Delta + \sqrt{l_\Delta^2 + l_{\mathrm{dq}}^2}}\right), & \text{for SynRM} \end{cases} \tag{2.17}$$

and it results a function of i_d, i_q as l_{dq} and l_Δ. Estimation error ε for SynRM and PMA-SynRM is shown in Figure 2.14. It is worth noting that a critical area where the estimation error abruptly skips from $-90°$ to $90°$ exist. This region should be avoided to guarantee a safe sensorless control operation.

Conventional PMSM control requires a reference trajectory to be chosen for the current control loop. The current amplitude reference I_{REF}, generated by the speed control loop, is converted to the projections $i_{d\,REF}$ to $i_{q\,REF}$ following the current reference trajectory, which usually corresponds to the MTPA.

Definition of trajectory t_1

During a sensored operation, the measured position is used to control the motor along the reference trajectory. The position observer, if present, is set in open-loop thus the estimated position is not used for control, but only monitored. The estimated position will be different from the measured one because of the presence of

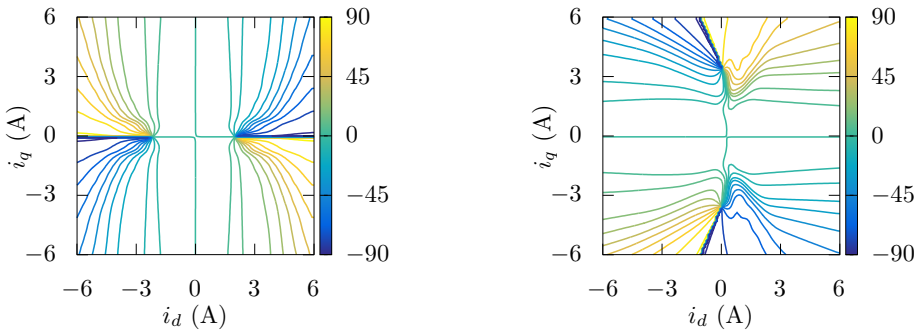

(a) $\varepsilon(i_d, i_q)$ (°) SynRM

(b) $\varepsilon(i_d, i_q)$ (°) PMA-SynRM

Figure 2.14: Estimation error (in open loop) ε computed with (2.17).

the cross-saturation effect. In other words, the trajectory drawn by the observer in open loop during a sensored operation, hereafter called sensored trajectory t_1, will be different from the reference trajectory. The sensored trajectory t_1 can be predicted starting from the open loop estimation error ε (Figure 2.14b) and the reference trajectory REF (Figure 2.12a). The procedure to compute the sensored trajectory t_1 in the case of PMA-SynRM is described with the help of Figure 2.15. At first, the estimation error map has to be interpolated along the reference trajectory, leading to $\varepsilon(I)$ (Figure 2.15a). Then, $\varepsilon(I)$ has to be added to the reference trajectory itself, leading to the sensored trajectory t_1 (Figure 2.15b). It is possible to notice that the observer trajectory t_1 is close to the reference only for low current amplitudes, i.e. when $l_{dq} \approx 0$ thanks to the low saturation level. Increasing the current amplitude, t_1 progressively moves away from the reference trajectory because of the increase of the cross-saturation and, consequently, of the absolute value of $\varepsilon(I)$. It is relevant noting that t_1 is a fictitious trajectory. A position sensor is required to cover the reference trajectory REF and draw the observer trajectory t_1.

Definition of trajectory t_2

During a sensorless operation, no position sensor is used. While in the sensored control the estimation error afflicts only the estimated position but not the operating point, during a sensorless operation the control loop is closed with the estimated angle and so the operating point is afflicted by the estimation error ε. In particular, the motor operates along a trajectory different from the desired reference one. This trajectory, hereafter called sensorless trajectory t_2, can be computed following the next steps:

- computation of $\Delta\theta(i_d, i_q)$
- computation of $I_{hq}(i_d, i_q)$
- computation of $I_{hq}(i_d, i_q) = 0$ and $\frac{\partial I_{hq}(i_d, i_q)}{\partial \alpha_{ie}} < 0$

As will be clarified shortly, the sensorless trajectory t_2 is just one of the trajectories belonging to the convergence region.

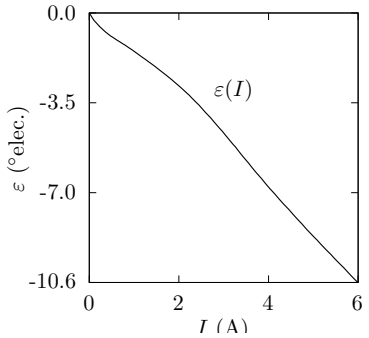

(a) Estimation error ε computed along the reference trajectory, in polar coordinates.

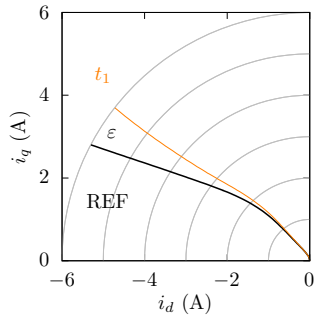

(b) Given REF trajectory and computed t_1 trajectory, in the d-q plane.

Figure 2.15: Procedure to compute the sensored trajectory t_1 given the reference trajectory REF. The first step consists in computing the estimation error ε along the the reference trajectory (on the left). The second step consists in adding ε to reference trajectory itself (on the right).

The first step consists in computing $\Delta\theta(i_d, i_q)$ over a portion of i_d-i_q plane as:

$$\Delta\theta(i_d, i_q) = \alpha_{ie}(i_d, i_q) - \theta_{REF}(I) \tag{2.18}$$

where $\alpha_{ie}(i_d, i_q) = \text{atan2}(i_q, i_d)$ and $I(i_d, i_q) = \sqrt{i_d^2 + i_q^2}$. The term $\theta_{REF}(I)$ can be obtained from the reference trajectory expressed in polar coordinates (Figure 2.12b). Figure 2.16a shows the computation of $\Delta\theta$ for an example point (-1,4) in the i_d-i_q plane. It is possible to notice that, given a point in d-q plane, $\Delta\theta$ is the angle between the point itself and the reference trajectory (REF) with the same current amplitude. $\Delta\theta$ has to be evaluated for all the current points where it is interesting to investigate the self-sensing capabilities of the considered sensorless drive.

Once computed $\Delta\theta(i_d, i_q)$, the map of $I_{hq}(i_d, i_q)$, i.e. the amplitude of the input signal of the position estimation observer (1.22), can be computed as:

$$I_{hq} = -\frac{U_h}{2\pi f_h} \frac{\sqrt{l_\Delta^2 + l_{dq}^2}}{l_{dd}\, l_{qq} - l_{dq}^2} \sin(2\Delta\theta - 2\varepsilon) \tag{2.19}$$

where U_h and f_h are the amplitude and the frequency of the high-frequency injected voltage. The map of $I_{hq}(i_d, i_q)$ in the case of PMA-SynRM and MTPA chosen as current reference is shown in Figure 2.16b. Being the position estimation observer a PI controller (Figure 1.4, 1.6, 2.17), the convergence of the position estimation is found once the input signal I_{hq} is nullified. In practice, the position observer varies its output (the angle of the estimated position) until the zero-crossing of the input I_{hq} is found. In Figure 2.16b, the locus $I_{hq} = 0$ is depicted in dashed lines. The whole locus $I_{hq} = 0$ includes both stable and unstable convergence points of the observer. Only the stable points of the locus $I_{hq} = 0$ can be defined as convergence region. In particular, the convergence region is the subset of points of $I_{hq} = 0$ characterized by negative slope with respect to the current angle. Thus, the tangential derivative of I_{hq} has to be computed in order to extract the convergence region.

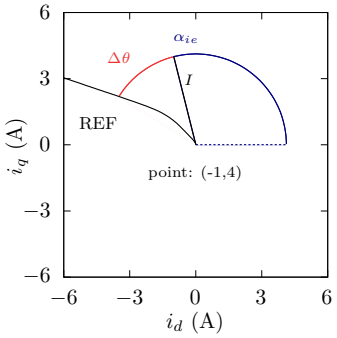

(a) Computation of $\Delta\theta$ for the example point (-1,4)

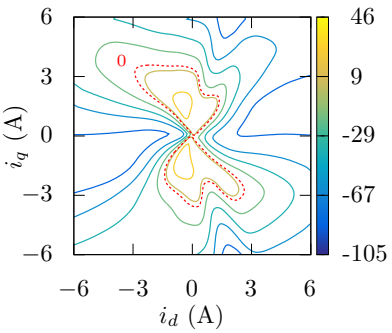

(b) $I_{hq}(i_d, i_q)$ (mA)

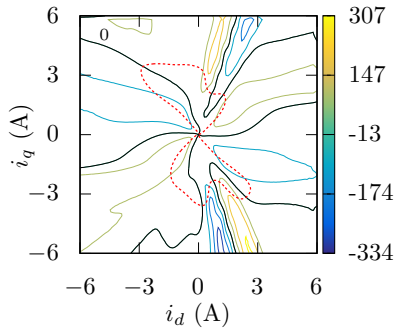

(c) $\frac{\partial I_{hq}(i_d,i_q)}{\partial \alpha_{ie}} \left(\frac{\text{mA}}{\text{rad}}\right)$

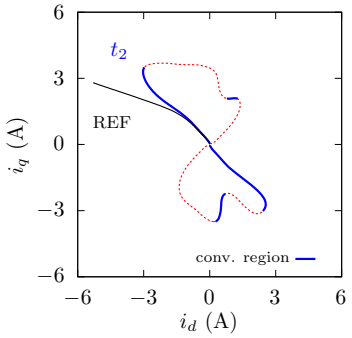

(d) Reference trajectory REF, convergence region and sensorless trajectory t_2.

Figure 2.16: Procedure to compute the convergence region and the sensorless trajectory t_2. The first step consists in computing $\Delta\theta$ for all the current points with (2.18) (top-left). The second step consists in computing I_{hq}, input of the position observer, using (2.19) (top-right). The third step consists in computing the derivative of I_{hq} with respect to the current angle with (2.20) (bottom-left). The last step consists in extracting the convergence region from $I_{hq} = 0$ (bottom-right). The sensorless trajectory t_2 is the first part of the convergence region, depicted in blue.

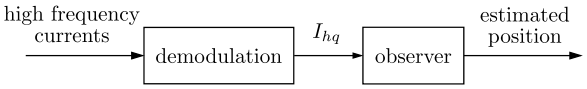

Figure 2.17: Conventional demodulation and position observer scheme for signal-injection sensorless control. I_{hq} is the input of the position observer or, equivalently, the output of the demodulation process.

The derivative of I_{hq} with respect to the current angle can be computed as:

$$\frac{\partial I_{hq}(i_d, i_q)}{\partial \alpha_{ie}} = -\frac{\partial I_{hq}(i_d, i_q)}{\partial i_d} i_q + \frac{\partial I_{hq}(i_d, i_q)}{\partial i_q} i_d \tag{2.20}$$

The map of the tangential derivative of I_{hq} is depicted in Figure 2.16c. Stable

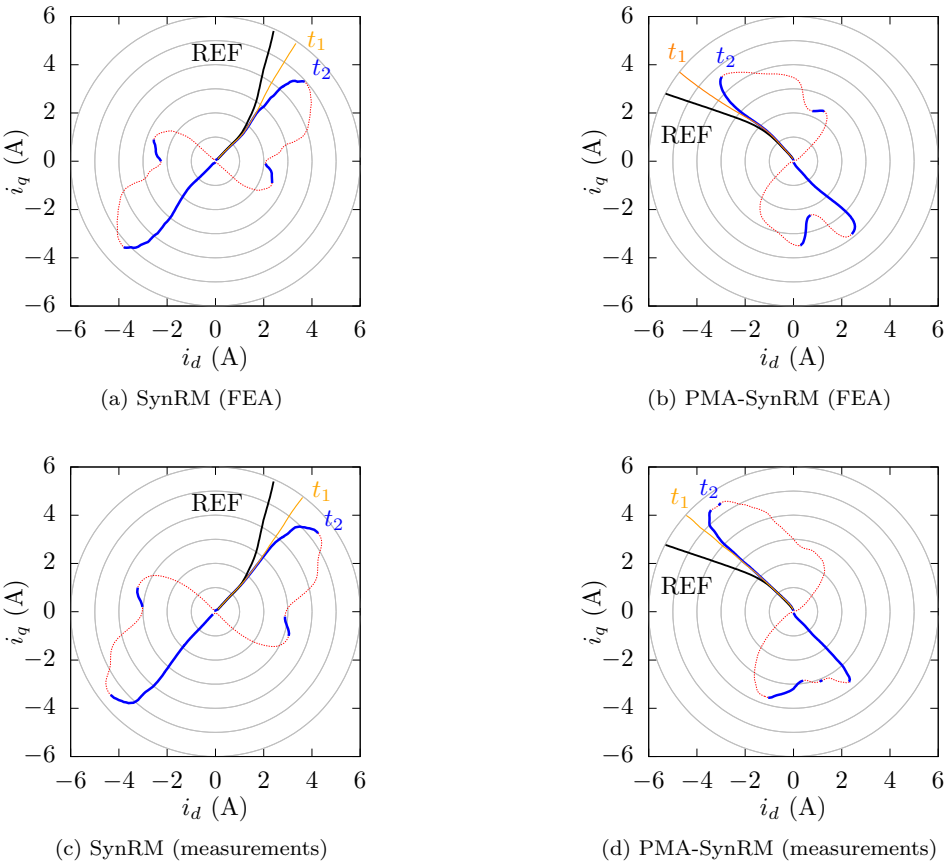

(a) SynRM (FEA)

(b) PMA-SynRM (FEA)

(c) SynRM (measurements)

(d) PMA-SynRM (measurements)

Figure 2.18: Results of the proposed computations on 4 different datasets. t_1 is a fictitious trajectory representing the output of the position observer (in open loop) during a sensored operation along the reference trajectory REF. t_2 is the effective trajectory in sensorless operation, with the estimated position used in closed loop. In blue the set of points of $I_{hq} = 0$ with negative slope (i.e. the convergence region). In red the set of points of $I_{hq} = 0$ with positive slope.

convergence points of $I_{hq} = 0$ can be found where the tangential derivative of I_{hq} is negative. The convergence region (Figure 2.16d) is obtained computing the intersection between the conditions $I_{hq}(i_d, i_q) = 0$ and $\frac{\partial I_{hq}(i_d,i_q)}{\partial \alpha_{ie}} < 0$. As shown in Figure 2.16d, the sensorless trajectory t_2 is just the first part, starting from the origin, of the convergence region. It represents the trajectory of the effective operating points controlling the motor in sensorless operation, i.e. closing the control on the estimated rotor position. As long as the negative-slope zero-crossing of I_{hq} with respect to the current angle α_{ie} exists, the position can be estimated. When a motor is highly saturated, I_{hq} does not cross zero for any current angle and the trajectory t_2 stops. The length of t_2 can be considered as the operational limit of a signal-injection sensorless drive. Sensorless-oriented motor design should focus on making the trajectory t_2 as close as possible to the reference REF.

Figure 2.18 shows the convergence regions of SynRM and PMA-SynRM computed both on simulated and measured flux linkages maps. MTPA is set as current reference. Moreover, in each picture, the sensored trajectoy t_1 and the sensorless trajectory t_2 are depicted. Convergence regions obtained from SynRM simulated and measured flux maps appears to be very similar (Figure 2.18a and Figure 2.18c). The maximum length of trajectory t_2 is about 5 A, meaning that theoretically (assuming ideal conditions like steady-state operations and absence of noise) the considered motor can operate in sensorless operation up to this current amplitude (without adopting compensations). As concerns the PMA-SynRM, sensorless trajectory t_2 reaches 4.5 A in the case of simulated flux maps (Figure 2.18b) and 5.5 A in the case of measured flux maps (Figure 2.18d). Considering that both motors have a rated current of 6 A, from Figure 2.18 it is possible to predict that compensation techniques [15, 16, 32, 33] are required to reach at least the rated current. Compensation is needed firstly to extend the operational limit and secondly to guarantee the sensorless operating trajectory is close as possible to the reference trajectory. It is worth noting that the proposed computation approach of the convergence region is valid for different reference trajectories. Thus, a simplified MTPA trajectory or any other trajectory can be chosen depending on the requirements.

2.4 Conclusion

In this chapter, a complete and systematic model of synchronous machines has been presented and adopted for computing the convergence region of a sensorless drive. The starting point for the analysis are the motor flux linkages maps. The self-sensing capability of the drive has been described by the difference between the sensored and the sensorless operation trajectories, t_1 and t_2 respectively. Both the trajectories can be evaluated offline starting from simulation results or experimental tests.

Chapter 3

Convergence Region Measurement

Abstract - In this chapter, a measurement procedure of the convergence region, i.e. the operating points where the motor can be successfully controlled without a position sensor, of a PMSM sensorless drive is presented and validated [48].

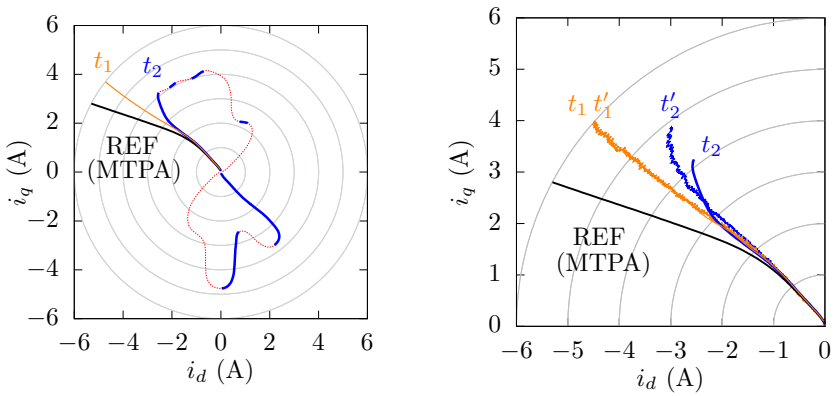

(a) Computed convergence region

(b) Measured convergence region

Figure 3.1: (a) Convergence region computed from the simulated flux linkages maps (FEA) for $\theta_{me} = 0$, using the method presented in 2.3.5. (b) Convergence region measured with the proposed method.

3.1 Introduction

In this work, an experimental procedure to measure the self-sensing capability of a synchronous sensorless drive is proposed. During the first measurement, the sensored trajectory t_1 (the trajectory of the position observer in open-loop during a sensored operation) is detected. During the second measurement, the sensorless trajectory t_2 (the trajectory of the effective operating points controlling the motor in sensorless operation) is obtained. The proposed experimental procedure is compared and validated with finite element analysis (FEA) results. The original contributions presented in this work are:

- The explanation of the dependency of the actual control trajectory (t_2) on the considered reference trajectory.
- An experimental validation to measure and give clear evidence to such a dependancy.

3.2 Considered motor

A PMA-SynRM is considered in this work. The geometry and the convention adopted to define the rotor reference frame are shown in Figure 2.1b, while Table 2.1 summarizes the main data of the considered machine. The motor has been characterized for rotor position $\theta_{me} = 0$ through FEA. The corresponding flux linkages λ_d and λ_q are shown in Figure 2.5.

Figure 3.1a shows the convergence region of the considered PMA-SynRM computed on the simulated flux linkages maps. The sensored trajectory t_1 moves away from the MTPA reference for increasing current values because of the cross-saturation effect on the estimated rotor position [23]. As can be noticed, the sensorless trajectory t_2 has a shorter length than t_1 because it exists a working point

(a) Locked PMA-SynRM

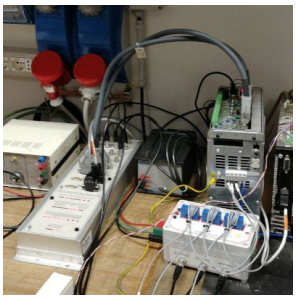

(b) dSPACE1104 and inverter

Figure 3.2: Experimental setup.

beyond which the observer is not able to estimate the rotor position leading to the sensorless control divergence [15]. The maximum length of trajectory t_2 is about 4 A, meaning that the considered motor can operate in sensorless operation up to this current amplitude (without adopting compensations). For higher current values it is not possible to estimate the rotor position, and additional compensations should be adopted [15, 16, 32, 33].

3.3 Proposed method explanation

In Figure 3.1a the sensored trajectory t_1 and the sensorless trajectory t_2 have been computed through post-processing computations on the FEA maps. In the following, the trajectories t_1' and t_2' will be recorded online during two experimental tests (the first sensored and the second sensorless) using the MTPA as reference trajectory for the current control. The tests have been performed on the test bench shown in Figure 3.2, where the PMA-SynRM has been locked at $\theta_{me} = 0$. The control scheme has been implemented on a dSPACE1104 using a control frequency of 10 kHz. The amplitude of the voltage injection is $U_h = 40$ V, and the injection frequency is $f_h = 1$ kHz. The cut-off frequency has been set to 100 Hz for both high-pass filters (HPF) and the low-pass filters (LPF) in the control scheme of Figure 1.7.

3.3.1 Trajectory t_1 measurement

The first test is performed in sensored mode: the measured position $\theta_{me} = 0$ is used for the current control (the swith in Figure 1.7 is on position 1) while the estimated position $\widetilde{\theta}_{me}$ and the currents i_d and i_q are used for the online computation of the trajectory t_1'. The coordinates of trajectory t_1', i.e. the currents in the estimated $\mathrm{d}^x\mathrm{q}^x$ reference frame i_d^x and i_q^x, are so computed:

$$i_d^x = i_d \cos(\widetilde{\theta}_{me} - \theta_{me}) - i_q \sin(\widetilde{\theta}_{me} - \theta_{me}) \tag{3.1a}$$

$$i_q^x = i_d \sin(\widetilde{\theta}_{me} - \theta_{me}) + i_q \cos(\widetilde{\theta}_{me} - \theta_{me}) \tag{3.1b}$$

It is worth noting that in this test the difference between the estimated position $\widetilde{\theta}_{me}$ and the measured position θ_{me} is the open-loop estimation error ε (2.17). Figure 3.3a

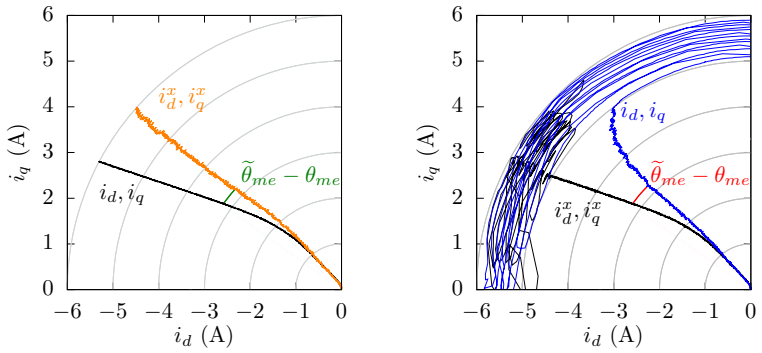

(a) t_1' measurement procedure

(b) t_2' measurement procedure

Figure 3.3: (a) Trajectory t_1' (i_d^x, i_q^x) computation procedure represented on the cartesian plane. (b) Trajectory t_2' (i_d, i_q) computation procedure represented on the cartesian plane.

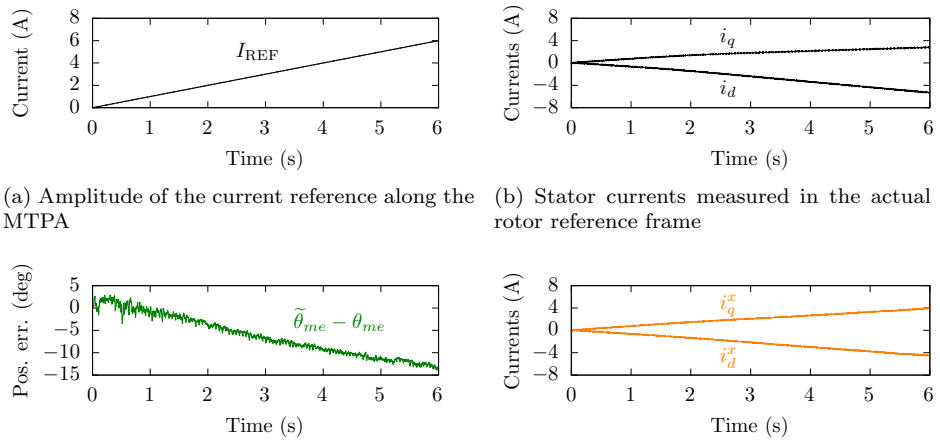

(a) Amplitude of the current reference along the MTPA

(b) Stator currents measured in the actual dq rotor reference frame

(c) Difference between estimated and measured rotor position

(d) Stator currents computed in the shifted $\mathrm{d}^x\mathrm{q}^x$ reference frame

Figure 3.4: Trajectory t_1' measurement procedure represented as a function of time. The currents i_d, i_q and the estimated position in open-loop $\widetilde{\theta}_{me}$ are used to compute the currents i_d^x, i_q^x. The rotor is locked at $\theta_{me} = 0$.

shows the results of the first test represented on the *d*-*q* plane. The test consists in controlling the motor using as reference a current ramp, along the MTPA, growing at rate of 1 A per second. In fact, the operating points represented by the measured currents i_d and i_q follow the trajectory MTPA from (0,0) up to the rated current amplitude value (6 A). The trajectory t_1', which coordinates are the currents i_d^x and i_q^x, is shifted with respect to the reference trajectory of a growing angle equal to ε. The results of the first test are represented also as a function of time. Figure 3.4a shows the amplitude of the current reference growing at rate of 1 A per second.

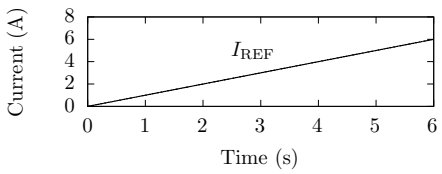

(a) Amplitude of the current reference along the MTPA

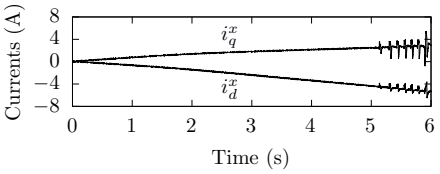

(b) Stator currents measured in the shifted $\mathrm{d}^x\mathrm{q}^x$ reference frame

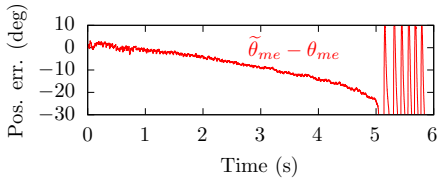

(c) Difference between estimated and measured rotor position

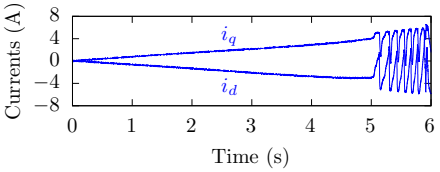

(d) Stator currents in the actual dq reference frame

Figure 3.5: Trajectory t_2' measurement procedure represented as a function of time. The currents i_d^x, i_q^x and the estimated position in closed-loop $\widetilde{\theta}_{me}$ are used to compute the currents i_d, i_q. The rotor is locked at $\theta_{me} = 0$.

Figure 3.4b shows the measured currents i_d and i_q. Figure 3.4c shows the estimation error, which is null at zero currents and increases up to -15 electrical degrees at the rated current amplitude. Finally, Figure 3.4d shows the coordinates of trajectory t_1'.

3.3.2 Trajectory t_2 measurement

Contrary to the first test, the second test is performed in sensorless mode: the estimated position $\widetilde{\theta}_{me}$ is used for the current control (the switch in Figure 1.7 is in position 2) while the measured position $\theta_{me} = 0$ and the currents i_d^x and i_q^x are used for the online computation of the trajectory t_2'. The coordinates of trajectory t_2', i.e. the currents in the actual dq reference frame i_d and i_q, are so computed:

$$i_d = i_d^x \cos(\widetilde{\theta}_{me} - \theta_{me}) - i_q^x \sin(\widetilde{\theta}_{me} - \theta_{me}) \tag{3.2a}$$

$$i_q = i_d^x \sin(\widetilde{\theta}_{me} - \theta_{me}) + i_q^x \cos(\widetilde{\theta}_{me} - \theta_{me}) \tag{3.2b}$$

The results of the second test are shown both on the *d*-*q* plane (Figure 3.3b) and as a function of time (Figure 3.5). The test consists in controlling the motor in sensorless mode using as reference a current ramp, along the MTPA, growing at rate of 1 A per second. Since the current control is closed on estimated position $\widetilde{\theta}_{me}$, the operating reference frame is the estimated $\mathrm{d}^x\mathrm{q}^x$. The measured currents i_d^x and i_q^x appear to follow the MTPA reference in the shifted control frame, but the real operating point is in a different place (t_2'). The actual operating point i_d-i_q is different from the trajectory covered in the first test (the MTPA), thus during a sensorless test - in which no compensations are actuated - the motor is actually controlled along a

wrong load-dependent current reference. Since the motor parameters are not linear and depend on the operating point, the trajectory t'_2 cross a region of the d-q plane where the inductances l_{dq} and l_Δ are different from those encountered along the MTPA trajectory. As a consequence of that, it is possible to notice that the closed-loop estimation error in Figure 3.5c is different from the open-loop estimation error in Figure 3.4c. While the open-loop estimation ε error has a direct expression (2.17), the closed-loop estimation error requires some additional steps to be computed. In particular, the sensorless trajectory t_2 can be computed from the signal I_{hq}, defined in (2.19). As concerns the trajectory t'_2 recorded during the second test, it is possible to notice that it is more distant from the MTPA than the sensored trajectory t'_1. Moreover, at a current amplitude of 5 A (at time 5 s) the control diverges. This can be noted also in oscillations of i_d^x and i_q^x (in Figure 3.5b), of i_d and i_q (in Figure 3.5d), and of $\widetilde{\theta}_{me}$ (in Figure 3.5c). The phenomenon of sensorless control divergence happens in the regions of the d-q plane where the signal I_{hq} does not cross the zero for any current angle [15]. When the position estimation and the control are lost, the sensorless drive becomes unusable.

To conclude, the trajectories computed during the experimental tests are compared and validated with the trajectories obtained from the FEA flux-linkages maps. The comparison is done considering t_1 and t_2 (from Figure 2.18), t'_1 (from Figure 3.3a), and t'_2 (from Figure 3.3b). In Figure 3.1b it is possible to appreciate that standstill operation and quasi-steady-state current control make the experimental results (t'_1 and t'_2) comparable with the ones predicted assuming an ideal control (t_1 and t_2). In particular, the sensored trajectories t_1 and t'_1 are perfectly coincident. Regarding the sensorless trajectories, the FEA trajectory t_2 is truncated at a current amplitude of 4 A while the experimental trajectory t'_2 reaches the current amplitude of 5 A. The control diverges for a current amplitude inferior to the rated value in both cases, indicating that the adopted motor is not completely suitable for signal injection sensorless control. Adequate compensation methods could improve the convergence region making it longer and more adherent to the MTPA reference.

In the following, the influence of the reference trajectory and rotor position on the convergence region are taken into account.

3.4 Dependency on the reference trajectory

Figure 3.6 shows the results of tests covering the influence of the reference trajectory. Four different linear references have been taken into account while the rotor position has been kept fixed at $\theta_{me} = 0$. The variation of the computed trajectories t_1 and t_2 for different current references (in terms of distance from the MTPA and lenght of curve t_2) is prominent. In particular, it can be noted that for $\theta_{REF} = 110°$ (Figure 3.6a) the operational limit of t_2 is 2 A. On the other hand, when the reference $\theta_{REF} = 170°$ is chosen, the sensorless operation is guaranteed for current amplitudes even greater than the nominal current (6 A), but this trajectory is not practically adopted. A good correspondence can be found between the computed t_1, t_2 and measured trajectories t'_1, t'_2. In Figure 3.6a, Figure 3.6b and Figure 3.6c, the measured trajectories t'_2 appear to be slightly wider than the computed t_2.

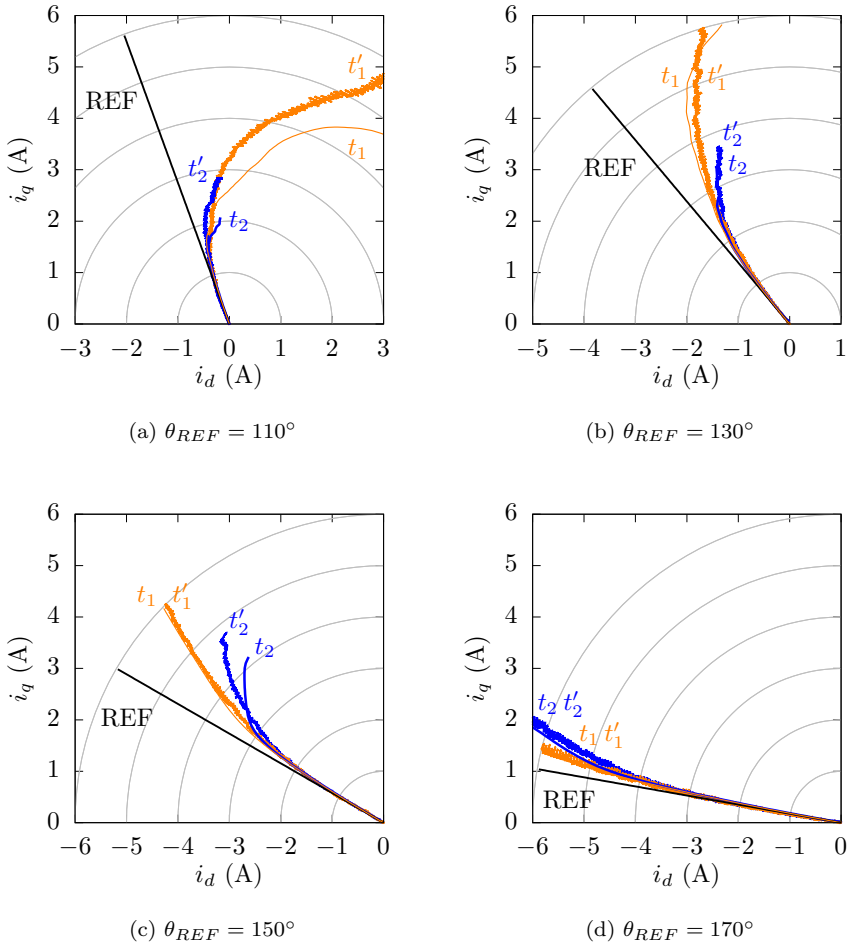

(a) $\theta_{REF} = 110°$

(b) $\theta_{REF} = 130°$

(c) $\theta_{REF} = 150°$

(d) $\theta_{REF} = 170°$

Figure 3.6: *Dependency on the reference trajectory.* Comparison between the trajectories computed on FEA data (t_1, t_2) and the trajectories recorded during the experimental tests (t_1', t_2'). The PMA-SynRM is locked at $\theta_{me} = 0°$. The reference trajectories are linear (θ_{REF} is constant).

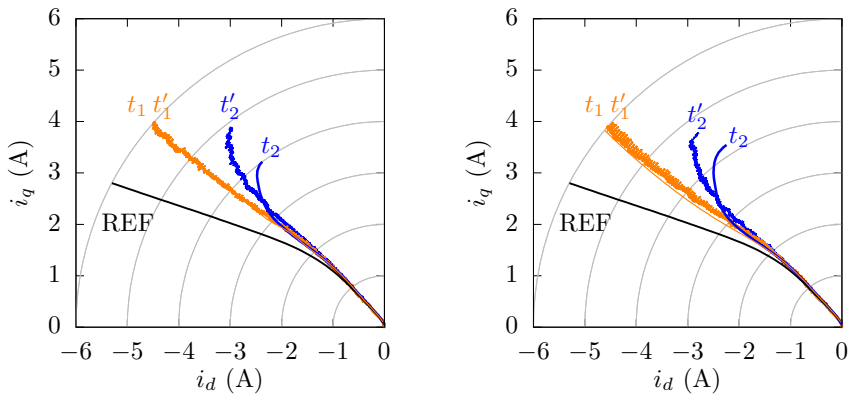

(a) $\theta_{me} = 0°$

(b) $\theta_{me} = 10°$

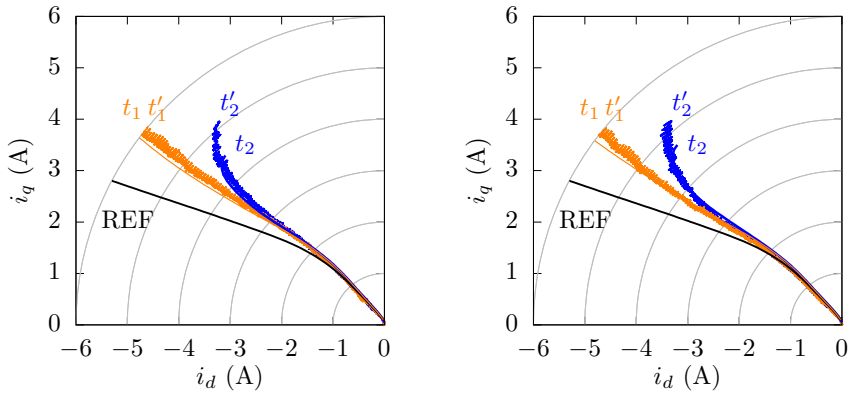

(c) $\theta_{me} = 20°$

(d) $\theta_{me} = 30°$

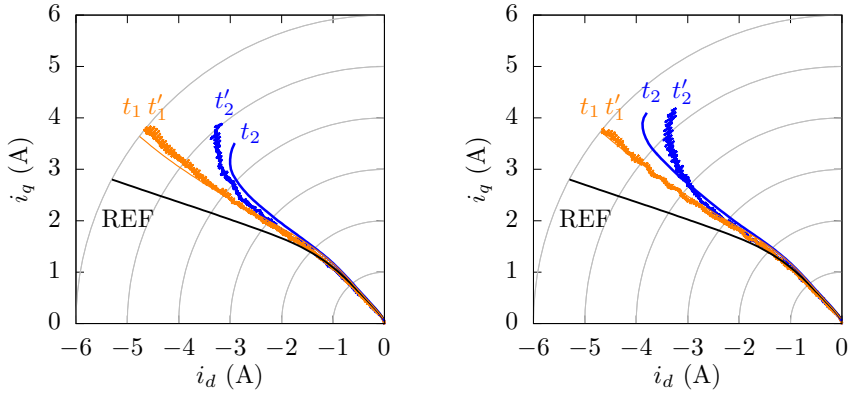

(e) $\theta_{me} = 40°$

(f) $\theta_{me} = 50°$

Figure 3.7: *Dependency on the rotor position.* Comparison between the trajectories computed on FEA data (t_1, t_2) and the trajectories recorded during the experimental tests (t_1', t_2'). The PMA-SynRM is locked at different rotor positions θ_{me}. The reference trajectory is the MTPA.

3.5 Dependency on the position

In the last group of tests (Figure 3.7) the effect of the rotor position is considered. The MTPA trajectory is adopted as current reference for both computations and measurements on PMA-SynRM. Six rotor positions have been considered. From the finite element simulations it appears that the theoretical operational limit of t_2 is between 4 A and 5.5 depending on the rotor position. In Figure 3.7 a good matching between sensored trajectories t_1 and t_1' can be found. Regarding the sensorless trajectories, the curves t_2' appear to be slightly longer than the computed t_2 in all the six figures except Figure 3.7f. The dependence on rotor position can be noticed in experimental tests (t_2'), but it is not as evident as in the computations (t_2).

3.6 Conclusions

In this chapter, an experimental investigation about the convergence region of a sensorless drive has been presented and adopted. The self-sensing capability of the drive has been described and highlighted by the difference between the sensored and the sensorless operation trajectories, t_1 and t_2 respectively. Both the trajectories can be evaluated online with proper measurements adopting a standard drive equipped with a position sensor. It has been demonstrated that the proposed measurement method allows to properly compute and evaluate the trajectories of the drive considering the effects of the current loop reference trajectory and the rotor position.

Chapter 4

Recursive Ellipse Fitting Algorhitm

Abstract - In this chapter a sensorless control scheme is proposed for low speed or standstill operation of a synchronous motor drive, characterized by a rotor anisotropy. The method is based on a high frequency voltage injection in the stator motor windings. High frequency current response to this injection is obtained from the measured currents thanks to a high pass filter. These filtered currents describe an ellipse trajectory, that is deeply analysed considering all its components. In particular, ellipse major semi-axis tilt is related to the rotor position. A recursive least squares estimator is proposed for the ellipse equation coefficients identification. After some manipulations, the rotor position is extrapolated from these information [19].

4.1 Introduction

In this chapter a new position estimation algorithm is proposed for low speed or standstill operation. The estimator is based on a high frequency rotating voltage vector injection. Unlike the solution described in [42, 49], the position is reconstructed every sampling period thanks to the identification of the current ellipse equation coefficients. These coefficients are recursively updated using a recursive least squares estimator (RLSE). Since the ellipse major semi-axis tilt depends on the rotor position, it can be easily computed by elaborating the ellipse equation coefficients. The proposed algorithm has the same known limits of the other injection-based sensorless techniques. Since the estimation is based on the motor anisotropy, rotor position cannot be extrapolated when the machine works in operating points where no anisotropy could be distinguished. Moreover, the presence of a strong correlation between the direct and quadrature axes, i.e. cross-saturation effect, introduces an error in the position estimation. Compensation techniques are beyond the scope of this work.

4.2 Ellipse detection method for the position estimation

4.2.1 High frequency rotating voltage injection

A standstill and low-speed rotor position estimator is proposed in this chapter for sensorless electric motor drives application. The method is based on the injection of a hf voltage signal that is superimposed to the voltage reference generated by the d-q axis current control loops. The rotor position can be extrapolated exploiting the current anisotropic responses to this injection, due to the rotor magnetic anisotropy. For this purpose the hf component of the currents is extracted by using a HPF, as shown in Figure 1.7.

A rotating voltage space vector in the α-β stationary reference frame of amplitude U_h and frequency $\omega_h = 2\pi f_h$ is used as injected signal. The permanent magnet flux linkage does not contribute to the hf voltage balance and the resistive drop can often be neglected due to the high frequency of the injected signal. According to these hypothesis, the motor equation assumes the following form:

$$\begin{bmatrix} u_{h\alpha} \\ u_{h\beta} \end{bmatrix} = \frac{d}{dt} \begin{bmatrix} \lambda_\alpha \\ \lambda_\beta \end{bmatrix} = \frac{\partial \boldsymbol{\lambda}_{\alpha\beta}}{\partial \mathbf{i}_{\alpha\beta}} \frac{d\mathbf{i}_{\alpha\beta}}{dt} = \begin{bmatrix} l_\alpha & l_{\alpha\beta} \\ l_{\alpha\beta} & l_\beta \end{bmatrix} \frac{d}{dt} \begin{bmatrix} i_{h\alpha} \\ i_{h\beta} \end{bmatrix} \tag{4.1}$$

As already explained in 1.6, in the case of anisotropic motor the current response to a rotating injection is a hf ellipse. The ellipse major-semi axis follows to rotor position. Thus, a real-time ellipse fitting technique can be used to extract the position information from the rotating ellipse (Figure 4.1).

4.2.2 A recursive ellipse parameters reconstruction

In this subsection the ellipse fitting technique is analysed. The problem of reconstructing ellipse equation parameters has already been faced [50]. Considering our case, ellipse parameters are time variant since the ellipse rotates at the electrical

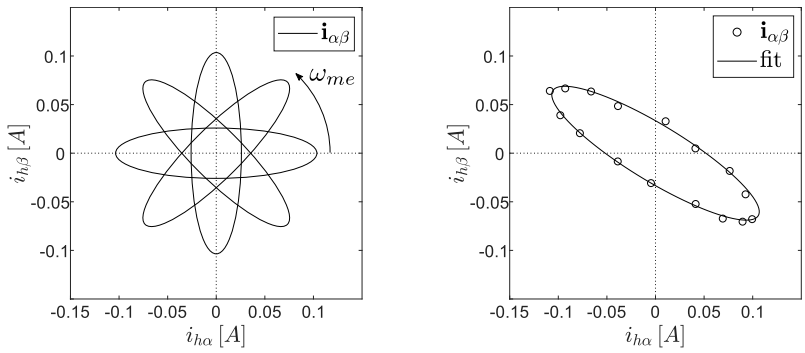

(a) Rotating ellipse (b) Current samples and fit

Figure 4.1: hf currents and ellipse fitting.

speed. However, since ellipse rotation is quite slow, the same happens for its equation coefficients. This is due to the operating speed range of the injection based sensorless algorithms, i.e. low speed and standstill.

Least squares estimator (LSE) is used to fit a set of current points with an ellipse, as shown in Figure 4.1b. This can be written in matrix form as:

$$\mathbf{H}\,\widetilde{\mathbf{x}} = \mathbf{y} \tag{4.2}$$

where:

$$\mathbf{H} = \begin{bmatrix} i_{\alpha 1}^2 & i_{\alpha 1} i_{\beta 1} & i_{\beta 1}^2 \\ i_{\alpha 2}^2 & i_{\alpha 2} i_{\beta 2} & i_{\beta 2}^2 \\ \vdots & \vdots & \vdots \\ i_{\alpha n}^2 & i_{\alpha n} i_{\beta n} & i_{\beta n}^2 \end{bmatrix} \quad \widetilde{\mathbf{x}} = \begin{bmatrix} a \\ b \\ c \end{bmatrix} \quad \mathbf{y} = \begin{bmatrix} -f \\ -f \\ \vdots \\ -f \end{bmatrix} \tag{4.3}$$

The $n \times 3$ matrix $\mathbf{H}$ is the measured data matrix, where the couples $(i_{\alpha 1}, i_{\beta 1})$, $(i_{\alpha 2}, i_{\beta 2}) \ldots (i_{\alpha n}, i_{\beta n})$ are the sampled hf filtered α-β current points. Each sampling period the matrix $\mathbf{H}$ is updated with a new couple of measured currents. The $n \times 1$ vector $\mathbf{y}$ can be imposed equal to the ones vector since f is a fixed scaling constant (1.25), related only to the hf injected voltage signal.

The coefficients a, b, c estimated with the LSE minimize the sum of the squares of the algebraic distances between the fitting ellipse and the data points. Coefficients vector $\widetilde{\mathbf{x}}$ can be evaluated as follows:

$$\widetilde{\mathbf{x}} = \left(\mathbf{H}^T\,\mathbf{H}\right)^{-1}\mathbf{H}^T\,\mathbf{y} \tag{4.4}$$

This solution requires a long buffer of n sampled points to guarantee a good fit, thus demanding high computational efforts. For this reason the LSE is not adopted and a recursive estimator [51] if preferred. In fact, under the hypothesis of low parameter changes, a recursive step by step ellipse identification appears more suitable:

$$\widetilde{\mathbf{x}}(k) = \widetilde{\mathbf{x}}(k-1) + \Delta\widetilde{\mathbf{x}}(k) \tag{4.5}$$

A proper recursive least squares estimator (RLSE) is implemented to estimate the ellipse equation coefficients. The RLSE can be performed exploiting less points than the LSE. Recursions are composed of three main steps:

- gain matrix $\mathbf{K}$ computation

$$\mathbf{K}(k) = \mathbf{P}(k-1)\,\mathbf{H}^T\,\left(\mathbf{H}\,\mathbf{P}(k-1)\,\mathbf{H}^T + \mathbf{R}\right)^{-1} \tag{4.6}$$

- covariance matrix $\mathbf{P}$ update

$$\mathbf{P}(k) = \frac{1}{\lambda}\,\left(\mathbf{P}(k-1) - \mathbf{K}(k)\,\mathbf{H}\,\mathbf{P}(k-1)\right) \tag{4.7}$$

- ellipse parameters vector $\widetilde{\mathbf{x}}$ update

$$\widetilde{\mathbf{x}}(k) = \widetilde{\mathbf{x}}(k-1) + \mathbf{K}(k)\,\left(\mathbf{y} - \mathbf{H}\,\widetilde{\mathbf{x}}(k-1)\right) \tag{4.8}$$

In the previous expressions, $\mathbf{R}$ is the measurement covariance matrix while λ is a forgetting factor. The fitting algorithm effectiveness is shown in the simulation and experimental tests in Sec. 4.3.

4.2.3 Rotor position reconstruction

The RLSE guarantees a recursive update of the parameters a, b, c. Neglecting cross-saturation effects, the position coincides to the ellipse major semi-axis tilt. Thus the rotor position estimation can be obtained from the parameters a, b, c by the following equation (in the case of PMA-SynRM):

$$\widetilde{\theta}_{me} = \frac{1}{2}\,\mathrm{atan2}(-b, c-a) \tag{4.9}$$

Eq. (4.9) generates a position signal $\widetilde{\theta}_{me}$ between 0 and π, as shown in Figure 1.10, because of the coefficient $\frac{1}{2}$. However for the machine control a position varying between 0 and 2π is necessary. The solution adopted in this work to maintain the estimated position in the desired interval is described hereafter. After an initial alignment, an incremental electric position is computed using the ellipse coefficients calculated during two following iterations:

$$\theta_k - \theta_{k-1} = \frac{1}{2}\,\arctan\left(\frac{-a_k\,b_{k-1} + b_k\,a_{k-1} - b_k\,c_{k-1} + c_k\,b_{k-1}}{a_k\,a_{k-1} - a_k\,c_{k-1} + b_k\,b_{k-1} - c_k\,a_{k-1} + c_k\,c_{k-1}}\right) \tag{4.10}$$

Coefficients subscripts indicate the sample time step. Keeping the position estimation in the desired interval results quite simple thanks to the incremental approach.

4.3 Simulation and experimental results

Several simulations have been performed to validate the proposed sensorless solution. Simulations are carried out on a PMA-SynRM motor whose parameters are reported in Table 2.1.

Sensorless control schemes performance is mainly influenced by l_{dq} and l_Δ, as already noticed in Sec. 4.2.1 and in Chapter 2. The PMA-SynRM motor is controlled on its MTPA trajectory (Figure 2.12a). The operating working point has to be quite far from the region where $l_\Delta = 0$ (Figure 2.9), that is the area where the convergence of the method is critical because of the loss of the rotor saliency containing the position information.

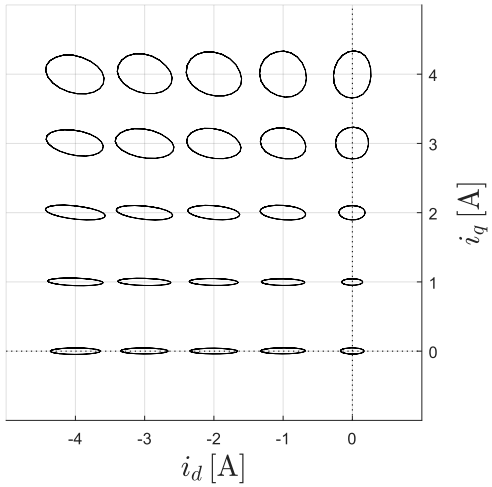

Figure 4.2: PMA-SynRM current ellipse shapes in different current operating points at standstill with $\theta_{me} = 0$ (simulations results).

Several simulations have been carried out to validate the relationship between equations (1.35) and (1.36) and the l_Δ map (Figure 2.9b). The rotor is kept in a fixed position ($\theta_{me} = 0$) and the hf rotating voltage signal is injected. Current responses are reported in Figure 4.2 for different operating points. A good correspondence is observed between the decrease of l_Δ and the reduction of the semi-axis ratio. The ellipse correspondent to the current point ($i_d = 0\text{A}, i_q = 4\text{A}$) is vertical because of an l_Δ sign change.

Experimental tests have been performed on the PMA-SynRM motor to further validate the proposed sensorless scheme. The test bench consists of a master permanent magnet (PM) synchronous motor and the PMA-SynRM under test, whose data has already been reported in Table 2.1. The proposed sensorless scheme (Figure 1.7) has been implemented thanks to a dSPACE 1104 Fast Control Prototyping Board. The board generates the six inverter reference voltages used to command the three-phase two-levels inverter that drives the PMA-SynRM.

During the test, the master assures the speed control (10 rpm), and different load torque are imposed through the PMA-SynRM motor in sensorless operation. Figure 4.3 shows the experimental results for different MTPA current points, and also the simulation error is reported. No error compensantion is adopted.

A good correspondence is observed between experimental and simulation results. The comparison between different operating points highlights that the higher is the current reference, the higher is the position estimation error. This result is consistent with the expected estimation error (Figure 2.14b). Increasing the current, in fact, the cross-saturation effect is stronger and the estimation error rises. The mean of experimental error is always negative because the considered MTPA current points are in the second quadrant of the d-q plane. During the 4 A test the 6^{th} spatial harmonics of the inductances appear in the experimental results.

For higher current points the convergence of the algorithm is guaranteed only adopting an error compensation technique.

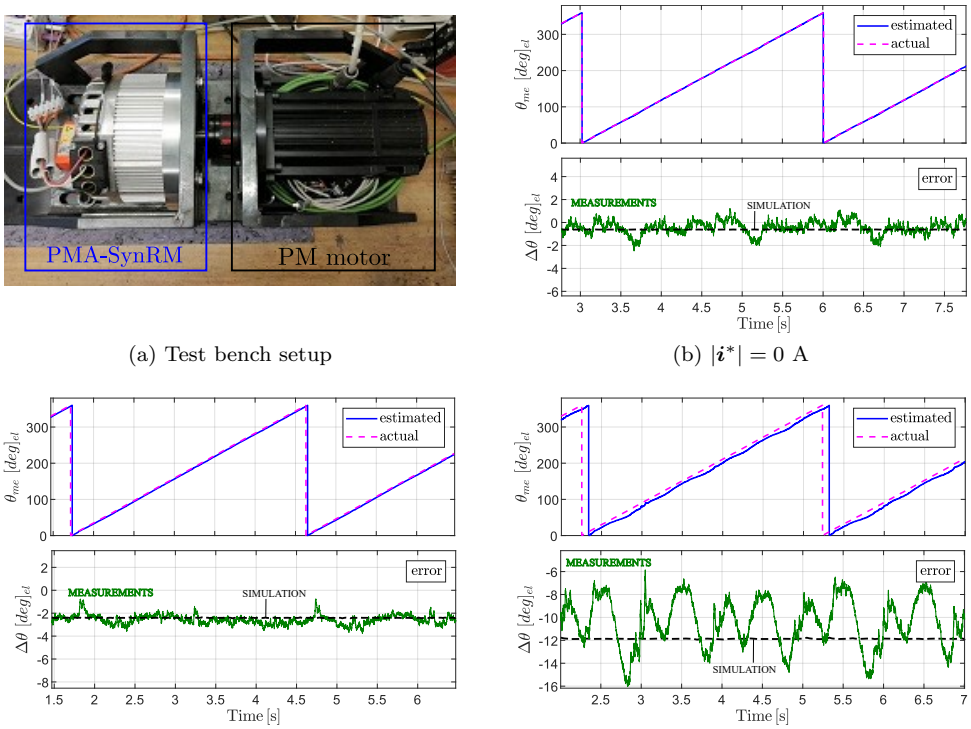

(a) Test bench setup

(b) $|\boldsymbol{i}^*| = 0$ A

(c) $|\boldsymbol{i}^*| = 2$ A

(d) $|\boldsymbol{i}^*| = 4$ A

Figure 4.3: Position estimation and related estimation error during a 10 rpm operation: experimental (and simulation) results.

4.4 Conclusions

This chapter presents a method for the sensorless control of synchronous motors at low speed or standstill. The technique employs a high frequency rotating voltage vector injection, thus it is valid for anisotropic machines such as synchronous reluctance and interior permanent magnet motors. Unlike other solutions, the proposed algorithm does not require a heterodyning demodulation of the current response. The position information is extracted from the sampled high frequency currents by a recursive ellipse coefficients identification algorithm. Simulations and experimental tests are presented for validating the method effectiveness.

Chapter 5

Recursive QR Ellipse Fitting Algorhitm

Abstract - In the conventional signal-injection control schemes, the rotor position estimation is achieved through the demodulation of the high frequency current response. In this chapter, an efficient ellipse fitting procedure is presented for detecting rotor position from the rotating high frequency injection current response. The inverse problem related to the ellipse fitting is solved implementing a QR recursive least squares algorithm. Efficient updating QR factorization has been adopted because of its features in terms of numerical stability and required limited computational effort. The proposed sensorless control scheme is validated by means of many experiments [20].

5.1 Introduction

This chapter deals with a sensorless synchronous motor drive based on high frequency sinusoidal voltage injection suitable for standstill and low speed applications. At every control sample, rotor position and speed are reconstructed by a recursive update using a least squares (RLS) estimator algorithm. Compared to most of its competitors, the RLS exhibits extremely fast convergence. However, this benefit comes at the cost of higher computational complexity. The ellipse fitting of the current response locus to rotating high frequency voltage injection has already been faced in [19].
An efficient QR updating factorization is implemented in this chapter. In linear algebra, a QR decomposition, also known as a QR factorization or QU factorization is a decomposition of a matrix A into a product $A = QR$ of an orthogonal matrix Q and an upper triangular matrix R. QR decomposition is often used to solve the linear least squares problem and is the basis for a particular eigenvalue algorithm, the QR algorithm. In this work, Givens rotations [52, 53] are implemented in order to reduce the computational effort drawback of the factorization, and achieving performance which makes the proposed algorithm mature even for industrial embedded applications.

Moreover, a comparison is done with the conventional demodulation scheme [1] which shares the same rotating injection in the stationary reference frame.

The work is organized as follows: firstly the mathematical model and the overall control scheme is derived in Sec. 5.2; the recursive least squares algorithm and the QR updating factorization are stated in Sec. 5.3; then many experimental results are shown and commented in Sec. 5.4 to fully validate the proposed approach.

5.2 Mathematical model

The proposed sensorless scheme operates in the stator reference frame. A voltage vector $u_{h\alpha\beta}$(t) rotating at high frequency, $\omega_h = 2\pi\,1000$ rad/s, is injected in the stator windings.

$$u_{h\alpha\beta}(t) = \begin{bmatrix} u_{h\alpha}(t) \\ u_{h\beta}(t) \end{bmatrix} = \begin{bmatrix} U_h \cos(\omega_h t) \\ U_h \sin(\omega_h t) \end{bmatrix} \tag{5.1}$$

Thus, a corresponding high frequency current response, $i_{h\alpha\beta}$(t), arises:

$$i_{h\alpha\beta}(t) = \begin{bmatrix} i_{h\alpha}(t) \\ i_{h\beta}(t) \end{bmatrix} \tag{5.2}$$

An implicit equation for the ellipse centered in zero described by $i_{h\alpha\beta}(t)$ is given by:

$$a\; i_{h\alpha}^2(t) + b\; i_{h\alpha}(t) i_{h\beta}(t) + c\; i_{h\beta}^2(t) + f = 0 \tag{5.3}$$

where:

$$f = -\frac{U_h^2}{\omega_h^2} \tag{5.4}$$

Measuring $i_{\alpha\beta}$ and filtering its high frequency component $i_{h\alpha\beta}$, knowing the injected

hf voltage magnitude U_h and frequency ω_h, it is possible to solve an inverse problem in order to estimate the coefficients a, b, c describing the ellipse in (5.3). An inverse problem, in science, is the process of calculating from a set of observations the causal factors that produced them. Inverse problems are some of the most important mathematical problems in science and mathematics because they tell us about parameters that we cannot directly observe. In the considered case study, the rotor electrical position and speed information are intrinsic in the ellipse.

To compute a, b, c coefficients from the current measures, an inverse problem has to be solved. The unknown coefficients vector is defined as $x = [a, b, c]^T \in \mathbb{R}^3$, thus at least three measurements $i_{h\alpha\beta}$, sampled in three consecutive control time instants, are necessary. Since measurements can be affected by noise, it is better to consider the overdetermined system stated in (5.5).

$$Ax = b \tag{5.5}$$

where

$$A = \begin{bmatrix} i_{h\alpha 1}^2 & i_{h\alpha 1} i_{h\beta 1} & i_{h\beta 1}^2 \\ i_{h\alpha 2}^2 & i_{h\alpha 2} i_{h\beta 2} & i_{h\beta 2}^2 \\ \vdots & \vdots & \vdots \\ i_{h\alpha m}^2 & i_{h\alpha m} i_{h\beta m} & i_{h\beta m}^2 \end{bmatrix} \quad x = \begin{bmatrix} a \\ b \\ c \end{bmatrix} \quad b = \begin{bmatrix} -f \\ -f \\ \vdots \\ -f \end{bmatrix} \tag{5.6}$$

Once the coefficients a, b, c have been computed, the rotor position and speed can be used to properly control the drive. In the following, an efficient algorithm to solve this inverse problem is presented.

5.3 QR Recursive Least Squares

5.3.1 Linear Least Squares

The method of least squares (LS) is a standard approach in regression analysis to approximate the solution of overdetermined systems. In particular, the linear LS problem can be defined as the following optimization problem as a function of $x \in \mathbb{R}^n$, where $A \in \mathbb{R}^{m \times n}$, $b \in \mathbb{R}^m$ and $m > n$.

$$\min_x ||Ax - b||_2^2 \tag{5.7}$$

For small and medium size linear LS problems with full-rank matrix A, there are three main well-known methods to compute the solution x: 1) solving the associated normal equations system of (5.7) with direct methods such as Cholesky factorization (CF); 2) using the QR factorization of A; or 3) computing the singular value decomposition (SVD) of A. The system of normal equations is obtained by setting the gradient of (5.7) equal to zero.

$$\begin{aligned} \min_x J(x) &= \min_x ||Ax - b||_2^2 = \min_x (Ax - b)^T (Ax - b) \\ &= \min_x x^T A^T A x - 2x^T A^T b + b^T b; \\ \nabla J(x) &= 2A^T A x - 2A^T b = 0; \\ &\Rightarrow \qquad A^T A x = A^T b. \end{aligned} \tag{5.8}$$

1) Since in the case study of this work the Hessian $2A^TA$ is real, positive definite and symmetric, so that the Cholesky factorization can be a suitable solution regarding the computational effort it requires to be implemented in embedded hardware.

2) The full-rank assumption of A guarantees the existence of its QR factorization $A = QR$, where Q is orthonormal and R is upper triangular. Hence, substituting in (5.8) and using the orthogonality of Q, one has

$$\begin{aligned} R^TQ^TQRx &= R^TQ^Tb \\ R^TRx &= R^TQ^Tb \\ Rx &= Q^Tb. \end{aligned} \tag{5.9}$$

Since R is upper triangular, the last system can be backward solved with minimal computational effort. However, the QR factorization of A requires a higher computational effort than the CF, mostly if Givens rotations are used to obtain the orthogonal triangularization of R. As an advantage over other techniques to build the factorization of QR, Givens rotations guarantee stability if a backward error analysis is studied. This is an important property for embedded applications, where limited machine precision can badly affect the solution accuracy.

3) Using SVD for solving (5.7) is in general suggested when A is severely ill-conditioned or even singular, because it allows to find anyway the minimum norm solution. As a drawback, this approach requires the highest computational effort if compared with the two previous methods, hence it is not in general suitable for embedded applications using hardware with limited computational power, which is a hard constrain for SVD implementation.

The target of this work is industrial applications, where hardware with limited computational power, memory and single machine precision is in general adopted. Thus, the QR factorization has been chosen as good compromise in terms of computational effort and reliability in the solution quality when the problem is ill-conditioned. A possible situation of ill-conditioned problem, related with the considered application, can occur when the hf injection is too slow respect to the sampling measurement time. In the just described condition, the new data can be very similar with the old data, hence A can result ill-conditioned.

5.3.2 Recursive QR Factorization

In Sec. 5.2 the estimation issue has been presented, where an on-line parameter identification problem has been stated. Because of its properties, a recursive least squares algorithm is implemented to identify the coefficients describing the ellipse which best fits measured currents in the $\alpha\beta$ stationary reference frame. In this kind of application it is necessary to re-factor a given matrix A after it has been altered by appending a row to it. Hereon it is shown that in situations like this, it is much more efficient to update A's QR factorization than to generate it from scratch. Furthermore, before beginning, it is worth mentioning that there are also techniques for updating different factorizations, like CF and SVD. However, updating these factorizations can be quite delicate because of pivoting requirements and because when a positive definite matrix is tampered using these techniques, the result may not be positive definite. Moreover, regarding the updating SVD factorization, it is based on an iterative method, thus it is more computational expensive than CF and QR. Mostly, the convergence it is not always guaranteed, specially if just few iterates are considered in order to achieve the real-time feasibility of the method.

In a generic control instant k, it is supposed the knowledge of the factorization $Q_{k-1}\,R_{k-1} = A_{k-1} \in \mathbb{R}^{m\times n}$. The objective is to compute the updated factorization since new data measurements $w_k \in \mathbb{R}^n$ are available. The matrix A_k can be written as:

$$A_k = \begin{bmatrix} \lambda A_{k-1} \\ w_k \end{bmatrix} = \begin{bmatrix} Q_{k-1} & 0 \\ 0 & 1 \end{bmatrix} \begin{bmatrix} \lambda R_{k-1} \\ w_k \end{bmatrix} \tag{5.10}$$

defining

$$Q^* = \begin{bmatrix} Q_{k-1} & 0 \\ 0 & 1 \end{bmatrix} \qquad R^* = \begin{bmatrix} \lambda R_{k-1} \\ w_k \end{bmatrix} \tag{5.11}$$

It is worth mentioning that λ is the so-called forgetting factor, which gives exponentially less weight to older measurements. It can be observed that matrix R^* is upper triangular except for the last row. Thus, n orthogonal transformations have to be applied for setting to zero the last row of R^*. In particular, Givens rotations are suitable for this purpose, since they are orthogonal transformations which selectively set to zero singly individual elements. These are rank-two corrections to the identity of the form

$$G_{i,j} = \begin{bmatrix} I & & & & \\ & cos(\theta) & & sin(\theta) & \\ & & I & & \\ & -sin(\theta) & & cos(\theta) & \\ & & & & I \end{bmatrix} \tag{5.12}$$

$G_{i,j}^T$ is also clearly orthogonal. Furthermore, premultiplication by $G_{i,j}^T$ amounts to a counterclockwise rotation of θ radians in the (i, j) coordinates plane. For a generic vector $z \in \mathbb{R}^n$, if one defines

$$cos(\theta) = \frac{z_i}{\sqrt{z_i^2 + z_j^2}}, \qquad sin(\theta) = \frac{-z_j}{\sqrt{z_i^2 + z_j^2}}, \tag{5.13}$$

Then for $G_{i,j}^T z = y$ one obtains

$$y_k = \begin{cases} cos(\theta)z_i - sin(\theta)z_j & k = i \\ 0 & k = j \\ z_k & k \neq i, j \end{cases} \tag{5.14}$$

therefore only elements i, j are affected. The same result can be achieved if R^* is premultiplied by $G_{i,j}^T$, with the difference that just rows i and j will be modified, while the element $R^*(i, j)$ will be zero. Thus, to find $Q_k R_k = A_k$, n Givens matrix transformations $G_{i,j} \in \mathbb{R}^{m+1\times m+1}$ have to be defined to eliminate w_k componentwise to give

$$G_{n,m+1}^T G_{n-1,m+1}^T ... G_{1,m+1}^T R^* = R_k \tag{5.15}$$

so, finally,

$$A_k = Q^* R^* = Q^* G_{1,m+1} G_{2,m+1} ... G_{n,m+1} R_k = Q_k R_k \tag{5.16}$$

Once the updating of the QR factorization is obtained, the solution of the RLS problem at the control sample instant k is then found by backward solving the system (5.17), where the last row of R_k and Q_k can be deleted since one has been

set to zero and the other holds to the $ker(Q)$ respectively. In this way, system (5.17) has always 3×3 dimension, since the unknown coefficients vector is defined as $x = [a, b, c]^T \in \mathbb{R}^3$.

$$R_k x_k = Q_k^T b_k \tag{5.17}$$

It is worth to remark that the QR updating factorization is the best solution for this kind of application, since it guarantees all the previously mentioned numerical features and it is the most efficient algorithm in terms of computational effort.

The unique drawback, which has to be faced, is the first complete QR factorization required for starting the updating algorithm. In the considered work, the complete QR factorization using Givens rotations has been implemented since the dimension of A is small. However, because of limited DSP computational power, in the control instant where the complete QR factorization of A is required, some control tasks are not run in order to avoid overrun situations. In particular, the estimation of x, by solving (5.9), and then all the algebraic manipulations necessary to calculate the estimated rotor position are not run till the complete QR factorization is computed. Thus, for the firsts control instants, the estimated rotor position is set to zero, dealing with an open loop control just for the initial instants.

5.4 Experiments

5.4.1 Setup Description

The proposed sensorless drive control strategy has been implemented in two different control platforms. At first a dSPACE 1104 rapid prototyping system has been adopted. The software has been developed using MATLAB-Simulink package in order to test the estimation performances of the proposed method under different operating conditions. Then, to validate the industrial application maturity, an efficient C code has been implemented on an industrial micro-controller (RX23T) running at 40 MHz with a single precision floating-point operation unit. The turn around time (tat) of RLS, including the updating of the QR factorization, is shown for both control platforms in Table 5.1, confirming the maturity of the algorithm for industrial embedded applications.

Regarding the motor under test, it is a PMA-SynRM prototype [34] connected to an industrial three-phase inverter. The BUS DV voltage is 300 V, and the adopted control frequency is 10 kHz. Main data of the considered motor are shown in Table 2.1. PMA-SynRM under test is mechanically connected to another PMSM, here on called "master motor", as shown in Figure 5.2a. This configuration allows to control the PMA-SynRM through the current loops, when the master holds the speed, and the speed loop, when the master applies a certain torque load.

Figure 1.7 presents the current control scheme. As it can be observed, once the phase currents are measured, they are filtered with a high pass filter (HPF) for letting the QR-RLS algorithm processing the high frequency component $i_{h\alpha\beta}$, while a low pass filter (LPF) is adopted to cut off the high frequency component from the proportional integral (PI) current control loops. The adopted HPF and LPF are digital first-order Infinite Impulse Response (IIR) filters. The continuous-time transfer functions of high-pass and low-pass filters are defined as:

$$H(s)_{\,\mathrm{HPF}} = \frac{\tau s}{\tau s + 1} \qquad H(s)_{\,\mathrm{LPF}} = \frac{1}{\tau s + 1} \tag{5.18}$$

Table 5.1: QR-RLS routine turn around time on the two considered hardware.

	CPU	**tat RLS**
DS1104	250 MHz	10 μs
RX23T	40 MHz	20 μs

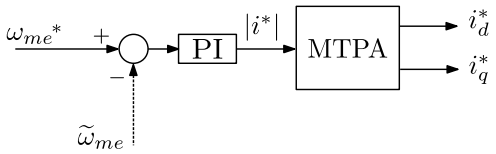

Figure 5.1: Sensorless speed control scheme.

where the filter time constant τ is equal to the reciprocal of the cutoff frequency $\omega_c = 2\pi f_c$. In the presented application, characterized by an injection frequency equal to $f_h = 1000$ Hz, the cutoff frequency has been set to $f_c = 500$ Hz for both HPF and LPF filters. For the implementation in the control algorithm, the transfer functions in the Z-domain have been obtained through the forward Euler discretization of (5.18). The computational time of each digital filter is just under 1 μs in the dSPACE 1104 platform.

The speed control loop is represented in Figure 5.1. It has been designed with a PI controller coupled with a linear MTPA trajectory for translating the PI output $|i^*|$ into the current references i_d^*, i_q^*. The estimated speed feedback is indicated with $\widetilde{\omega}_{me}$.

5.4.2 Results

The proposed sensorless control drive is validated by means of experiments. At first, the current control performance and the rotor position estimation accuracy are shown, imposing different speeds with the master motor and changing the *d-q* currents references. Secondly, the speed control performance is evaluated, using the master motor as load.

Current Control

Sensorless steady-state current control results are shown in Figure 5.3, 5.4, 5.5, 5.6. The first test is done at no load holding a speed of 10 rpm with the master motor. A forgetting factor $\lambda = 0.98$ is used. In the first plot of Figure 5.3 the estimated position $\widetilde{\theta}_{me}$ (obtained from the QR-RLS) and the actual position θ_{me} (measured with an encoder) are shown. Also the position error is illustrated. The mean value of the the position error is zero. However, its profile is not constant. This happens because the incremental inductances l_Δ and l_{dq}, supposed constant in Sec. 5.2, change with the current working point but also with the actual rotor position [16,54]. The resultant position fluctuation, depending on the motor incremental inductances, is between -3 and 3 electrical degrees in this current working point ($i_d, i_q = 0$; only the hf voltage is applied).

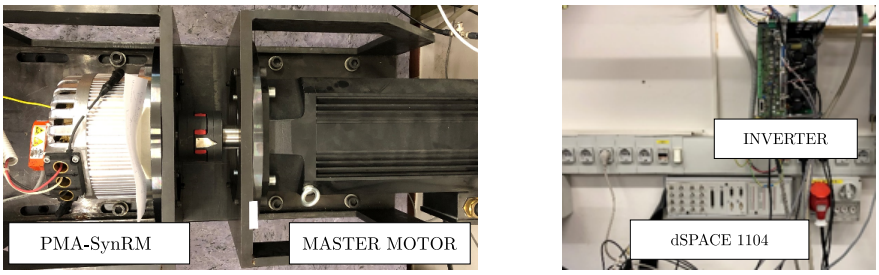

(a) Test bench. (b) Inverter and controller.

Figure 5.2: Experimental setup.

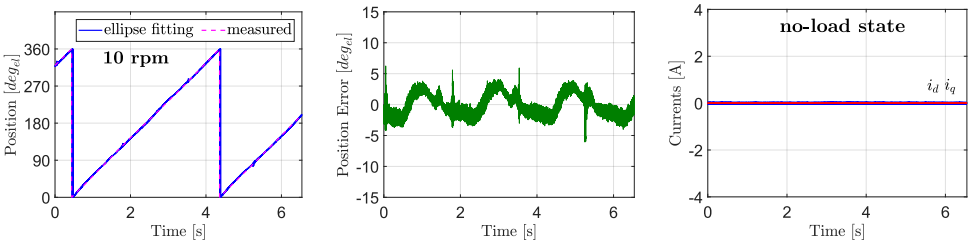

Figure 5.3: Sensorless current control results with $|i^*| = 0$ A, $n = 10$ rpm, $\lambda = 0.98$

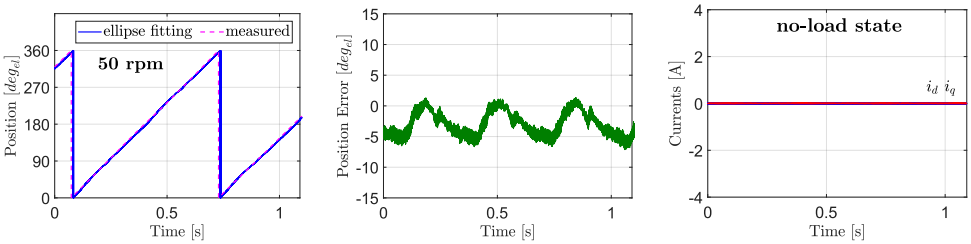

Figure 5.4: Sensorless current control results with $|i^*| = 0$ A, $n = 50$ rpm, $\lambda = 0.97$

Figure 5.4 shows a no load test at 50 rpm. Comparing the results with the 10 rpm test, an offset appears in the position error. This issue can be explained considering the fitting procedure (5.6). The current points $i_{h\alpha\beta}$ are buffered in matrix A, which is recursively factorized in QR form. Sampling a rotating ellipse implies that the older measurements are unreliable, especially if the ellipse rotates at high speed, because the points sampled first are not updated with the actual rotor position. Decreasing the forgetting factor it is possible to give less weight to older measurements. In this way the offset error in the estimated position can be reduced or completely eliminated. However, values of λ less than 0.95 are not suggested because they increase the variance error (the noise in the estimated position). A compromise between bias and variance estimation error must be found at the different operating speeds. For example, $\lambda = 0.97$ has been chosen at $n = 50$ rpm.
In Figure 5.5 and Figure 5.6 the steady-state tests, at 10 and 50 rpm, have been

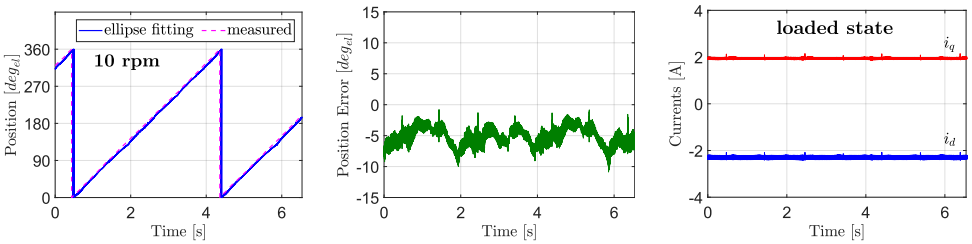

Figure 5.5: Sensorless current control results with $|i^*| = 3$ A, $n = 10$ rpm, $\lambda = 0.98$

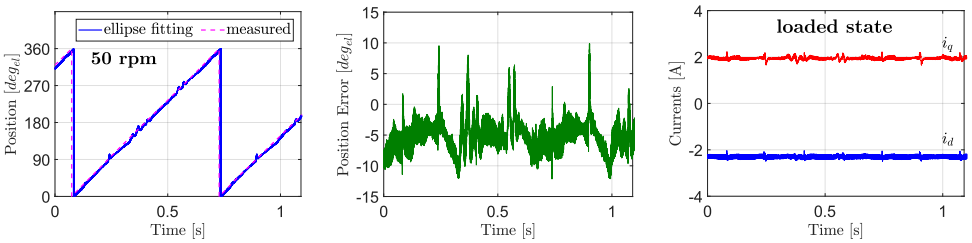

Figure 5.6: Sensorless current control results with $|i^*| = 3$ A, $n = 50$ rpm, $\lambda = 0.965$

repeated with a MTPA current reference of 3 A. Considering the 10 rpm tests, the mean value of the error is 0° at no load, and −5° at 3 A (Figure 5.3, Figure 5.5), which is still acceptable by the controller. Because speed n and forgetting $\lambda = 0.98$ are the same in the two tests, the increase of the estimation error can be attributed to the cross-saturation effect [24,55]. In fact the cross-saturation inductance l_{dq} affects the position estimation introducing a bias error. The value of l_{dq} increases with the current amplitude. As concerns the 50 rpm test, choosing $\lambda = 0.965$ reduces the bias error but increases the variance error, as can be noticed in (Figure 5.6). However, the controller shows stability and a higher forgetting factor could filter the estimation as analysed in Sec. 5.4.2.
A MTPA current step from 0 to 3 A has been performed. Figure 5.7, 5.8 show the results at 10 and 50 rpm. As expected, in both cases the bias error increases after the current step because of the cross-saturation effect. The steady-state errors are coherent with the ones obtained in Figure 5.3,. The proposed algorithm shows good stability in dynamic current control operating condition. The latter means that the estimator is fast enough to not corrupt PI controllers; in fact PI bandwidth has not been changed passing from sensored to sensorless current control.
Resuming the obtained results for the proposed sensorless current control, it has been tested in different speeds and currents both in steady-state and dynamic conditions, showing promising performance in terms of estimation accuracy and control stability. As a drawback, it has been demonstrated that the estimation accuracy shows speed and currents dependency. The speed dependency can be avoided adopting a look-up table (LUT) with different forgetting factors. Regarding the current dependency, which is a known limit of hf voltage injection techniques, valid solutions, as proposed in [16, 54], suggest an error compensation method based on the current operating point.

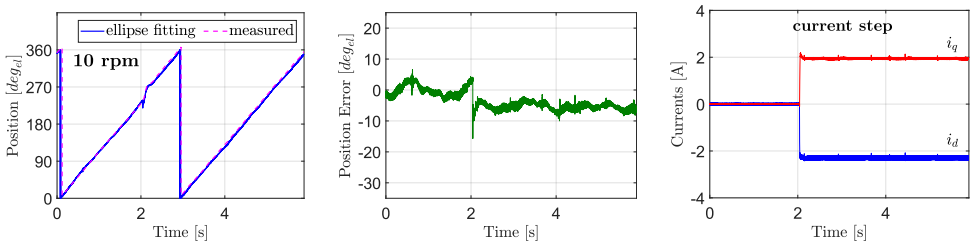

Figure 5.7: Sensorless current control results with 3 A MTPA current reference step, $n = 10$ rpm, $\lambda = 0.98$

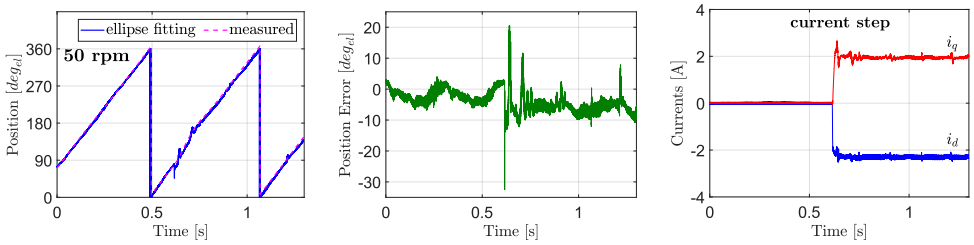

Figure 5.8: Sensorless current control results with 3 A MTPA current reference step, $n = 50$ rpm, $\lambda = 0.965$

Speed Control

Speed estimation is necessary if a speed control operation is required. The proposed algorithm deals with equation (1.31) discretized using forward Euler method. PI speed control loop feedback has been closed using (1.31) filtered with a LPF. Figure 5.9 shows a rise speed step from 0 to 100 rpm. Error percentage between the estimated and measured speed is shown. It can be noticed that in steady-state condition the error is always smaller than 10%, which is a good result considering that 100 rpm is a high rate for hf voltage injection technique applied to the considered PMA-SynRM. It is worth mentioning that a constant forgetting factor equal to 0.96 has been implemented for this experiment, showing a wide operating range without the needed of LUT. Furthermore, even in this case, the PI bandwidth has not been changed passing from sensored to sensorless speed control.

Important Considerations

It is important to highlight that the novelty of this work is the adopted method used for solving the RLS problem applied to sensorless synchronous motor drive application. The efficient implementation of updating QR factorization allows to achieve the minimum computational effort with good reliability in the solution goodness when the problem is ill-conditioned. Last feature is significant when the adopted hardware has single precision floating-point operation unit, thus if matrix A is ill-

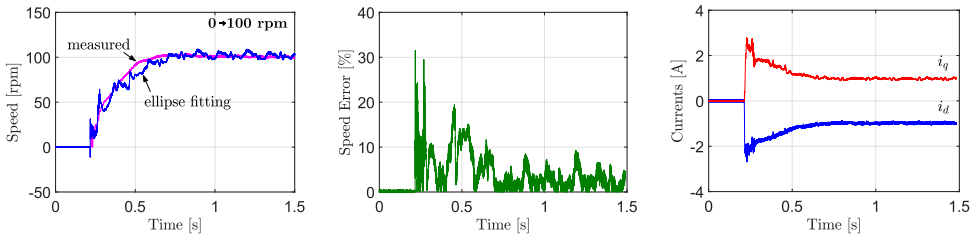

Figure 5.9: Sensorless speed control results with 100 rpm speed reference step.

conditioned, the Hessian $2A^TA$ is even more ill-conditioned and the solution quality could be poor if Cholesky factorization has implemented. Instead, using the QR factorization, (5.9) has to be solved and R holds the same condition number of A.

Comparison with conventional demodulation method

In the conventional hf injection methods, the rotor position estimation is achieved through the demodulation of the high frequency current response. In this subsection, a comparison of the latter with the proposed algorithm is investigated, highlighting different aspects as well as showing off pros and cons of the two techniques. The adopted demodulation technique in shown in Figure 1.5 [9]. Experiments done in Figure 5.7, 5.8 and Figure 5.9 are repeated using the sensor measurements. In this way the two techniques can work with the same transfer function system in the control so that a meaning comparison is obtained.

Figure 5.10 and Figure 5.11 show the current control comparison performance at 10 and 50 rpm. As it can be noticed in both experiments, the ellipse fitting techniques presents a smaller estimation error (Figure 5.10b and Figure 5.11b) and faster response in tracking the rotor position when the current reference changes at time 0.4 s (Figure 5.10a and Figure 5.11a). Indeed, the proposed algorithm is less affected by signal processing delay effects. In particular, these latter are a well known issue for the demodulation technique [56] and they request particular further details to be avoided [57], increasing the computational effort.

Figure 5.12 shows the speed control comparison results with 100 rpm reference step at low load condition, where speed estimation is necessary for the control purpose. Even in this case, the ellipse fitting technique exhibit a faster response in tracking the speed when a change event occurs, while in steady state condition the two schemes have comparable performance, regarding the speed estimation.

To measure the difficulty of solving a computational problem, one may wish to see how much time the algorithm requires to solve the problem. Thus, for the sake of completeness, in Table 5.2 there are shown the turn around times of both the compared techniques. As it can be observed, the two techniques are comparable in the sense that they have the same order of magnitude. It should be noted that the considered demodulation scheme does not include the compensation strategy for the signal processing delays.

Summarizing pros and cons highlighted in this subsection:

- the ellipse fitting is less sensitive to offset errors due to digital implementation;
- the ellipse fitting requires a smaller tuning effort than demodulation technique

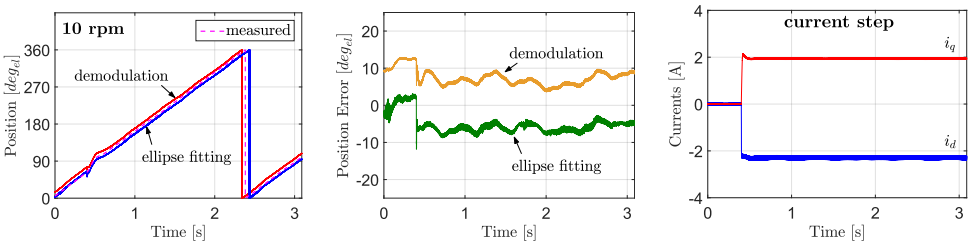

Figure 5.10: Comparison current control results with 3 A MTPA current reference step at 10 rpm. Experimental results.

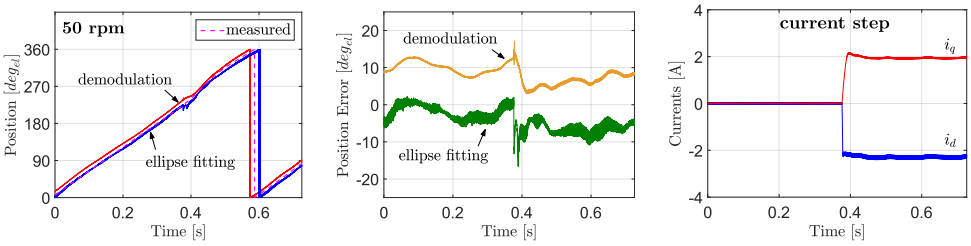

Figure 5.11: Comparison current control results with 3 A MTPA current reference step at 50 rpm. Experimental results.

(just λ has to be tuned), since less filters and PIs are present in the control scheme;

- the ellipse fitting is more expensive regarding the computational effort, but using the proposed updating QR factorization, it appears, from the turn around time comparison, that it has been achieved feasible real-time implementation for embedded industrial controller.

Forgetting Factor Tuning

In this subsection it is given a further analysis about the tuning of λ. As previously mentioned, the forgetting factor gives exponentially less weight to older measurements. For example, to better understand, taking $\lambda = 1$ it is like calculating the average value of all the measurements taken into account from the beginning, when the algorithm started. Based on this concept, the forgetting factor tuning has been done manually, finding which are the values that better allow the ellipse fitting in function of the speed. In other words, since the ellipse is rotating, old measurements belonged to another ellipse respect to the current one, thus the weight (memory) of these measurements has to be reduced (forgotten) in the optimal problem. This is the reason why in Figure 5.9 a forgetting factor $\lambda = 0.98$ has been chosen at $n = 10$ rpm, while $\lambda = 0.965$ has been selected at $n = 50$ rpm.

For the sake of completeness, in the following references [58], [59] there are shown other techniques for the forgetting factor decision. In our case, forgetting factor has been chosen after a preliminary simulation analysis, done offline with measured currents.

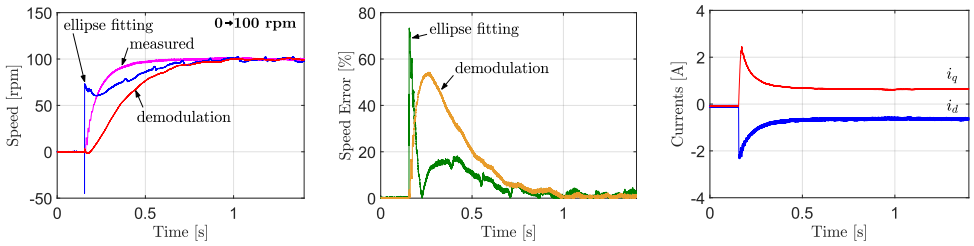

Figure 5.12: Comparison speed control results with 100 rpm reference step at low load condition. Experimental results.

Table 5.2: Turn around time comparison.

	Ellipse Fitting	**Demodulation**
dSPACE1104	10 μs	3 μs
RX23T	20 μs	7 μs

5.5 Conclusions

This work deals with sensorless drive with hf injection technique. In particular, an efficient QR updating factorization for solving the inverse problem related to the rotor position measurement has been presented. It allows to estimate the rotor position and speed processing efficiently the hf current response. It has been demonstrated that it is a valid solution thanks to its features in terms of numerical stability and required computational effort. It is based on a recursive least square algorithm and the proposed overall control strategy has been validated by means of many experiments, testing both speed and current sensorless control drives, achieving promising results. Moreover, the algorithm has been successfully implemented on two different control platforms. Turn around time analysis has been performed, showing implementation feasibility even for hardware with limited memory and computational power. This confirms the maturity of the proposed method for industrial embedded application such as electric drives.

Chapter 6

Incremental Inductances Estimation

Abstract - This chapter deals with the online incremental inductances estimation of a synchronous motor at low speeds using a high-frequency voltage injection. The control scheme is analogous to that used in position estimation algorithms, with the difference that the current control and the rotating voltage injection operate on the real dq axes. Thus a position sensor is required to apply this method. The corresponding current response is measured, filtered, and processed with an ellipse fitting technique. The estimated ellipse coefficients are then used to retrieve the incremental inductances online without the need of any post processing. A novel formulation to express the estimation error valid for other conventional signal injection techniques is presented. The method has been validated experimetally on a SynRM at locked rotor and during load and speed transients [60].

6.1 Introduction

Permanent magnet synchronous motors are widely adopted in variable speed drives for industrial applications due to their high torque density, dynamic performance, and efficiency. It is well known that SynRM, PMA-SynRM and IPMSM are usually characterized by nonlinear flux linkages maps [21]. As a consequence of that, the knowledge of an accurate model of the motor is necessary to design a high-performance current controller [61, 62]. Several parameter identification and self-commissioning methods for AC motor drives have been proposed in literature [35, 63], based on finite element simulations and laboratory measurements.

The focus of this work is on the identification methods based on hf voltage injection. In particular, an online incremental (differential) inductance estimation technique is proposed. The method is applicable to motors characterized by rotor saliency, i.e. SynRM, PMA-SynRM and IPMSM.

Ebersberger and Piepenbreier proposed a differential inductance and stator resistance identification method using test current instead of voltage injection [64]. A proportional-resonant controller located in parallel to each fundamental PI-type current controller in dq coordinates imposes a hf current injection. The hf-portions of the respective signals are separated online by means of the Goertzel algorithm and used to determine the differential self and mutual inductances. The main drawback of the method is that the test current signal injection cannot be executed simultaneously on both d and q axes. When the current signal is injected into the d-axis, the inductances l_{dd} and l_{qd} can be estimated. When the current signal is injected into the q-axis, the inductances l_{dq} and l_{qq} can be estimated. Another limit of the method is that its validity has been proved only at standstill (locked rotor).

Kuehl and Kennel proposed a method to estimate the differential inductances using a conventional pulsating voltage injection in dq superimposed to a sensored control scheme [65]. The differential inductance matrix is obtained measuring both the eigenvalues of the uncoupled inductance matrix and the estimation error ε from the sensorless algorithm. Similarly to [64] two separate measurements are necessary: one, where the sensorless algorithm tracks the estimated d-axis, and one for the q-axis. A post-processing least-squares optimization problem has to be solved to find the optimal correction variables. The method has been validated on an IPMSM coupled to a load motor, which was controlled at a fixed speed by an industrial inverter.

The identification method presented in this work tries to extend the works in [64] and [65]. First of all, a rotating injection in dq allows to estimate simultaneously all the incremental inductances l_{dd}, l_{dq}, and l_{qq} without the necessity of perform two tests. Moreover, while the previous techniques were tested at locked rotor or at steady-state fixed speed, the presented online identification method is tested also during load and speed transients showing a good match with the expected inductances. The proposed method requires to solve an online least-squares problem (ellipse fitting) and presents innovative analytical equations that link estimation error and incremental inductances. Experimental tests validate the proposed method.

6.2 Considered Motor

The motor considered in this work is a 2-kW SynRM. The convention used to define d- and q-axis is depicted in Figure 2.1a, and the main data of the motor are shown in

Table 6.1: Fit coefficients for the considered SynRM.

coefficient	value		coefficient	value
a_{d0}	2.03	H^{-1}	S	5.42
a_{dd}	2.20		T	0.39
a_{dq}	12.83		U	1.90
a_{q0}	2.89	H^{-1}	V	0
a_{qq}	20.53			

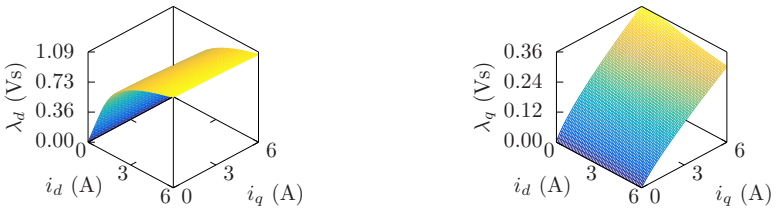

(a) d-axis flux linkage

(b) q-axis flux linkage

Figure 6.1: Measured (fitted) flux linkages.

Table 2.1. As concerns the flux linkages λ_d and λ_q, the motor has been characterized through experimental measurements [36]. The adopted characterization method required the use of a master motor to impose a speed of about 500 rpm. The flux linkages have been measured on a grid of stator currents (i_d, i_q) (Figure 2.3) and then fitted with the algebraic model proposed in [66]. The model is particularly useful since it is possible to describe the SynRM nonlinear characteristics with only 9 coefficients, shown in Table 6.1. The fitted flux linkages maps are depicted in Figure 6.1.

The incremental inductances (2.4) are computed as follows:

$$l_{dd} = \frac{\partial \lambda_d}{\partial i_d} \tag{6.1a}$$

$$l_{dq} = \frac{\partial \lambda_d}{\partial i_q} = \frac{\partial \lambda_q}{\partial i_d} \tag{6.1b}$$

$$l_{qq} = \frac{\partial \lambda_q}{\partial i_q} \tag{6.1c}$$

The so-computed incremental inductances, shown in Figure 6.2, will be used as a benchmark to validate the accuracy of the proposed identification method.

6.3 High-Frequency Model

The proposed identification technique relies on hf voltage injection on d- and q- axis and real-time processing of the measured currents. In particular, a rotating injection on d- and q- axis is adopted. It is worth noting that a position sensor (encoder or resolver) is required to inject the voltage signal on the real d- and q- axis. The d and

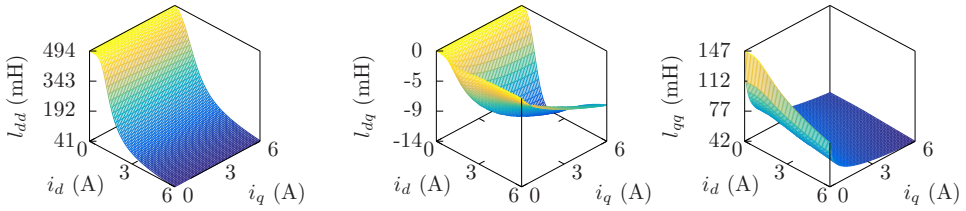

(a) d-axis incremental inductance

(b) mutual incremental inductance

(c) q-axis incremental inductance

Figure 6.2: Incremental inductances computed from the measured flux linkages.

q currents are measured, filtered, and processed online. The real-time processing consists of a least squares ellipse fitting and additional operations to compute the incremental inductances from the estimated ellipse coefficients.

The same assumptions for position estimation methods (based on saliency and signal injection) have to be verified. First of all, the proposed identification method can be used with motors characterized by rotor saliency, such as the SynRM, the PMA-SynRM and the IPMSM. Secondly, the frequency of the injected signals should be high enough to neglect the stator resistance effect on the estimation and, at the same time, the operating speed should be quite low (standstill or at the most 10% of the rated speed).
The hf model of a synchronous motor at quasi-zero speed is:

$$\begin{bmatrix} u_{hd}(t) \\ u_{hq}(t) \end{bmatrix} = \begin{bmatrix} l_{dd} & l_{dq} \\ l_{dq} & l_{qq} \end{bmatrix} \begin{bmatrix} \frac{\partial i_{hd}(t)}{\partial t} \\ \frac{\partial i_{hq}(t)}{\partial t} \end{bmatrix} \tag{6.2}$$

where u_{hd} and u_{hq} are the injected hf voltages and i_{hd} and i_{hq} the hf currents [39]. The adopted rotating voltage injection in the d- and q- axis is:

$$u_{hd}(t) = U_h \cos(\omega_h t) \tag{6.3a}$$
$$u_{hq}(t) = U_h \sin(\omega_h t) \tag{6.3b}$$

where U_h is the injection amplitude and $\omega_h = 2\pi f_h$, where f_h is the injection frequency. Once measured the stator currents i_d and i_q, the hf currents i_{hd} and i_{hq} are obtained through high-pass filtering. The hf currents can be expressed as:

$$i_{hd}(t) = \frac{U_h}{\omega_h (l_{dd}\, l_{qq} - l_{dq}^2)} \left[l_{dq} \cos(\omega_h t) + l_{qq} \sin(\omega_h t) \right] \tag{6.4a}$$
$$i_{hq}(t) = \frac{-U_h}{\omega_h (l_{dd}\, l_{qq} - l_{dq}^2)} \left[l_{dd} \cos(\omega_h t) + l_{dq} \sin(\omega_h t) \right] \tag{6.4b}$$

or, in matrix form:

$$\begin{bmatrix} i_{hd}(t) \\ i_{hq}(t) \end{bmatrix} = \begin{bmatrix} \frac{U_h\, l_{dq}}{\omega_h (l_{dq}\, l_{qq} - l_{dq}^2)} & \frac{U_h\, l_{qq}}{\omega_h (l_{dd}\, l_{qq} - l_{dq}^2)} \\ \frac{-U_h\, l_{dd}}{\omega_h (l_{dd}\, l_{qq} - l_{dq}^2)} & \frac{-U_h\, l_{dq}}{\omega_h (l_{dd}\, l_{qq} - l_{dq}^2)} \end{bmatrix} \begin{bmatrix} \cos(\omega_h t) \\ \sin(\omega_h t) \end{bmatrix} \tag{6.5}$$

From (6.5) it is possible to obtain $\cos(\omega_h t)$ and $\sin(\omega_h t)$ as:

$$\cos(\omega_h t) = -\frac{\omega_h \left[l_{dq}\, i_{hd}(t) + l_{qq}\, i_{hq}(t)\right]}{U_h} \tag{6.6a}$$

$$\sin(\omega_h t) = \frac{\omega_h \left[l_{dd}\, i_{hd}(t) + l_{dq}\, i_{hq}(t)\right]}{U_h} \tag{6.6b}$$

The hf currents can be written in implicit form replacing (6.6) in $\cos^2(\omega_h t) + \sin^2(\omega_h t) = 1$ and collecting the ellipse coefficents. Finally, the hf ellipse can be written as:

$$a\, i_{hd}(t)^2 + b\, i_{hd}(t)\, i_{hq}(t) + c\, i_{hq}(t)^2 + f = 0 \tag{6.7}$$

where the coefficients a, b, c and f are:

$$a = l_{dd}^2 + l_{dq}^2 \tag{6.8a}$$

$$b = 2\, l_{dq}\, (l_{dd} + l_{qq}) \tag{6.8b}$$

$$c = l_{qq}^2 + l_{dq}^2 \tag{6.8c}$$

$$f = -\frac{U_h^2}{\omega_h^2} \tag{6.8d}$$

The coefficients a, b, c depend on the operating point as well as the incremental inductances l_{dd}, l_{dq}, l_{qq}. On the other hand, the term f is constant if the injection amplitude and frequency U_h and f_h are not changed during an online operation.

Some additional parameters need to be introduced for the following analysis. The mean incremental inductance l_Σ (2.7) and the semi-difference incremental inductance l_Δ are:

$$l_\Sigma = \frac{l_{qq} + l_{dd}}{2} \tag{6.9a}$$

$$l_\Delta = \frac{l_{qq} - l_{dd}}{2} \tag{6.9b}$$

The incremental inductance l_Σ is known to be related to the positive-sequence current response [67,68]. On the other hand, the negative-sequence incremental inductance is:

$$l_{\text{neg}} = \sqrt{l_\Delta^2 + l_{dq}^2} \tag{6.10}$$

It can be seen that the terms l_Δ and l_{dq} are intrinsically linked in l_{neg}. The following analysis will focus on the separation of l_Δ from l_{dq}, a problem not yet addressed in literature. From now on, only the SynRM will be considered.

In order to split l_{neg} into l_Δ and l_{dq}, the knowledge of the estimation error ε (the error in the position estimation introduced by the cross-saturation effect [21]) is needed. The estimation error ε in the case of SynRM during a sensored operation is defined as:

$$\varepsilon = \frac{1}{2}\, \text{atan2}(l_{dq}, -l_\Delta) \tag{6.11}$$

Applying the properties of the function atan2, it is possible to re-write the estimation error with arctan as:

$$\varepsilon = \arctan\left(\frac{l_{dq}}{-l_\Delta + l_{\text{neg}}}\right) \tag{6.12}$$

This novel formulation can be exploited to compute:

$$\cos(\varepsilon) = \frac{1}{\sqrt{2}} \frac{-l_\Delta + l_{\text{neg}}}{\sqrt{l_{\text{neg}}^2 - l_\Delta\, l_{\text{neg}}}} \tag{6.13a}$$

$$\sin(\varepsilon) = \frac{1}{\sqrt{2}} \frac{l_{dq}}{\sqrt{l_{\text{neg}}^2 - l_\Delta\, l_{\text{neg}}}} \tag{6.13b}$$

The incremental inductances l_Δ and l_{dq} can be obtained from the incremental inductance l_{neg} and the estimation error ε with:

$$l_\Delta = l_{\text{neg}}\,(1 - 2\cos^2(\varepsilon)) \tag{6.14a}$$

$$l_{dq} = \sqrt{2}\,\sqrt{l_{\text{neg}}^2 - l_\Delta\, l_{\text{neg}}}\,\sin(\varepsilon) \tag{6.14b}$$

These equations are valid for other conventional signal injection methods as well, since the estimation error ε can be simply obtained subtracting the estimated position from the measured one during a sensored operation with the position observer in open loop. The proposed method, as will be explained in the following section, computes both l_{neg} and ε from the estimated ellipse coefficients a, b, and c.

6.4 Proposed Method

The proposed control scheme is depicted in Figure 6.3. A conventional control scheme with PI controllers is adopted. A position sensor is used to measure the rotor position and feed the Park transformation. The identification method consists of a hf voltage injection, an ellipse fitting procedure, and the HPF and LPF filters superimposed to the PI control scheme. In particular, a rotating voltage vector is injected, consisting of two pulsating phase-shifted signals in the d- and q- axis (6.3). A high-pass filter is adopted to extract the hf currents (6.4) which feed the ellipse fitting procedure. A low-pass filter is used to remove the hf component in the current control loop; however, the low-pass filter is not mandatory and it can even be removed [69].

An ellipse fitting procedure is used to estimate in real-time the ellipse coefficients a, b, c associated to the hf currents i_{hd} and i_{hq}. The ellipse fitting of the current response locus has already been proposed in literature in the case of rotating injection in the stationary reference frame $\alpha\beta$ [19, 20]. The least squares problem associated to the ellipse fitting can be computational demanding if directly solved. Thus, a recursive solution method [19] and a recursive QR factorization technique [20] have been proposed in order the reduce the computational effort and guarantee the real-time operation of the ellipse fitting. Both methods can estimate the coefficients a, b, c of a rotating ellipse in $\alpha\beta$. The forgetting factor should accurately be tuned according to the rotating speed in order to guarantee a compromise between bias and variance estimation error [20].

The ellipse fitting is executed in dq in the proposed configuration. The main advantage of operating in dq is that a stationary ellipse can be detected, avoiding the speed-dependent forgetting factor tuning. As shown in Figure 6.3, the i_{hd} and i_{hq} current samples are processed by the real-time fitting and the ellipse coefficients a, b, c are estimated. The estimated coefficients can be used to compute online the

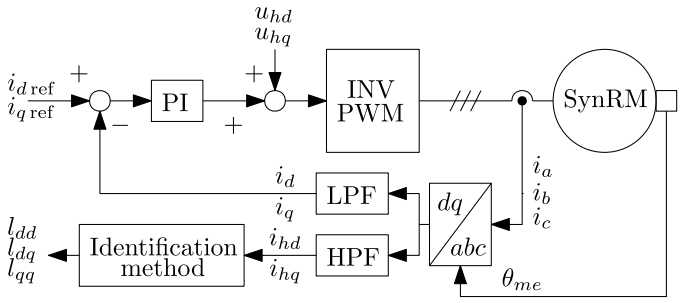

Figure 6.3: Proposed identification method scheme.

incremental inductances l_Σ and l_{neg}:

$$l_\Sigma = \frac{1}{2}\sqrt{a + c + \sqrt{4ac - b^2}} \tag{6.15a}$$

$$l_{\mathrm{neg}} = \frac{1}{2}\sqrt{\frac{b^2 + (a-c)^2}{a + c + \sqrt{4ac - b^2}}} \tag{6.15b}$$

The coefficients a, b, c can be also used to compute ellipse tilt angle caused by the cross-saturation effect, which corresponds (in the case of SynRM during a sensored operation) to:

$$\varepsilon = \frac{1}{2}\,\mathrm{atan2}(b,\, a - c) \tag{6.16}$$

The following step consists in splitting the negative-sequence incremental inductance l_{neg} (6.15b) into l_Δ and l_{dq} using the estimation error ε from (6.16). Equations (6.14) can be used for this purpose. The semi-difference incremental inductance l_Δ and the cross-saturation inductance l_{dq} are now available.

The last step consists in computing l_{dd} and l_{qq} using l_Σ estimated from (6.15a) and l_Δ:

$$l_{dd} = l_\Sigma - l_\Delta \tag{6.17a}$$

$$l_{qq} = l_\Sigma + l_\Delta \tag{6.17b}$$

The incremental inductances l_{dd}, l_{dq} and l_{qq} have been finally identified.

The following section will focus on the accuracy of the identification method at standstill and during speed and load transients.

The following equations hold in the case of PMA-SynRM *and* IPMSM:

$$\varepsilon = \frac{1}{2}\,\mathrm{atan2}(-b,\, c-a) = \frac{1}{2}\,\mathrm{atan2}(-l_{dq},\, l_\Delta) = \arctan\left(\frac{-l_{dq}}{l_\Delta + l_{\mathrm{neg}}}\right) \tag{6.18a}$$

$$\cos(\varepsilon) = \frac{1}{\sqrt{2}}\,\frac{l_\Delta + l_{\mathrm{neg}}}{\sqrt{l_{\mathrm{neg}}^2 + l_\Delta\, l_{\mathrm{neg}}}} \tag{6.18b}$$

$$\sin(\varepsilon) = \frac{1}{\sqrt{2}}\,\frac{-l_{dq}}{\sqrt{l_{\mathrm{neg}}^2 + l_\Delta\, l_{\mathrm{neg}}}} \tag{6.18c}$$

$$l_\Delta = l_{\mathrm{neg}}\,(2\cos^2(\varepsilon) - 1) \tag{6.18d}$$

$$l_{dq} = -\sqrt{2}\,\sqrt{l_{\mathrm{neg}}^2 + l_\Delta\, l_{\mathrm{neg}}}\,\sin(\varepsilon) \tag{6.18e}$$

The convention used to define d- and q- axis for a PMA-SynRM *or a* IPMSM *is depicted in* Figure 2.1b.

6.5 Experimental Results

The proposed identification method has been validated in two scenarios. The first test consisted of locking the rotor and analyzing the estimation accuracy in a grid of operating current points, while the second tests consisted of coupling the SynRM to a load motor and controlling the speed while varying the load torque. The experimental setup was composed by a dSPACE MicroLabBox and a three-phase inverter. The sampling frequency was set to $f_c = 10$ kHz. In both the tests the injected voltage had amplitude $U_h = 40$ V and frequency $f_h = 1$ kHz. These values appear to be adequate for the considered motor and the chosen sampling frequency. The following considerations have been drawn. The amplitude of the injected voltage U_h should be as low as possible in order to reduce acoustic noise and core losses, but it should be high enough in order to make the hf currents detectable and distinguishable from the current measurement noise. It has been verified that $U_h = 40$ V is a good compromise for the considered SynRM. Fixed the sampling frequency f_c, the injection frequency f_h must not be less than one fifth of f_c. In fact, the ratio between f_c and f_h corresponds to the number of points considered in the buffer of the ellipse fitting procedure. It is evident that the quality of the estimate increases with the number of points which constitute the circumference of the measured current ellipse. A buffer of 10 points, as the one adopted in the experimental tests, has been found satisfactory. As concerns the HPFs and LPFs, four digital first-order infinite impulse response (IIR) filters have been adopted [20]. The cut-off frequency has been set to 100 Hz for both HPFs and LPFs.

Figure 6.4 shows the results of the first test with the rotor locked. The rotor has been locked with a mechanical brake at the position $\theta_{me} = 0$. The incremental inductances $\widetilde{l}_{dd}$, $\widetilde{l}_{qq}$ and $\widetilde{l}_{dq}$ have been estimated online and stored without the need of post processing. The algorithm has been tested on a grid of currents from 0 to 6 A, with a step of 0.1 A. The sequence of 61×61 reference currents $(i_d,\, i_q)$ has been applied with the same pattern used in [70]. Considering a time step of 6 ms for each reference operating point, the total time required for the mapping was about

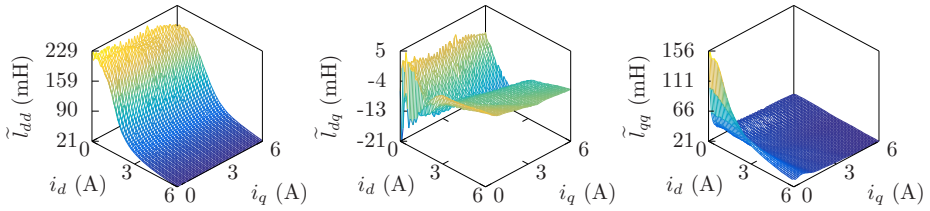

(a) d-axis incremental inductance (b) mutual incremental inductance (c) q-axis incremental inductance

Figure 6.4: Estimated incremental inductances at $\theta_{me} = 0$ (first test).

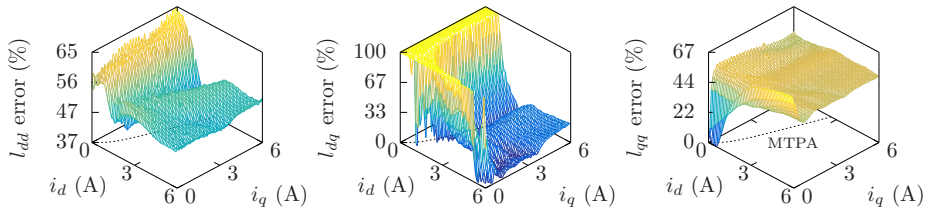

(a) $\widetilde{l}_{dd}$ percentage error (b) $\widetilde{l}_{dq}$ percentage error (c) $\widetilde{l}_{qq}$ percentage error

Figure 6.5: Percentage error between the estimated incremental inductances at $\theta_{me} = 0$ (first test) and the incremental inductances obtained from the flux-linkage characterization performed at 500 rpm. The MTPA trajectory of the considered SynRM is shown in dashed line.

22 s. Figure 6.5 shows the percentage error between the estimated incremental inductances at $\theta_{me} = 0$ (Figure 6.4) and the incremental inductances obtained from the flux-linkage characterization performed at 500 rpm (Figure 6.2). The accuracy of the method depends on the operating point. The $\widetilde{l}_{dd}$ percentage error is higher when the current i_{dd} is close to zero, while $\widetilde{l}_{qq}$ percentage error is around 40% in most of the considered current grid. Conversely, the $\widetilde{l}_{dq}$ percentage error appears to be remarkable along the dq axes and less than 30% at higher current values. The accuracy of the presented method can be assumed acceptable considering that all the estimation procedure can be carried on without knowledge of any motor parameters and without considering the effect of the rotor positon on the estimation. The accuracy of the method presented in [65], which is an offline and not online estimation, is between 10% and 20% depending on the operating point.

The results of the second test are reported in Figure 6.6. The SynRM is coupled with a load motor which initially produces no torque. A 150-rpm speed reference step is set after 2 s from the beginning of the test, as shown in Figure 6.6a. Then, a trapezoidal-shape load torque is imposed by the load motor maintaining the 150-rpm speed reference. The MTPA, shown in (Figure 6.5), is the reference trajectory for the current control loop. The measured stator currents are depicted in Figure 6.6b. The rated current amplitude of 6 A is reached during the load torque application.

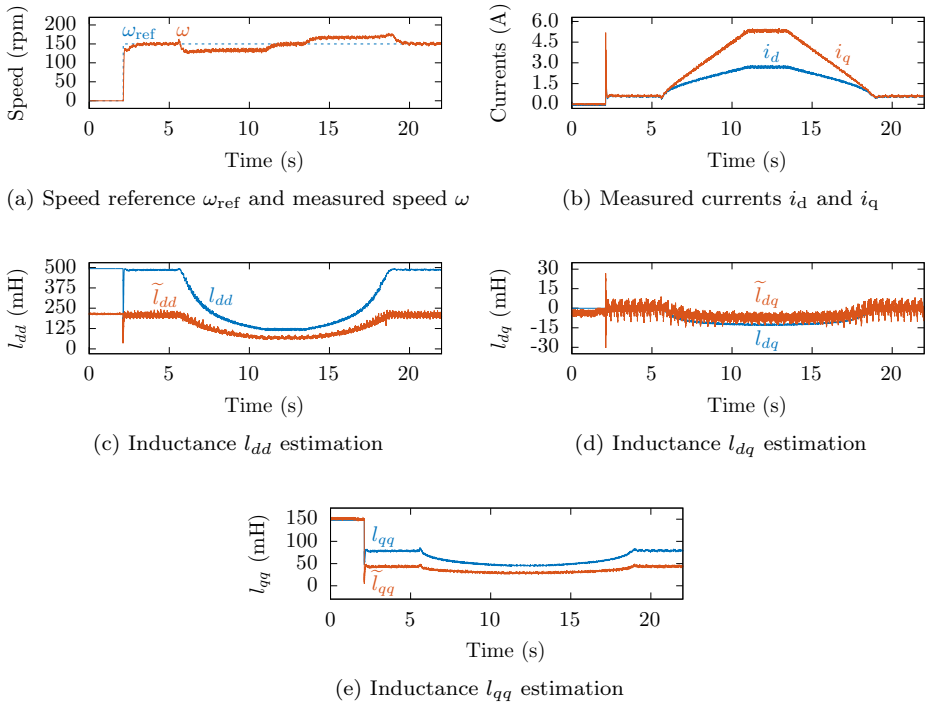

(a) Speed reference ω_{ref} and measured speed ω

(b) Measured currents i_{d} and i_{q}

(c) Inductance l_{dd} estimation

(d) Inductance l_{dq} estimation

(e) Inductance l_{qq} estimation

Figure 6.6: Results of the proposed identification method during speed and load transients (second test). The MTPA is the reference trajectory for the current control loop. l_{dd}, l_{dq}, l_{qq} are the incremental inductances obtained from the flux-linkage characterization, computed offline through lookup table. $\widetilde{l}_{dd}$, $\widetilde{l}_{dq}$, $\widetilde{l}_{qq}$ are the incremental inductances estimated online.

Figure 6.6c, Figure 6.6e and Figure 6.6d show the online estimated inductances $\widetilde{l}_{dd}$, $\widetilde{l}_{dq}$, $\widetilde{l}_{qq}$ and the expected inductances l_{dd}, l_{dq}, l_{qq} during the whole test. It is worth noting that, even during the load transients, the estimation accuracy is consistent with locked-rotor test (Figure 6.4). Complementarily to the first standstill test, the method appears to be effective also during the second test characterized by a conventional operation. The chosen speed of 150 rpm can be assumed the upper limit for the considered SynRM for low speed signal injection techniques, consistently with the signal injection position estimation techniques which are usually valid up to a tenth of the rated motor speed.

6.6 Conclusions

The chapter presents a novel identification method for reluctance and interior permanent magnet synchronous motors. The motor incremental inductances can be estimated online using a rotating high-frequency injection and a computationally efficient ellipse fitting. The relationship between the ellipse coefficients, the position estimation error and the incremental inductances are clearly explained and presented. The identification method has been tested on a SynRM both at standstill

and during load and speed transients. The results are compared with a conventional flux linkages measurements technique.

General Conclusions

This work focuses on signal-injection sensorless control for permanent magnet synchronous motors. Hereafter the main conclusions are reported.

Self-sensing capabilities

In Chapter 2 a systematic and comprehensive model for synchronous motors has been presented. Starting from the non-linear flux-linkages maps, it is possible to compute and predict the self-sensing capabilities (saliency, estimation error, convergence region) of the considered motor. Both simulated and measured flux-linkages maps can be used. The proposed computational approach is verified by means of experiments.

In Chapter 3 the experimental method to measure the sensored and sensorless trajectories is explained. The results are compared with the computational approach proposed in Chapter 2, showing a good match.

The computation and the measurement of the convergence region are valid not only in the case of rotating injection and ellipse fitting, but also in the case of pulsating and rotating injection with demodulation. In fact, as explained in Chapter 1, different injection schemes exploit the same principle of extracting the rotor position information from the high frequency current response. Analytical equations show the similarities of the methods as concerns the signal I_{hq} (responsible for the position estimation algorithm convergence).

Ellipse fitting

Conventional signal-injection techniques require a demodulation scheme to estimate the rotor position from the measured currents. In this work, an innovative ellipse fitting method robust to signal processing delay effects is proposed. In Chapter 4 the problem related to the ellipse fitting is solved through recursive least square estimator, while in Chapter 5 the problem is recursively solved using an efficient updating QR factorization. In both cases the tuning of only one parameter (called forgetting factor) is required, making the studied methods suitable for industrial application thanks to their minimal setup effort.

Incremental Inductances Estimation

An online incremental (differential) inductances estimation algorithm for synchronous reluctance motors is presented in Chapter 6. The proposed technique is the first parameter estimation scheme for signal-injection schemes carried out completely online. The method is validated both at locked rotor (on a grid of operating points i_d-i_q) and with load transients during a closed-loop speed control.

As future works, the accuracy of the incremental inductance method should be improved. It would be also very interesting validating the method for motors, such as IPMs and PMASynRMs.

Appendix A

Simulink Model

Abstract - A PMSM can be characterized, in terms of flux linkages, through experimental measurements or finite element analysis. The goal of this appendix is to explain how to create the non-linear model, in Simulink, of a synchronous reluctance or permanent magnet motor starting from its flux-linkage maps.

Simulink is the recommended tool to simulate an electrical motor as concerns dynamic simulations and control validation. Dynamic simulations are in time domain, meaning that electrical and mechanical transients can be studied. Regarding control validation, the use of Simulink allows to test the control algorithm without a physical motor and test bench. Adopting an accurate model it is possible to take into account the non-linearities and speed up the control prototyping procedure.

PMSM modeling has already been addressed [70–81]. As shown in [80], a synchronous motor can be modeled in Simulink considering either the flux linkages or the currents as state variables. The first type of model is the Flux Model, the latter the Current Model [80]. Both the models are obtained from the flux-linkage maps, that is the relationship between flux linkages and currents stated by experimental results and finite element analysis. Together with the Flux Model and Current Model, also the SynRM Model [71] will be considered in this appendix.

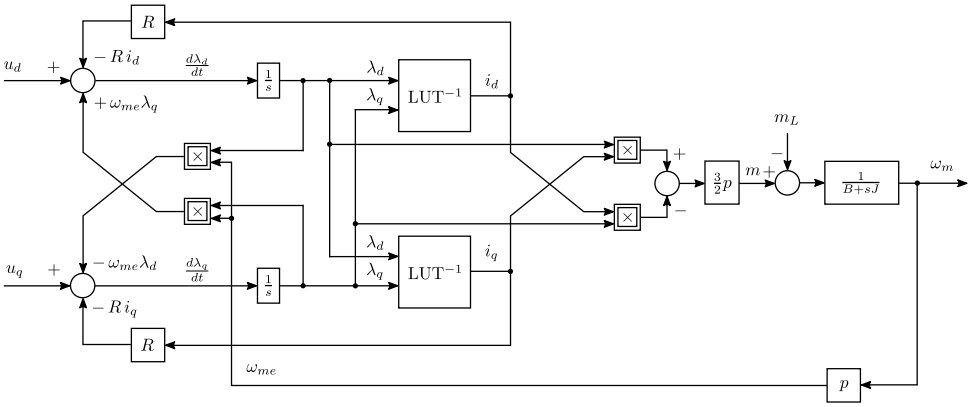

Figure A.1: Flux Model scheme.

Flux Model

The Flux Model is explained first. Consider the voltage equations of a PMSM (2.1):

$$\begin{aligned} u_d &= R\,i_d + \frac{d\lambda_d}{dt} - \omega_{me}\,\lambda_q \\ u_q &= R\,i_q + \frac{d\lambda_q}{dt} + \omega_{me}\,\lambda_d \end{aligned} \tag{A.1}$$

Rearranging the previous equations it is possible to obtain:

$$\begin{aligned} \frac{d\lambda_d}{dt} &= u_d - Ri_d + \omega_{me}\lambda_q \\ \frac{d\lambda_q}{dt} &= u_q - Ri_q - \omega_{me}\lambda_d \end{aligned} \tag{A.2}$$

Moreover, the torque m can be computed from the flux linkages and the currents (2.11):

$$m = \frac{3}{2}\,p\,[\lambda_d\,i_q - \lambda_q\,i_d] \tag{A.3}$$

The Flux Model scheme, depicted in Figure A.1, relies on equations (A.2) and (2.11). As can be seen, the flux linkages λ_d and λ_q are obtained integrating respectively $\frac{d\lambda_d}{dt}$ and $\frac{d\lambda_q}{dt}$. The currents i_d and i_q are calculated interpolating the content of inverted Lookup Tables (LUT^{-1}). The procedure required to obtain the LUT^{-1} will be explained later. The LUT^{-1} implemented in the scheme of Figure A.1 use linear interpolation.

In the Flux Model, the flux linkages are state variables. In fact, they are obtained using Integrator blocks. Since definite integrals are computed, the constants of integration (respectively λ_{d0} and λ_{q0}) can not be neglected:

$$\begin{aligned} \lambda_d &= \int (u_d - R\,i_d + \omega_{me}\lambda_q)\,dt \; + \lambda_{d0} \\ \lambda_q &= \int (u_q - R\,i_q - \omega_{me}\lambda_d)\,dt \; + \lambda_{q0} \end{aligned} \tag{A.4}$$

(a) Direct Lookup Table

(b) Inverted Lookup Table

Figure A.2: Graphical convention used for representing the direct and inverted Lookup Tables of generic quantities x and y. It is worth noticing that LUT requires as input the currents i_d, i_q, while LUT^{-1} requires the fluxes λ_d, λ_q.

The user can modify λ_{d0} and λ_{q0} inside the Integrator block options. If no value is set, Simulink considers $\lambda_{d0} = 0$ and $\lambda_{q0} = 0$ as default. This particular condition is correct for a synchronous reluctance motor (REL), when the currents are equal to zero. If a PM motor is considered, λ_{d0} should be set equal to the permanent magnet flux (λ_{PM}) in order to force the currents equal to zero at the beginning of the simulation.

In general, in a Flux Model, the initial conditions λ_{d0} and λ_{q0} should be modified accordingly to the desired values of the currents at the beginning of the simulation. In analytical terms:

$$\begin{aligned} \lambda_d &= \int (u_d - R\, i_d + \omega_{me} \lambda_q)\, dt \; + \; \lambda_d(i_{d0}, i_{q0}) \\ \lambda_q &= \int (u_q - R\, i_q - \omega_{me} \lambda_d)\, dt \; + \; \lambda_q(i_{d0}, i_{q0}) \end{aligned} \tag{A.5}$$

Using this strategy, the user can start a simulation with any desidered value of the currents (i_{d0}, i_{q0}).

Through experimental measurements or finite element analysis it is possible to obtain the relationships $\lambda_d(i_d, i_q)$, $\lambda_q(i_d, i_q)$, also known as "direct maps". The direct maps can be interpolated in Simulink through direct Lookup Tables (LUT). Anyway, these maps must be inverted into LUT^{-1} $i_d(\lambda_d, \lambda_q)$, $i_q(\lambda_d, \lambda_q)$ maps for the Flux Model implementation, as shown in Figure A.1. The convention used for representing LUT and LUT^{-1} is defined in Figure A.2.

The procedure required to obtain the LUT^{-1} relies on the use of the following MATLAB functions: `griddata`[1] and `scatteredInterpolant`[2]. In a nutshell, the measured flux linkages $\lambda_d(i_d, i_q)$, $\lambda_q(i_d, i_q)$ are defined over a regular grid of currents. If the currents are expressed as a function of the flux linkages, scattered data in the form $i_d(\lambda_d, \lambda_q)$, $i_q(\lambda_d, \lambda_q)$ is obtained. The scattered data must be interpolated on a query grid (a user-defined regular grid of flux-linkages) to obtain the LUT^{-1}.

As concerns the interpolating functions, `scatteredInterpolant` is to be preferred over `griddata` since it is capable of extrapolating data. On the other hand, `griddata` is available in Python[3].

[1] https://www.mathworks.com/help/matlab/ref/griddata.html
[2] https://www.mathworks.com/help/matlab/ref/scatteredinterpolant.html
[3] https://docs.scipy.org/doc/scipy/reference/generated/scipy.interpolate.griddata.html

Current Model

In the following section the Current Model will be analysed. The Current Model is based on the inverse incremental inductances of the motor (LUT), thus it does not require the inverted flux-linkage maps (LUT^{-}1).

Consider equation (2.1), and in particular the terms $\frac{d\lambda_d}{dt}$ and $\frac{d\lambda_q}{dt}$. Adding the dependency of the flux linkages with the currents, and applying the chain rule, it follows that:

$$\begin{aligned} \frac{d\lambda_d(i_d,i_q)}{dt} &= \frac{\partial\lambda_d(i_d,i_q)}{\partial i_d}\frac{di_d}{dt} + \frac{\partial\lambda_d(i_d,i_q)}{\partial i_q}\frac{di_q}{dt} \\ \frac{d\lambda_q(i_d,i_q)}{dt} &= \frac{\partial\lambda_q(i_d,i_q)}{\partial i_d}\frac{di_d}{dt} + \frac{\partial\lambda_q(i_d,i_q)}{\partial i_q}\frac{di_q}{dt} \end{aligned} \tag{A.6}$$

or, in matrix form:

$$\begin{bmatrix} \frac{d\lambda_d}{dt} \\ \frac{d\lambda_q}{dt} \end{bmatrix} = \begin{bmatrix} l_{dd}(i_d,i_q) & l_{dq}(i_d,i_q) \\ l_{qd}(i_d,i_q) & l_{qq}(i_d,i_q) \end{bmatrix} \begin{bmatrix} \frac{di_d}{dt} \\ \frac{di_q}{dt} \end{bmatrix} \tag{A.7}$$

where the matrix of the incremental inductances (2.4) is defined as:

$$\begin{bmatrix} l_{dd}(i_d,i_q) & l_{dq}(i_d,i_q) \\ l_{qd}(i_d,i_q) & l_{qq}(i_d,i_q) \end{bmatrix} = \begin{bmatrix} \frac{\partial\lambda_d(i_d,i_q)}{\partial i_d} & \frac{\partial\lambda_d(i_d,i_q)}{\partial i_q} \\ \frac{\partial\lambda_q(i_d,i_q)}{\partial i_d} & \frac{\partial\lambda_q(i_d,i_q)}{\partial i_q} \end{bmatrix} \tag{A.8}$$

From equation (A.7) it is possible to extract the currents derivatives:

$$\begin{bmatrix} \frac{di_d}{dt} \\ \frac{di_q}{dt} \end{bmatrix} = \begin{bmatrix} \gamma_d(i_d,i_q) & \gamma_{dq}(i_d,i_q) \\ \gamma_{qd}(i_d,i_q) & \gamma_q(i_d,i_q) \end{bmatrix} \begin{bmatrix} \frac{d\lambda_d}{dt} \\ \frac{d\lambda_q}{dt} \end{bmatrix} \tag{A.9}$$

where the matrix of the inverse incremental inductances (2.8) is defined as the inverse of the matrix of the inductances:

$$\begin{bmatrix} \gamma_d(i_d,i_q) & \gamma_{dq}(i_d,i_q) \\ \gamma_{qd}(i_d,i_q) & \gamma_q(i_d,i_q) \end{bmatrix} = \begin{bmatrix} l_{dd}(i_d,i_q) & l_{dq}(i_d,i_q) \\ l_{qd}(i_d,i_q) & l_{qq}(i_d,i_q) \end{bmatrix}^{-1} \tag{A.10}$$

Expanding (A.9) it is possible to obtain:

$$\begin{aligned} \frac{di_d}{dt} &= \gamma_d(i_d,i_q)\frac{d\lambda_d}{dt} + \gamma_{dq}(i_d,i_q)\frac{d\lambda_q}{dt} \\ \frac{di_q}{dt} &= \gamma_{qd}(i_d,i_q)\frac{d\lambda_d}{dt} + \gamma_q(i_d,i_q)\frac{d\lambda_q}{dt} \end{aligned} \tag{A.11}$$

The Current Model scheme, shown in Figure A.3, is based on equation (A.11) and equation (A.2). In this scheme, LUT for λ_d and λ_q use linear (linear point-slope) interpolation, while LUT for γ_d, γ_{dq}, γ_{qd} and γ_q use flat (constant) interpolation. The incremental inductances, and consequently the inverse incremental inductances, are computed deriving the flux linkages using the difference quotient. Since the flux linkages are linear between the known points, it follows that their derivative is constant. This is the reason why the Lookup Tables γ_d, γ_{dq}, γ_{qd} and γ_q should use flat interpolation.

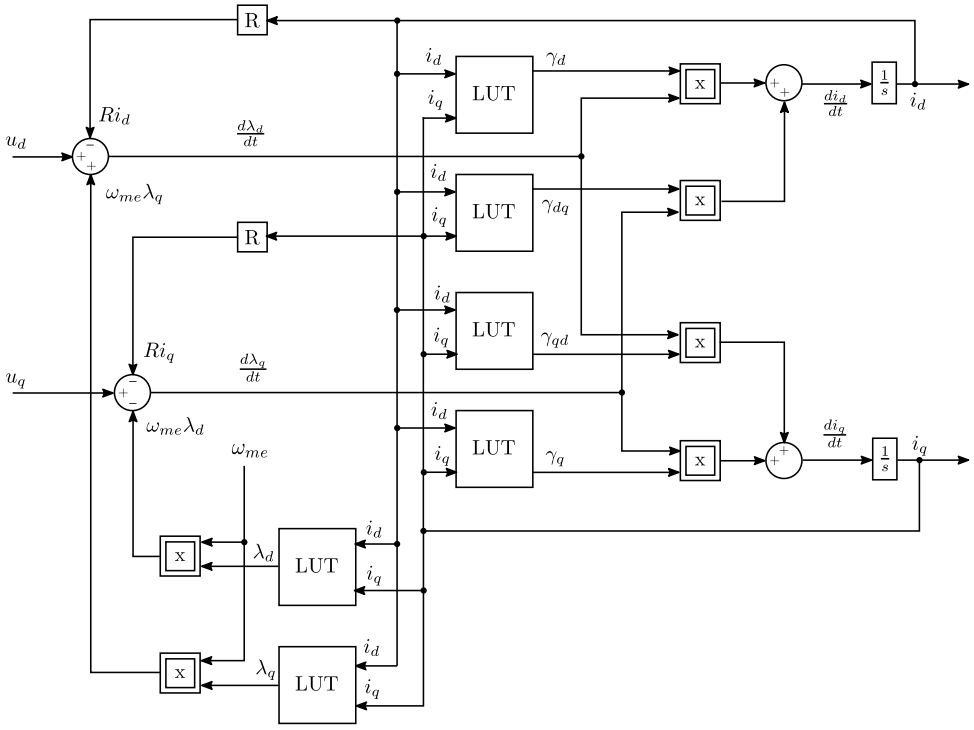

Figure A.3: Current Model scheme.

In the Current Model, the currents are state variables. They are obtained as follows:

$$\begin{aligned} i_d &= \int \left(\gamma_d(i_d, i_q) \frac{d\lambda_d}{dt} + \gamma_{dq}(i_d, i_q) \frac{d\lambda_q}{dt} \right) dt + i_{d0} \\ i_q &= \int \left(\gamma_{qd}(i_d, i_q) \frac{d\lambda_d}{dt} + \gamma_q(i_d, i_q) \frac{d\lambda_q}{dt} \right) dt + i_{q0} \end{aligned} \tag{A.12}$$

Regarding the initial values i_{d0} and i_{q0}, they can be directly chosen by the user. If no values is set, the simulation will start with null corrents both in the case of REL motor and PM motor. Thus, the setup of i_{d0} and i_{q0}, in a Current Model, is very simple and direct. In a Flux Model, forcing i_{d0} and i_{q0} it is not so immediate because the user can act only on the values of λ_{d0} and λ_{q0}.

The procedure to create the Current Model from the flux-linkage maps consists in two parts: the computation of the incremental inductances l_{dd}, l_{dq}, l_{qd}, l_{qq} (Figure 2.8) and the computation of the inverse incremental inductances γ_d, γ_{dq}, γ_{qd} and γ_q (Figure 2.10). The corresponding functions are implemented in Apollo[4]:

- `calc_incremental_inductances(method='diff')`
- `mot.calc_inverse_incremental_inductances()`

[4]https://gitlab.com/LuigiAlberti/dolomites-python (free code)

SynRM Model

Hinkkanen et al. proposed an algebraic model proposed for the SynRM [66]. The model is particularly useful since it is possible to describe the SynRM nonlinear characteristics with only 9 coefficients (5 parameters $a_{d0}, a_{dd}, a_{dq}, a_{q0}, a_{qq}$ and 4 exponents S, T, U, V):

$$\begin{aligned} i_d(\lambda_d, \lambda_q) &= \left(a_{d0} + a_{dd}|\lambda_d|^S + \frac{a_{dq}}{V+2}|\lambda_d|^U|\lambda_q|^{V+2} \right) \lambda_d \\ i_q(\lambda_d, \lambda_q) &= \left(a_{q0} + a_{qq}|\lambda_q|^T + \frac{a_{dq}}{U+2}|\lambda_d|^{U+2}|\lambda_q|^V \right) \lambda_q \end{aligned} \tag{A.13}$$

It is worth noting that in (A.13) the currents are expressed as function of the flux linkages. Thus, $i_d(\lambda_d, \lambda_q)$ and $i_q(\lambda_d, \lambda_q)$ are already in the form of LUT^{-1}, that makes (A.13) easily implementable in the Flux Model (Figure A.1) using MATLAB functions, getting rid of the Lookup Tables interpolations.

The coefficients of (A.13) can be obtained through a fitting procedure, implemented in Apollo[5] as `fit_flux_SynRM()`. Starting data $\lambda_d(i_d, i_q), \lambda_q(i_d, i_q)$ is conventionally measured (or simulated) on a grid of stator currents (i_d, i_q), but the function is valid also in the case of scattered data. Once obtained the 9 coefficients of (A.13), it is possible to recalculate the fitted fluxes on a new query grid (that can be even larger than the starting one).

Another advantage of the proposed SynRM model is that the incremental parameters can be computed and monitored in real-time in the Simulink model. Starting from (A.13), the derivatives of the currents i_d and i_q with respect to the flux linkages λ_d and λ_q (i.e. the inverse incremental inductances) are:

$$\begin{aligned} \gamma_{dd}(\lambda_d, \lambda_q) &= a_{d0} + a_{dd}(S+1)|\lambda_d|^S + \frac{a_{dq}}{V+2}(U+1)|\lambda_d|^U|\lambda_q|^{V+2} \\ \gamma_{dq}(\lambda_d, \lambda_q) &= a_{dq}|\lambda_d|^U\lambda_d\frac{|\lambda_q|^{V+2}}{\lambda_q} \\ \gamma_{qd}(\lambda_d, \lambda_q) &= a_{dq}|\lambda_q|^V\lambda_q\frac{|\lambda_d|^{U+2}}{\lambda_d} \\ \gamma_{qq}(\lambda_d, \lambda_q) &= a_{q0} + a_{qq}(T+1)|\lambda_q|^T + \frac{a_{dq}}{U+2}(V+1)|\lambda_d|^{U+2}|\lambda_q|^V \end{aligned} \tag{A.14}$$

[5] https://gitlab.com/LuigiAlberti/dolomites-python (free code)

The incremental inductances can be computed with:

$$
\begin{aligned}
l_{dd}(\lambda_d, \lambda_q) &= \frac{\gamma_{qq}(\lambda_d, \lambda_q)}{\gamma_{dd}(\lambda_d, \lambda_q)\gamma_{qq}(\lambda_d, \lambda_q) - \gamma_{dq}(\lambda_d, \lambda_q)\gamma_{qd}(\lambda_d, \lambda_q)} \\
l_{dq}(\lambda_d, \lambda_q) &= \frac{-\gamma_{dq}(\lambda_d, \lambda_q)}{\gamma_{dd}(\lambda_d, \lambda_q)\gamma_{qq}(\lambda_d, \lambda_q) - \gamma_{dq}(\lambda_d, \lambda_q)\gamma_{qd}(\lambda_d, \lambda_q)} \\
l_{qd}(\lambda_d, \lambda_q) &= \frac{-\gamma_{qd}(\lambda_d, \lambda_q)}{\gamma_{dd}(\lambda_d, \lambda_q)\gamma_{qq}(\lambda_d, \lambda_q) - \gamma_{dq}(\lambda_d, \lambda_q)\gamma_{qd}(\lambda_d, \lambda_q)} \\
l_{qq}(\lambda_d, \lambda_q) &= \frac{\gamma_{dd}(\lambda_d, \lambda_q)}{\gamma_{dd}(\lambda_d, \lambda_q)\gamma_{qq}(\lambda_d, \lambda_q) - \gamma_{dq}(\lambda_d, \lambda_q)\gamma_{qd}(\lambda_d, \lambda_q)}
\end{aligned}
\tag{A.15}
$$

The model proposed in this section is valid only for SynRM, while the Flux Model and the Current Model can be used for any other type of permanent magnet motor (SPM, IPM, SynRM, PMA-SynRM).

Bibliography

[1] M. J. Corley and R. D. Lorenz, "Rotor position and velocity estimation for a salient-pole permanent magnet synchronous machine at standstill and high speeds," *IEEE Transactions on Industry Applications*, vol. 34, no. 4, pp. 784–789, 7 1998.

[2] Y. Zhao, Z. Zhang, W. Qiao, and L. Wu, "An extended flux model-based rotor position estimator for sensorless control of salient-pole permanent-magnet synchronous machines," *IEEE Transactions on Power Electronics*, vol. 30, no. 8, pp. 4412–4422, 10 2015.

[3] I. Boldea, M. C. Paicu, and G. Andreescu, "Active flux concept for motion-sensorless unified ac drives," *IEEE Transactions on Power Electronics*, vol. 23, no. 5, pp. 2612–2618, 9 2008.

[4] J. M. Liu and Z. Q. Zhu, "Rotor position estimation for dual-three-phase permanent magnet synchronous machine based on third harmonic back-emf," in *2015 IEEE Symposium on Sensorless Control for Electrical Drives (SLED)*, 6 2015, pp. 1–8.

[5] S. Bolognani, S. Calligaro, and R. Petrella, "Design issues and estimation errors analysis of back-emf based position and speed observer for spm synchronous motors," in *2011 Symposium on Sensorless Control for Electrical Drives*, 9 2011, pp. 138–145.

[6] R. Antonello, L. Ortombina, F. Tinazzi, and M. Zigliotto, "Enhanced low-speed operations for sensorless anisotropic pm synchronous motor drives by a modified back-emf observer," *IEEE Transactions on Industrial Electronics*, vol. 65, no. 4, pp. 3069–3076, 4 2018.

[7] H. Kim, K. Huh, R. D. Lorenz, and T. M. Jahns, "A novel method for initial rotor position estimation for ipm synchronous machine drives," *IEEE Transactions on Industry Applications*, vol. 40, no. 5, pp. 1369–1378, 9 2004.

[8] Y. Jeong, R. D. Lorenz, T. M. Jahns, and S. Sul, "Initial rotor position estimation of an interior permanent-magnet synchronous machine using carrier-frequency injection methods," *IEEE Transactions on Industry Applications*, vol. 41, no. 1, pp. 38–45, 1 2005.

[9] D. Raca, P. Garcia, D. D. Reigosa, F. Briz, and R. D. Lorenz, "Carrier-signal selection for sensorless control of pm synchronous machines at zero and very low speeds," *IEEE Transactions on Industry Applications*, vol. 46, no. 1, pp. 167–178, 1 2010.

[10] S. Yang and Y. Hsu, "Full speed region sensorless drive of permanent-magnet machine combining saliency-based and back-emf-based drive," *IEEE Transactions on Industrial Electronics*, vol. 64, no. 2, pp. 1092–1101, 2 2017.

[11] A. Faggion, N. Bianchi, and S. Bolognani, "Ringed-pole permanent-magnet synchronous motor for position sensorless drives," *IEEE Transactions on Industry Applications*, vol. 47, no. 4, pp. 1759–1766, 7 2011.

[12] O. B. Abdallah, A. Masmoudi, M. Berto, L. Alberti, and S. Bolognani, "Rotating high frequency injection and ellipse fitting technique for ringed-pole motor sensorless control," in *2020 Fifteenth International Conference on Ecological Vehicles and Renewable Energies (EVER)*, 9 2020, pp. 1–6.

[13] J. Jang, J. Ha, M. Ohto, K. Ide, and S. Sul, "Analysis of permanent-magnet machine for sensorless control based on high-frequency signal injection," *IEEE Transactions on Industry Applications*, vol. 40, no. 6, pp. 1595–1604, 11 2004.

[14] W. Hammel and R. M. Kennel, "Position sensorless control of pmsm by synchronous injection and demodulation of alternating carrier voltage," in *2010 First Symposium on Sensorless Control for Electrical Drives*, 7 2010, pp. 56–63.

[15] V. Manzolini and S. Bolognani, "On the rotor position self-sensing capability of reluctance and ipm synchronous motors," *IEEE Transactions on Industry Applications*, pp. 1–1, 2020.

[16] Y. Kwon, J. Lee, and S. Sul, "Extending operational limit of ipmsm in signal-injection sensorless control by manipulation of convergence point," *IEEE Transactions on Industry Applications*, vol. 55, no. 2, pp. 1574–1586, 3 2019.

[17] R. D. Lorenz, "Practical issues and research opportunities when implementing zero speed sensorless control," in *ICEMS'2001. Proceedings of the Fifth International Conference on Electrical Machines and Systems (IEEE Cat. No.01EX501)*, vol. 1, 10 2001, pp. 1–10.

[18] S. Kim, J. Ha, and S. Sul, "Pwm switching frequency signal injection sensorless method in ipmsm," *IEEE Transactions on Industry Applications*, vol. 48, no. 5, pp. 1576–1587, 9 2012.

[19] M. Berto, P. G. Carlet, V. Manzolini, and L. Alberti, "An effective ellipse fitting technique of the current response locus to rotating hf voltage injection in ipmsm for sensorless rotor position estimation," in *IECON 2018 - 44th Annual Conference of the IEEE Industrial Electronics Society*, 10 2018, pp. 391–396.

[20] F. Toso, M. Berto, L. Alberti, and F. Marcuzzi, "Efficient qr updating factorization for sensorless synchronous motor drive based on high frequency voltage injection," *IEEE Transactions on Industrial Electronics*, vol. 67, no. 12, pp. 10 213–10 222, 12 2020.

[21] M. Berto, L. Alberti, V. Manzolini, and S. Bolognani, "Computation of self-sensing capabilities of synchronous machines for rotating high frequency voltage injection sensorless control," *IEEE Transactions on Industrial Electronics*, 2021, to be published.

[22] M. Barcaro, M. Morandin, T. Pradella, N. Bianchi, and I. Furlan, "Iron saturation impact on high-frequency sensorless control of synchronous permanent-magnet motor," *IEEE Transactions on Industry Applications*, vol. 53, no. 6, pp. 5470–5478, 11 2017.

[23] P. Guglielmi, M. Pastorelli, and A. Vagati, "Cross-saturation effects in ipm motors and related impact on sensorless control," *IEEE Transactions on Industry Applications*, vol. 42, no. 6, pp. 1516–1522, 11 2006.

[24] N. Bianchi and S. Bolognani, "Influence of rotor geometry of an ipm motor on sensorless control feasibility," *IEEE Transactions on Industry Applications*, vol. 43, no. 1, pp. 87–96, 1 2007.

[25] N. Bianchi, E. Fornasiero, and S. Bolognani, "Effect of stator and rotor saturation on sensorless rotor position detection," *IEEE Transactions on Industry Applications*, vol. 49, no. 3, pp. 1333–1342, 5 2013.

[26] G. Bacco, S. Bolognani, N. Bianchi, and V. Manzolini, "Self-sensing-oriented optimization of synchronous reluctance machine design," in *2019 IEEE 10th International Symposium on Sensorless Control for Electrical Drives (SLED)*, 9 2019, pp. 1–6.

[27] S. Wu, D. D. Reigosa, Y. Shibukawa, M. A. Leetmaa, R. D. Lorenz, and Y. Li, "Interior permanent-magnet synchronous motor design for improving self-sensing performance at very low speed," *IEEE Transactions on Industry Applications*, vol. 45, no. 6, pp. 1939–1946, 11 2009.

[28] A. Athavale, T. Fukushige, T. Kato, C. Yu, and R. D. Lorenz, "Variable leakage flux ipmsms for reduced losses over a driving cycle while maintaining suitable attributes for high-frequency injection-based rotor position self-sensing," *IEEE Transactions on Industry Applications*, vol. 52, no. 1, pp. 234–241, 1 2016.

[29] L. Chen, G. Götting, S. Dietrich, and I. Hahn, "Self-sensing control of permanent-magnet synchronous machines with multiple saliencies using pulse-voltage-injection," *IEEE Transactions on Industry Applications*, vol. 52, no. 4, pp. 3480–3491, 7 2016.

[30] N. Bianchi, S. Bolognani, J. Jang, and S. Sul, "Comparison of pm motor structures and sensorless control techniques for zero-speed rotor position detection," *IEEE Transactions on Power Electronics*, vol. 22, no. 6, pp. 2466–2475, 11 2007.

[31] Y. Kano and N. Matsui, "Rotor geometry design of saliency-based sensorless controlled distributed-winding ipmsm for hybrid electric vehicles," *IEEE Transactions on Industry Applications*, vol. 54, no. 3, pp. 2336–2348, 5 2018.

[32] B. Shuang, Z. Q. Zhu, and X. Wu, "Improved cross-coupling effect compensation method for sensorless control of ipmsm with high frequency voltage injection," *IET Electric Power Applications*, pp. 1–11, 2021.

[33] A. Varatharajan, G. Pellegrino, and E. Armando, "Signal-injection sensorless control of synchronous reluctance machines for overload operation," *IEEE Transactions on Power Electronics*, pp. 1–1, 2021.

[34] N. Bianchi, E. Fornasiero, E. Carraro, S. Bolognani, and M. Castiello, "Electric vehicle traction based on a pm assisted synchronous reluctance motor," in *2014 IEEE International Electric Vehicle Conference (IEVC)*, 12 2014, pp. 1–6.

[35] S. A. Odhano, P. Pescetto, H. A. A. Awan, M. Hinkkanen, G. Pellegrino, and R. Bojoi, "Parameter identification and self-commissioning in ac motor drives: A technology status review," *IEEE Transactions on Power Electronics*, vol. 34, no. 4, pp. 3603–3614, 4 2019.

[36] E. Armando, R. I. Bojoi, P. Guglielmi, G. Pellegrino, and M. Pastorelli, "Experimental identification of the magnetic model of synchronous machines," *IEEE Transactions on Industry Applications*, vol. 49, no. 5, pp. 2116–2125, 9 2013.

[37] J. Bonifacio and R. M. Kennel, "On considering saturation and cross-coupling effects for copper loss minimization on highly anisotropic synchronous machines," *IEEE Transactions on Industry Applications*, vol. 54, no. 5, pp. 4177–4185, 9 2018.

[38] L. Alberti, J. Gyselinck, N. Bianchi, M. Morandin, and S. Bolognani, "Small-signal finite-element modeling of synchronous machines for sensorless applications," in *2012 XXth International Conference on Electrical Machines*, 9 2012, pp. 2266–2272.

[39] L. Alberti, N. Bianchi, and S. Bolognani, "High-frequency d-q model of synchronous machines for sensorless control," *IEEE Transactions on Industry Applications*, vol. 51, no. 5, pp. 3923–3931, 9 2015.

[40] S. Chai, B. Lee, J. Hong, S. Sul, and S. Kim, "Design of ipmsm having high power density for position sensorless operation with high-frequency signal injection and the method of calculating inductance profile," in *2011 International Conference on Electrical Machines and Systems*, 8 2011, pp. 1–5.

[41] M. J. Corley and R. D. Lorenz, "Rotor position and velocity estimation for a permanent magnet synchronous machine at standstill and high speeds," in *IAS '96. Conference Record of the 1996 IEEE Industry Applications Conference Thirty-First IAS Annual Meeting*, vol. 1, 10 1996, pp. 36–41.

[42] T. S. Slininger and R. D. Lorenz, "Enhancing self-sensing estimation accuracy via negative sequence current image registration, with evaluation on a low saliency ratio machine," in *2017 IEEE International Symposium on Sensorless Control for Electrical Drives (SLED)*, 9 2017, pp. 85–90.

[43] F. Tinazzi, S. Bolognani, S. Calligaro, P. Kumar, R. Petrella, and M. Zigliotto, "Classification and review of mtpa algorithms for synchronous reluctance and interior permanent magnet motor drives," in *2019 21st European Conference on Power Electronics and Applications (EPE '19 ECCE Europe)*, 9 2019, pp. 1–10.

[44] A. Dianov, F. Tinazzi, S. Calligaro, and S. Bolognani, "Review and classification of mtpa control algorithms for synchronous motors," *IEEE Transactions on Power Electronics*, pp. 1–1, 2021.

[45] A. Varatharajan, S. Cruz, H. Hadla, and F. Briz, "Predictive torque control of synrm drives with online mtpa trajectory tracking and inductances estimation," in *2017 IEEE International Electric Machines and Drives Conference (IEMDC)*, 5 2017, pp. 1–7.

[46] N. Limsuwan, T. Kato, and R. D. Lorenz, "Concurrent design of interior-permanent-magnet machines for self-sensing and power conversion," *IEEE Transactions on Industry Applications*, vol. 48, no. 6, pp. 2157–2164, 11 2012.

[47] L. Alberti, N. Bianchi, and S. Bolognani, "Comparison of different synchronous machines for sensorless drives," in *IECON 2013 - 39th Annual Conference of the IEEE Industrial Electronics Society*, 11 2013, pp. 8220–8226.

[48] M. Berto, L. Alberti, and S. Bolognani, "Experimental investigation on the self-sensing capability of synchronous machines for signal injection sensorless drives," in *2021 IEEE Energy Conversion Congress and Exposition (ECCE)*, 2021, pp. 5078–5083.

[49] T. S. Slininger and R. D. Lorenz, "Enhancing estimation accuracy by applying cross-correlation image tracking to self-sensing including evaluation on a low saliency ratio machine," in *2016 IEEE Energy Conversion Congress and Exposition (ECCE)*, 9 2016, pp. 1–7.

[50] W. Gander, G. H. Golub, and R. Strebel, "Least-squares fitting of circles and ellipses," *BIT Numerical Mathematics*, vol. 34, no. 4, pp. 558–578, 12 1994.

[51] D. Simon, *Optimal State Estimation: Kalman, H Infinity, and Nonlinear Approaches*. New York, NY, USA: Wiley-Interscience, 2006.

[52] G. H. Golub and C. F. Van Loan, *Matrix Computations (3rd Ed.)*. Baltimore, MD, USA: Johns Hopkins University Press, 1996. [Online]. Available: https://jhupbooks.press.jhu.edu/title/matrix-computations

[53] A. Bjorck, *Numerical Methods in Matrix Computations*. Springer, Cham, 09 2014. [Online]. Available: https://link.springer.com/book/10.1007/978-3-319-05089-8

[54] V. Manzolini and S. Bolognani, "On the rotor position self-sensing capability of ipm and reluctance synchronous motors," in *2018 IEEE 9th International Symposium on Sensorless Control for Electrical Drives (SLED)*, 9 2018, pp. 108–113.

[55] N. Bianchi, S. Bolognani, and A. Faggion, "Predicted and measured errors in estimating rotor position by signal injection for salient-pole pm synchronous motors," in *2009 IEEE International Electric Machines and Drives Conference*, 5 2009, pp. 1565–1572.

[56] F. Cupertino, A. Guagnano, A. Altomare, and G. Pellegrino, "Position estimation delays in signal injection-based sensorless pmsm drives," in *3rd IEEE International Symposium on Sensorless Control for Electrical Drives (SLED 2012)*, 9 2012, pp. 1–6.

[57] P. Xu and Z. Q. Zhu, "Carrier signal injection-based sensorless control for permanent magnet synchronous machine drives with tolerance of signal processing delays," *IET Electric Power Applications*, vol. 11, no. 6, pp. 1140–1149, 2017.

[58] W. K. Yung and K. F. Man, "Optimal selected forgetting factor for rls estimation," *IFAC Proceedings Volumes*, vol. 26, no. 2, Part 1, pp. 331–334, 1993, 12th Triennal Wold Congress of the International Federation of Automatic control. Volume 1 Theory, Sydney, Australia, 18-23 July.

[59] W. Zhuang, "Rls algorithm with variable forgetting factor for decision feedback equalizer over time-variant fading channels," *Wireless Personal Communications*, vol. 8, no. 1, pp. 15–29, 10 1998.

[60] M. Berto, L. Alberti, F. Martin, and M. Hinkkanen, "Online incremental inductance identification for reluctance synchronous motors," in *IECON 2021 - 47th Annual Conference of the IEEE Industrial Electronics Society*, 2021, pp. 1–6.

[61] R. Antonello, L. Ortombina, F. Tinazzi, and M. Zigliotto, "Advanced current control of synchronous reluctance motors," in *2017 IEEE 12th International Conference on Power Electronics and Drive Systems (PEDS)*, 12 2017, pp. 1,037–1,042.

[62] H. A. A. Awan, S. E. Saarakkala, and M. Hinkkanen, "Flux-linkage-based current control of saturated synchronous motors," *IEEE Transactions on Industry Applications*, vol. 55, no. 5, pp. 4762–4769, 9 2019.

[63] M. S. Rafaq and J. Jung, "A comprehensive review of state-of-the-art parameter estimation techniques for permanent magnet synchronous motors in wide speed range," *IEEE Transactions on Industrial Informatics*, vol. 16, no. 7, pp. 4747–4758, 7 2020.

[64] S. Ebersberger and B. Piepenbreier, "Identification of differential inductances of permanent magnet synchronous machines using test current signal injection," in *International Symposium on Power Electronics Power Electronics, Electrical Drives, Automation and Motion*, 6 2012, pp. 1342–1347.

[65] S. Kuehl and R. M. Kennel, "Measuring magnetic characteristics of synchronous machines by applying position estimation techniques," *IEEE Transactions on Industry Applications*, vol. 50, no. 6, pp. 3816–3824, 11 2014.

[66] M. Hinkkanen, P. Pescetto, E. Mölsä, S. E. Saarakkala, G. Pellegrino, and R. Bojoi, "Sensorless self-commissioning of synchronous reluctance motors at standstill without rotor locking," *IEEE Transactions on Industry Applications*, vol. 53, no. 3, pp. 2120–2129, 5 2017.

[67] F. Briz, M. W. Degner, A. Diez, and R. D. Lorenz, "Measuring, modeling, and decoupling of saturation-induced saliencies in carrier-signal injection-based sensorless ac drives," *IEEE Transactions on Industry Applications*, vol. 37, no. 5, pp. 1356–1364, 9 2001.

[68] J. M. Liu and Z. Q. Zhu, "Novel sensorless control strategy with injection of high-frequency pulsating carrier signal into stationary reference frame," *IEEE Transactions on Industry Applications*, vol. 50, no. 4, pp. 2574–2583, 7 2014.

[69] A. Piippo, M. Hinkkanen, and J. Luomi, "Sensorless control of pmsm drives using a combination of voltage model and hf signal injection," in *Conference Record of the 2004 IEEE Industry Applications Conference, 2004. 39th IAS Annual Meeting.*, vol. 2, 10 2004, pp. 964–970.

[70] J. Lee, Y. Kwon, and S. Sul, "Experimental identification of ipmsm flux-linkage considering spatial harmonics for high-accuracy simulation of ipmsm drives," in *2018 IEEE Energy Conversion Congress and Exposition (ECCE)*, 9 2018, pp. 5804–5809.

[71] Z. Qu, T. Tuovinen, and M. Hinkkanen, "Inclusion of magnetic saturation in dynamic models of synchronous reluctance motors," in *2012 XXth International Conference on Electrical Machines*, 9 2012, pp. 994–1000.

[72] W. Xu and R. D. Lorenz, "High frequency injection-based stator flux linkage and torque estimation for db-dtfc implementation on ipmsms considering cross-saturation effects," in *2013 IEEE Energy Conversion Congress and Exposition*, 9 2013, pp. 844–851.

[73] X. Chen, J. Wang, B. Sen, P. Lazari, and T. Sun, "A high-fidelity and computationally efficient model for interior permanent-magnet machines considering the magnetic saturation, spatial harmonics, and iron loss effect," *IEEE Transactions on Industrial Electronics*, vol. 62, no. 7, pp. 4044–4055, 7 2015.

[74] D. Hu, Y. M. Alsmadi, and L. Xu, "High-fidelity nonlinear ipm modeling based on measured stator winding flux linkage," *IEEE Transactions on Industry Applications*, vol. 51, no. 4, pp. 3012–3019, 7 2015.

[75] M. N. Ibrahim, P. Sergeant, and E. M. Rashad, "Relevance of including saturation and position dependence in the inductances for accurate dynamic modeling and control of synrms," *IEEE Transactions on Industry Applications*, vol. 53, no. 1, pp. 151–160, 1 2017.

[76] S. Li, D. Han, and B. Sarlioglu, "Modeling of interior permanent magnet machine considering saturation, cross coupling, spatial harmonics, and temperature effects," *IEEE Transactions on Transportation Electrification*, vol. 3, no. 3, pp. 682–693, 9 2017.

[77] J. Pries and T. Burress, "High fidelity d-q modeling of synchronous machines using spectral interpolation," in *2017 IEEE Transportation Electrification Conference and Expo (ITEC)*, 6 2017, pp. 779–785.

[78] A. Sjöberg, "Real-time implementation of pmsm software model on external hardware," Ph.D. dissertation, KTH Royal Institute of Technology, 2017. [Online]. Available: http://www.diva-portal.org/smash/record.jsf?pid=diva2:1140582&dswid=7132

[79] A. A. Mohammadi, J. Gyselinck, and A. Pop, "Dynamic modeling of dual-star permanent-magnet synchronous machines using look-up tables," in *2019 Electric Vehicles International Conference (EV)*, 10 2019, pp. 1–6.

[80] K. Drobnič, L. Gašparin, and R. Fišer, "Fast and accurate model of interior permanent-magnet machine for dynamic characterization," *Energies*, vol. 12, no. 5, 2019. [Online]. Available: https://www.mdpi.com/1996-1073/12/5/783

[81] S. Ciceo, F. Chauvicourt, J. Gyselinck, and C. Martis, "A comparative study of system-level pmsm models with either current or flux-linkage state variables used for vibro-acoustic computation," in *2019 IEEE International Electric Machines Drives Conference (IEMDC)*, 5 2019, pp. 1881–1888.

My publications

[1] M. Berto, P. G. Carlet, V. Manzolini, and L. Alberti, "An effective ellipse fitting technique of the current response locus to rotating hf voltage injection in ipmsm for sensorless rotor position estimation," in *IECON 2018 - 44th Annual Conference of the IEEE Industrial Electronics Society*, 10 2018, pp. 391–396.

[2] O. B. Abdallah, A. Masmoudi, M. Berto, L. Alberti, and S. Bolognani, "Rotating high frequency injection and ellipse fitting technique for ringed-pole motor sensorless control," in *2020 Fifteenth International Conference on Ecological Vehicles and Renewable Energies (EVER)*, 9 2020, pp. 1–6.

[3] F. Toso, M. Berto, L. Alberti, and F. Marcuzzi, "Efficient qr updating factorization for sensorless synchronous motor drive based on high frequency voltage injection," *IEEE Transactions on Industrial Electronics*, vol. 67, no. 12, pp. 10 213–10 222, 12 2020.

[4] M. Berto, L. Alberti, V. Manzolini, and S. Bolognani, "Computation of self-sensing capabilities of synchronous machines for rotating high frequency voltage injection sensorless control," *IEEE Transactions on Industrial Electronics*, 2021, to be published.

[5] L. Ortombina, M. Berto, and L. Alberti, "Synchronous motor sensorless drives based on rotating signal injection and direct ellipse estimation," in *2021 International Aegean Conference on Electrical Machines and Power Electronics (ACEMP) 2021 International Conference on Optimization of Electrical and Electronic Equipment (OPTIM)*, 2021, pp. 413–419.

[6] M. Berto, L. Alberti, and S. Bolognani, "Experimental investigation on the self-sensing capability of synchronous machines for signal injection sensorless drives," in *2021 IEEE Energy Conversion Congress and Exposition (ECCE)*, pp. 5078–5083.

[7] M. Berto, L. Alberti, F. Martin, and M. Hinkkanen, "Online incremental inductance identification for reluctance synchronous motors," in *IECON 2021 - 47th Annual Conference of the IEEE Industrial Electronics Society*, pp. 1–6.